Electronic & Magnetic Properties of $Ba(Fe,Co)_2As_2$ & URu_2Si_2

Measurements of the Electronic and Magnetic Properties of Superconducting $Ba(Fe,Co)_2As_2$ and 'Hidden Order' URu_2Si_2

By

Travis Jay Williams, B.Sc. (Hons.), M.Sc.

A Thesis

Submitted to the School of Graduate Studies

in Partial Fulfilment of the Requirements

for the Degree

Doctor of Philosophy of Science

McMaster University

DOCTOR OF PHILOSOPHY OF SCIENCE (2013) McMaster University

(Department of Physics and Astronomy) Hamilton, Ontario

TITLE: Measurements of the Electronic and Magnetic Properties of Superconducting $Ba(Fe,Co)_2As_2$ and 'Hidden Order' URu_2Si_2

AUTHOR: Travis Williams, B.Sc. (Hons.), M.Sc.

SUPERVISOR: Graeme M. Luke

NUMBER OF PAGES: xxx, 147

Abstract

This thesis details a collection of experiments performed on two condensed matter systems, Co-doped $BaFe_2As_2$ and URu_2Si_2. These two materials are related by their structural type ($ThCr_2Si_2$-type) serving as great examples of the diversity of material properties present in this family. They are also both superconducting materials and belong to the collection of strongly-correlated electron systems. The interest in studying the $Ba(Fe,Co)_2As_2$ group of materials is due to the high superconducting transition temperature in these (and related) materials, while the compound URu_2Si_2 was studied due to the presence of a poorly-understood 'hidden order' phase.

Muon spin relaxation/rotation/resonance (μSR) was used to measure several single crystals of the series $Ba(Fe_{2-x}Co_x)_2As_2$ with Cobalt concentrations $x = 0.038$, 0.047, 0.061, 0.074, 0.107 and 0.114, and a single crystal of $Sr(Fe_{0.87}Co_{0.13})_2As_2$. The two samples with the lowest doping, $x = 0.038$ and $x = 0.047$, showed strong $\hat{c}$-axis magnetism occurring below the magnetic transition, T_{SDW}. The measurements suggest that the local magnetic field is increasingly disordered as the concentration of Co increases. These samples were shown to exhibit both superconductivity and magnetism, but that the entire sample contains non-zero local magnetic fields, meaning that superconductivity exists in or near regions of strong magnetic order.

The remaining compounds (with $x = 0.061$, 0.074, 0.107, 0.114 and $Sr(Fe_{0.87}Co_{0.13})_2As_2$) were measured with zero-field (ZF)-μSR and no magnetic ordering was found down to T = 1.65 K. An analytic Ginzburg-Landau model was used to fit the data and obtain absolute values for the penetration

depth, λ. A model for the temperature dependence of the density of superconducting carriers, $n_s \propto 1/\lambda^2$, based on two s-wave gaps describes the data well. Below T_{SC}, a paramagnetic frequency shift was observed indicative of field-induced magnetism along the $\hat{c}$ crystallographic direction.

Measurements of URu_2Si_2 under chemical and hydrostatic pressure have focused on measuring the spin correlations that are present in the hidden order phase. The chemical pressure that is induced by 5% Re doping perturbs, but does not destroy, the commensurate spin excitations. The spin gap that is present in the parent material is also present under this chemical doping. The hidden order phase survives at least halfway to the quantum critical point to ferromagnetism, but is weakened by the Re substitution.

Under hydrostatic pressure of 10.1 kbar, URu_2Si_2 becomes antiferromagnetic, but the spin correlations are found to be qualitatively similar to those of the hidden order phase. The width in reciprocal space ($\vec{Q}$-width) of the excitations and their gapped nature remains unchanged upon entering the antiferromagnetic phase. Quantitatively, there is an increase in the magnitude of the gap at $\vec{Q} = (1.4\ 0\ 0)$. This may be a result of the increase in the transition temperature preceding the entry to the antiferromagnetic phase.

Due to the large difference in their properties, and hence the motivation for studying $Ba(Fe_{1-x}Co_x)_2As_2$ and URu_2Si_2, they will be introduced and presented separately. Chapter 1 will provide the necessary background material on $Ba(Fe,Co)_2As_2$, while Chapter 2 will provide the background for the work on URu_2Si_2. Chapter 3 will describe the experimental techniques that were used to study these systems.

Original research results on $Ba(Fe,Co)_2As_2$ are presented in Chapter 4. This is mainly focused on μSR measurements of dopings that display superconductivity. Samples that did not order magnetically were measured in the mixed state to measure the vortex lattice to extract the various properties, including the superconducting pairing symmetry. Samples that did order magnetically were measured to analyze the amount of magnetic disorder and discover the extent of coexistence or phase separation between magnetism and superconductivity.

Chapter 5 details the original research results on URu_2Si_2. This involved crystal growth of these compounds, and two neutron scattering experiments to measure the spin correlations while perturbing the hidden order state. The first experiment was done on a Re-doped crystal, $URu_{1.9}Re_{0.1}Si_2$. Doping with Re suppresses the hidden order, eventually leading to ferromagnetism at higher dopings. This work showed that the spin correlations are also suppressed, but not as quickly as the hidden order. The second experiment was on pure URu_2Si_2 under hydrostatic pressure. Applied pressure increases the hidden order transition, but eventually leads to antiferromagnetism, the phase in which the experiment was performed.

Acknowledgements

I owe thanks to a number of people who have been a source of support, personally and professionally, during my graduate career. This thesis would not exist without their contributions, so I would like to acknowledge some of their many contributions.

My supervisor, Dr. Graeme Luke, has been a mentor for six years and I owe my professional success to him. While his expertise has been the leading cause of success for the projects discussed in this thesis, I feel more indebted to him for his tireless encouragement and the opportunities he has provided to help me grow as a professional researcher. While he always sought to give me a great deal of independence, I have never felt on my own. The desire to be there for his students no matter what the issue is a model for which I will continue to strive as I take on new challenges. And I feel confident that I will have a friend wherever those challenges take me.

I have been even more fortunate to find other brilliant researchers who have taken an interest in my success and who have selflessly given of themselves to help me achieve that success. In my work at TRIUMF, for seemingly endless months, Dr. Tomo Uemura has been a great inspiration. His enthusiasm for the work is contagious and continues to motivate me in my love of physics. At Chalk River, Dr. Bill Buyers has been a great help to understand neutron scattering and the analysis of those measurements. I am very lucky to have have the opportunity to work with a world-class physicist and gentleman whose patience in answering my myriad of questions continues to amaze me. At McMaster, I need to acknowledge the other two members of my committee, Dr. Bruce Gaulin and Dr. Takashi Imai. They have always been there to greet me with a smile (and often a funny remark) and made me feel at ease at the most trying points of my graduate career. I am

blessed to have this group of researchers who have helped me to the point of calling them colleagues.

The many hours in the lab, office or lecture hall have introduced me to some wonderful friends with whom I could share the joys and trials. The members of Dr. Luke's research group, past and present: Dr. Greg MacDougall, Dr Adam Aczel, Tim Munsie, Rob D'Ortenzio and Teresa Medina. Members of Dr. Uemura's group: Tatsuo Goko, Jeremy Carlo and Carlos Arguello. Other students at McMaster: Pat Clancy, Kate Ross, Jerod Wagman, Katharina Fritsch, Jesse Hall, Phil Ashby and many others. Thank you all for the good times that made the past six years so unforgettable.

I have been further blessed to have a wonderfully supportive family. My parents, Margaret and Terry, have never missed an opportunity to encourage me in my work. It is reassuring to know that their constant refrain, "Have you finished your thesis yet?" was really just a veil for "How are you? How can we help?" Knowing that they are always behind me has given me the confidence to proceed into the unknown territory that is scientific research. And just as supportive has been my brother, Cameron. Whether a casual dinner, a game of golf or just a chat, I know I can always count on him to keep me level. I am certain that wherever my work may take me in the future, I have a family whom I can always depend on. Thank you all.

Lastly, to my wonderful fiancé Kelly: Thank you for everything. My work, my scientific career, is just a small part of my life; none of which would hold much meaning for me without you. The countless nights you took care of me, allowing me to work uninterrupted and without worrying means so much to me. I know that I have nothing to worry about with you by my side. I am starting a great journey and I know how excited I am to share that with you. I love you.

Co-Authorship

All of the projects discussed in this thesis are collaborative works.

The series of $Ba(Fe,Co)_2As_2$ crystals discussed in Chapter 4 were grown by N. Ni, S.L. Bud'ko and P.C. Canfield at Ames Laboratory, Iowa State University. The μSR measurements were performed at TRIUMF, Vancouver, British Columbia by myself and others, including the research groups of Y.J. Uemura, E. Baggio-Saitovich, H. Kageyama and the other members of the research group of G.M. Luke: A.A. Aczel, T.J.S. Munsie, R.M. D'Ortenzio and M.T. Medina Fernandez.

The $URu_{1.9}Re_{0.1}Si_2$ crystals, as well as some of the crystals of URu_2Si_2, discussed in Chapter 5, were grown by N.P. Butch and M.B. Maple at the University of California, San Diego. The neutron scattering measurements for the Re-doped material as well as comparative measurements on the pure material were performed at Chalk River Laboratories, Chalk River, Ontario. These measurements were performed by myself, with assistance from Z. Yamani and W.J.L. Buyers.

The URu_2Si_2 measurements performed under pressure were measured at the NIST Center for Neutron Research, Gaithursburg, Maryland. These measurements were performed by myself, with assistance from H. Barath, J.A. Rodriguez-Riviera, J.B. Leao and C. Broholm. The crystals used were grown by myself at McMaster University, Hamilton, Ontario, with assistance from J.D. Garrett. The characterization of this crystal was also performed by myself. W.J.L. Buyers and Z. Yamani were also of assistance with some of the technical aspects of this project.

Finally, the data analysis and the writing contained herein this thesis is a result of my own work, under the supervision of G.M. Luke.

"Do you know the laws of the heavens?
Can you set up God's dominion over the earth?"
Job 38:33

Table of Contents

Abstract iii

Acknowledgements vi

Co-Authorship viii

List of Figures xiii

List of Tables xxx

Chapter 1 Introduction to $Ba(Fe,Co)_2As_2$ **1**

1.1 Conventional and Unconventional Superconductivity 1

1.2 Iron Pnictide Superconductivity 8

1.3 Experimental Survey of $Ba(Fe,Co)_2As_2$ 12

Chapter 2 Introduction to URu_2Si_2 **20**

2.1 Heavy Fermion Materials 20

2.2 URu_2Si_2 and Hidden Order 23

2.3 Experimental Survey of the Hidden Order Phase 27

2.3.1 $U(Ru,Re)_2Si_2$ 33

2.3.2 URu_2Si_2 Under Hydrostatic Pressure 36

Chapter 3 Experimental Techniques **40**

3.1 Crystal Growth 41

3.2 Muon Spin Relaxation/Rotation/Resonance (μSR) 44

3.2.1 Principles of μSR 44

3.2.2 Zero-Field (ZF)-μSR 48

3.2.3 Transverse Field (TF)-μSR 54

3.2.4 μSR in the Vortex State of Type-II Superconductors . 57

3.3 Neutron Diffraction 62

3.3.1 Introduction to Neutron Scattering Properties 62

3.3.2 The Triple-Axis Neutron Scattering Technique 66

3.3.3 The C5 DUALSPEC Spectrometer 69

3.3.4 The Multi-Axis Crystal Spectrometer 70

3.3.5 Instrumental Resolution Function 71

Chapter 4 μSR Measurements of $Ba(Fe,Co)_2As_2$ 74

4.1 Introduction 74

4.2 Coexistence of Magnetism and Superconductivity in Underdoped $Ba(Fe,Co)_2As_2$ 76

4.3 Superfluid Density of Optimally-Doped $Ba(Fe_{0.926}Co_{0.074})_2As_2$) 85

4.4 Superfluid Density of Overdoped $Ba(Fe,Co)_2As_2$ 93

4.5 Field-Induced Magnetism in Overdoped $Ba(Fe,Co)_2As_2$ 100

4.6 Conclusions 102

Chapter 5 Neutron Scattering Measurements of URu_2Si_2 **104**

5.1 Introduction 104

5.2 Measurements of Re-doped $URu_{1.9}Re_{0.1}Si_2$ 105

5.3 Measurements of URu_2Si_2 Under Hydrostatic Pressure 114

5.4 Conclusions 119

Chapter 6 Conclusions **123**

6.1 $Ba(Fe_{1-x}Co_x)_2As_2$ and $Sr(Fe_{0.87}Co_{0.13})_2As_2$ 123

6.2 $URu_{1.9}Re_{0.1}Si_2$ and URu_2Si_2 124

List of Figures

1.1 The interface between normal and superconducting regions, and how ξ and λ dictate the field strength and superconducting order parameter at the transition. Adapted from [5]. 2

1.2 The H-T phase diagram for a superconductor. In a type-I superconductor, there is only one critical field, H_c, and the phase transition is given by the dotted line. In a type-II superconductor, shown by the solid lines, there are two transitions. For $T \leq T_{SC}$ and $H \leq H_{c1}(T)$, the material is in the Meissner state. For $T \leq T_{SC}$ and $H_{c1}(T) \leq H \leq H_{c2}(T)$, the material is in the mixed state. The values of H_c, H_{c1} and H_{c2} depend on the microscopic parameters. Adapted from [6]. 3

1.3 (Left) The specific heat of a normal metal and superconductor. This difference in entropy is reflected in the free energy (right). This illustrates the second-order transition to the superconducting state. Adapted from [7]. 4

1.4 The temperature dependence of the superconducting gap, measured by electron tunnelling. This shows the excellent agreement between a conventional, elemental superconductor and BCS theory. Figure adapted from [6]. See also [9]. 5

1.5 (a) A plot of the *d*-wave superconducting gap on a circular Fermi surface. Note the nodal points at which the gap changes sign. (b) The angular dependence of the gap energy as measured by ARPES in Bi-2212. Figure taken from [21] and used with permission. 7

1.6 The structure of the various families of Iron pnictide superconductors. Figure taken from [27] and used with permission. 9

1.7 The phase diagram of $Ba(Fe,Co)_2As_2$. Most notable is the similarity to the cuprate phase diagram where superconductivity is also in close proximity to the antiferromagnetic phase of the parent compound. Figure taken from [27] and used with permission. . 11

1.8 Resistivity (upper), Magnetization (middle) and heat capacity (lower) data on the parent material $BaFe_2As_2$. Here we see the clear signatures of the first order transition to an orthorhombic antiferromagnet at T = 133 K. Figure taken from [28] and used with permission. 11

1.9 Thermoelectric power (left) and Hall coefficient (right) measurements over a range of Co-dopings. Dramatic changes are seen above $x = 0.24$, suggesting a topological change or distortion in the Fermi surface, coinciding with the onset of superconductivity. Figure taken from [44] and used with permission. 14

1.10 (Left) The phase diagram in the doping region near where static magnetism disappears. It shows the turnover of the magnetic and structural transitions, and the region in which the incommensuration appear. (Right) The neutron scattering measurements showing the change from commensurate to incommensurate order, and then to the loss of magnetic order at higher dopings. Figure taken from [60] and used with permission. . . 16

1.11 The Fermi surface structure of electron-doped (eg. $Ba(Fe,Co)_2As_2$, left) and hole-doped (eg. $(Ba,K)Fe_2As_2$, right) pnictide superconductors. Note the two sets of spherical Fermi sheets connected along $(\pm\pi,\pm\pi)$. Figure taken from [65] and used with permission. 17

1.12 A schematic of the s_{++} (left) and $s_{\pm}$ (right) states. In the latter case, we see the sign changes as we move along the $(\pi,0)$-direction. Figure taken from [63] and used with permission. . . 19

2.1 The structure of URu_2Si_2. It is tetragonal, space group I_{4mmm}, with the $ThCr_2Si_2$ structure. 24

2.2 The specific heat of URu_2Si_2. This shows the phase transitions at $T_0 = 17.5K$ and $T_{SC} = 1.2K$. This also demonstrates the fit to the large specific heat coefficient of $\gamma = 180$ mJ/mol K^2. Figure taken from [92] and used with permission. 25

2.3 The susceptibility of URu_2Si_2 as a function of temperature. This indicates a $\hat{c}$-axis, Ising-like magnet, with Curie-Weiss behaviour above T = 150 K. From the high-T data, we see that T_{CW} = -65 K and the coherence temperature, $T^{\star} \approx 60$ K. We also see a drop and a plateau in the susceptibility around the hidden order transition. Figure taken from [94] and used with permission. . 26

2.4 The resistivity of URu_2Si_2 as a function of temperature. Figure taken from [94] and used with permission. 27

2.5 Neutron scattering measurements at various $\vec{Q}$ in the hidden order state. Both excitations are seen here: the commensurate $\vec{Q}_{com}$ = (1 0 0) dispersing in the top two cuts and the incommensurate $\vec{Q}_{inc}$ = (1 0.4 0) dispersing from that cut (2^{nd} from the bottom). Figure taken from [115] and used with permission. 29

2.6 A series of inelastic neutron scattering measurements along the (H 0 0) direction, highlighting the excitations present in the hidden order phase. Here we see the gap in the incommensurate excitations, and the large spin wave velocities at both wavevectors. (inset) The quasi-elastic scattering at (1.4 0 0), showing the opening of the gap below T_0 = 17.5 K. Figure taken from [121] and used with permission. 30

2.7 The phase diagram up to 50 % Re substitution. The hidden order is continuously suppressed, with a quantum critical point estimated around $x = 0.10$. A ferromagnetic phase then arises, which extend up to at least 50 % doping, but displays non-Fermi liquid-like behaviour. The quantum critical point and ferromagnetism are a departure from other chemical substitutions, where an antiferromagnetic phase usually emerges from within the hidden order dome. Figure taken from [137] and used with permission. 34

2.8 The electrical resistivity (a) and the specific heat (b) of $URu_{2-x}Re_xSi_2$ as a function of temperature. Both quantities display discontinuities as T_0. Despite the decrease in the transition temperature the features remain well-defined, suggesting that the gapping of the Fermi surface is fairly robust against this disorder. Figure taken from [137] and used with permission. 35

2.9 The specific heat of URu_2Si_2 as a function of pressure and temperature. This shows the phase transition at $T_0 = 17.5$K, which increases slightly with applied pressure. Figure taken from [94] and used with permission. 36

2.10 Pressure-temperature phase diagram of URu_2Si_2 using He as a pressure medium, compared to various other media. Applied pressure initially increases T_0 before an antiferromagnetic phase emerges above 0.5 GPa. It is suspected that superconductivity and antiferromagnetism meet at a multicritical point. Figure taken from [142] and used with permission. 37

2.11 Shubnikov-de Haas measurements as a function of field angle (a & b, in the LMAF phase) and pressure (c & d, summed over the entire Fermi surface pocket). No dramatic changes in the Fermi surface are seen in the LMAF phase, and only slight changes in the cyclotron effective mass due to the increased moment size. Figure taken from [127] and used with permission. 39

3.1 Schematic of the mono-arc furnace used for premelting of the samples. A welding arc from a high-voltage supply heats the material, which is in an inert Ar atmosphere. 41

3.2 Schematic of the tri-arc furnace. The sample is placed on the stage and melted with the arcs. The seed rod is lowered into the sample, crystallizing material on it. As the seed rod is raised, more material solidifies, forming a long, single-crystalline rod. 42

3.3 A representation of the probability distribution of the positron momentum produced from muon decay. When the positron carries all of the energy ($\sim$ 53 MeV, the rest energy of the muon) the decay is highly anisotropic. The distribution becomes more isotropic with lower energy, becoming completely symmetric at half the rest energy ($\sim$ 26 MeV). Figure taken from [154]. . . . 47

3.4 The experimental geometry of a ZF-μSR experiment. Here, we define $\hat{z}$ as being the beam direction, $\hat{y}$ is Up-Down and $\hat{x}$ is Right-Left. Figure taken from [154]. 49

3.5 An example of a μSR histogram in one counter. This shows the oscillatory behaviour of the rotating muon spin, which decreases over time, superimposed on the exponential from the radioactive decay of the muon. Data taken by the author as part of [155]. 51

3.6 An example of a μSR asymmetry using two counters. This shows the oscillatory behaviour of the rotating muon spin more clearly, including its decreases over time. The exponential arising from the radioactive decay of the muon has been cancelled out with this method. Data taken by the author as part of [155]. 52

3.7 The experimental geometry of a TF-μSR experiment. This shows the latter of the two arrangements, where the muon spin has been rotated to be perpendicular to the beam direction (the muon momentum). The magnetic field is then applied along the direction of the muon momentum. Figure taken from [154]. 55

3.8 The spatial variation of the superconducting parameters $J_s(r)$ and $\psi(r)$ around a conventional vortex core. The parameters are shown normalized to their maximum values, which occurs at $r = r_0$ for the supercurrent density and $r = \infty$ (far from the vortex core) for the superconducting order parameter. Figure taken from [160] and used with permission. 58

3.9 The theoretical field distribution for a hexagonal vortex lattice. The maximum, minimum and most probable (saddle point) fields are shown. The inset shows a contour plot of such an arrangement of vortices. Figure adapted from [160]. 60

3.10 The field distribution measured in the normal (top) and mixed (bottom) states of $YBa_2Cu_3O_{6.95}$, which has a hexagonal vortex lattice. In the normal state, the field distribution is a narrow Gaussian about the applied field. Below T_{SC}, the Abrikosov lineshape appears. Superimposed on this is a Gaussian with the same frequency and smaller amplitude than the normal state. This is due to a volume fraction or background that is not superconducting. Figure taken from [160] and used with permission. 62

3.11 An illustration of Bragg's law in a periodic crystal. The path length difference is $2d\sin(\theta)$, which is an integer multiple of the wavelength to obtain constructive interference. Figure taken from [5]. 64

3.12 A schematic representation of a triple axis experimental setup. Here, a beam of neutrons from a source is incident on the monochromator crystal, selecting an incoming energy. The neutrons are then scattered from the crystal, and the outgoing beam is scattered from the analyzer crystal, picking out one particular outgoing energy. The resultant flux is then measured by a detector. Figure taken from [166]. 67

3.13 A schematic representation of a four-circle diffractometer. This is used to rotate the crystal through α, β and γ, and to change the scattering angle, θ, to achieve any desired scattering vector $\vec{Q}$. Figure taken from [167]. 68

3.14 (Left) An image of the C5 Spectrometer, showing the sample in between the analyzer & detector and the monochromator and source. (Right) The layout of the beamline floor at Chalk River Laboratories, indicating the location of C5, and showing the three axes for the instrument. Figure taken from [167]. 70

3.15 (Left) An overhead schematic of MACS, showing its various components. (Right) A closer view of the sample station and the 20 detector channels. Figure taken from [168] and used with permission. 71

4.1 (Top) Resistivity of $Ba(Fe_{0.926}Co_{0.074})_2As_2$ in the vicinity of T_{SC} and (inset) from 2 to 300 K. (Bottom) Field-cooled and zero-field-cooled magnetization in the vicinity of T_{SC}. Figure taken from [173]. 75

4.2 The zero-field (ZF)-μSR spectra taken at T = 1.65 K for the parent $x = 0$ (blue), $x = 0.038$ (red) and $x = 0.047$ (black). The $x = 0.038$ data is vertically offset by +0.15 and the $x = 0$ data is vertically offset by +0.3 for clarity. The solid lines are fits to the data, as described in the text. Here, clear precession is seen in the parent material, but the precession in the doped compounds are strongly damped, indicating significantly disordered magnetism. Figure taken from [172]. 77

4.3 (a) ZF-μSR spectra for $Ba(Fe_{1-x}Co_x)_2As_2$ for $x = 0.038$ ($T_{SDW} = 71$ K and $T_{SC} = 8$ K) and $x = 0.047$ ($T_{SDW} = 45$ K and $T_{SC} = 15$ K). There is a clear onset at T_{SDW}, where the precession frequency becomes non-zero. There is no change below T_{SC}. Figure taken from [172]. 79

4.4 TF-μSR measurements of $x = 0.038$ and 0.047 in TF = 4 mT. (a) The frequency shows a drop below the magnetic ordering temperature, but slowly increases again towards T = 0. This may be indicative of field-induced ordering. (b) The relaxation rate increases sharply below T_{SDW}, saturating well before T = 0. This indicates that the local field is fairly inhomogeneous in these samples, which causes dephasing of the muon polarization in the ordered part of the phase diagram. (c) We see a 100% paramagnetic signal above T_{SDW}, which drops sharply at the transition. Below the ordering temperature, there is a residual signal from the low-field region, about 40% for $x = 0.047$ and less than 10% for $x = 0.038$. Due to the small residually-precessing volume present in the 3.8% doped sample, the points below 50 K are omitted from (a) and (b). Figure taken from [172]. 80

4.5 Representative TF-μSR spectra measured in $Ba(Fe_{0.962}Co_{0.038})_2As_2$ in a field TF = 40 G. The black squares are data taken at T = 1.65 K in a spin-rotated (SR) configuration, such that the initial muon spin direction is perpendicular to the crystallographic $\hat{c}$-axis. The other two sets of data, the red circles (T = 90 K) and the green triangles (T = 1.65 K) are taken in a non-spin rotated (non-SR) configuration, so that the initial muon spin direction is along $\hat{c}$. These spectra provide evidence for strong $\hat{c}$-axis magnetism, and no macroscopic phase separation of strongly- and weakly-magnetic regions. 82

4.6 Fast Fourier transform of the TF-μSR signal in B = 0.1 T applied along the $\hat{c}$ crystallographic axis. The solid black line is taken at T = 1.7 K while the red dashed line corresponds to T = 30 K. The anisotropic shape at low temperature is characteristic of a well-ordered vortex lattice. Figure taken from [173]. 85

4.7 Combined two-gap fit (solid line) and power-law fit (dashed line) to the superfluid density measured from TF-μSR at fields of 0.02 T (black diamonds), 0.05 T (red crosses) and 0.1 T (green squares). Error bars are smaller than the plotting symbols. Figure taken from [173]. 88

4.8 (Top) Magnetic field dependence of the magnetic penetration depth in $Ba(Fe_{0.926}Co_{0.074})_2As_2$ measured at T = 1.7 K. (Bottom) $1/\lambda^2 \propto$ superfluid density, n_s, measured at T = 1.7 K. Figure taken from [173]. 92

4.9 Fourier transforms of the TF-μSR spectra for $Ba(Fe_{1-x}Co_x)_2As_2$, showing the anisotropic lineshapes characteristic of an Abrikosov vortex lattice. Figure taken from [174]. 94

4.10 Superfluid density $n_s \propto 1/\lambda^2$ as a function of temperature for the (Ba,Sr)(Fe,Co)$_2$As$_2$ samples measured. The filled symbols and solid lines are the measured values and two-gap fits in TF = 0.02 T, respectively, while the open symbols and dashed lines are the measurements and fits in TF = 0.1 T. Figure taken from [174]. 95

4.11 Superconducting T_{SC} and $1/\lambda_0^2$ for $Ba(Fe_{1-x}Co_x)_2As_2$ and $Sr(Fe_{1-x}Co_x)_2As_2$ as a function of Co concentration x, measured in TF = 0.02 T and 0.1 T, and for extrapolated values to B = 0. The open points and dashed lines are the measured T_{SC}'s and the superconducting dome taken from [31] for $Ba(Fe_{1-x}Co_x)_2As_2$ and from [196] and [197] for $Sr(Fe_{1-x}Co_x)_2As_2$. Figure taken from [174]. 97

4.12 Superconducting T_{SC} versus $1/\lambda_0^2$ for $Ba(Fe_{1-x}Co_x)_2As_2$ and $Sr(Fe_{1-x}Co_x)_2As_2$ as a function of Co concentration x, measured in TF = 0.02 T and 0.1 T, and for extrapolated values to B = 0. Figure taken from [174]. 98

4.13 $1/\lambda_0^2$ versus superconducting T_{SC} for $Ba(Fe_{1-x}Co_x)_2As_2$ and $Sr(Fe_{1-x}Co_x)_2As_2$ as a function of Co concentration x, measured in TF = 0.02 T and 0.1 T, and for extrapolated values to B = 0. This is plotted with $\Delta C_p/T_{SC}$ from [198]. The dashed line has slope $n = 2$ and is a guide to the eye. Figure taken from [174]. 99

4.14 Fractional shift of the muon precession frequency, $\nu_S/\nu_N - 1$, relative to the normal state frequency, ν_N. The superconducting transition temperatures are indicated by triangular symbols. Figure taken from [174]. 101

5.1 Magnetic Phase diagram of $URu_{2-x}Re_xSi_2$ showing the antiferromagnetic (hidden order) and ferromagnetic phases. Figure taken from [137] and used with permission. See also [206] and [207]. 105

5.2 Inelastic scattering along the (H 0 0) direction for an energy transfer of 2.9 meV at T = 2 K (black squares) and T = 40 K (red circles). At 40 K, well above the hidden order transition, there is partial suppression of the incommensurate fluctuations. In contrast, there is almost complete suppression of the commensurate fluctuations. The lines are Gaussian fits at each of the three peak positions. Figure taken from [204]. 107

5.3 The temperature dependence of the commensurate (1 0 0) fluctuations in $URu_{1.9}Re_{0.1}Si_2$ at 1.65 meV. The onset of order parameter-like behaviour is observed around at the hidden order phase transition, T = 15 K. The inset shows a close-up of the data below 30 K. Figure taken from [204]. 108

5.4 The fits to the incommensurate fluctuations for (a) $URu_{1.9}Re_{0.1}Si_2$ at T = 2 K and for (b) URu_2Si_2 at T = 3 K and 5 K (combined data). The blue line is the fit to Eq. 5.1 and the red line is a fit to a Lorentzian of energy 2Δ, amplitude A, and damping 2γ = FWHM, convoluted with the resolution function, as described below. For the Re-doped case, the nesting gap energy, Δ, is reduced to 60% of its value in the pure system. Figure taken from [204]. 109

5.5 (a) The elastic scattering at (1 0 0) in the $URu_{1.9}Re_{0.1}Si_2$ sample, measured at T = 2K. (b) The (1 0 0) inelastic scattering in the pure URu_2Si_2 system, measured at 3 K and 5 K (combined data). Both were fit to a Gaussian for the elastic peak and a Lorentzian of energy $\omega_{\vec{Q}} = 2\Delta$, amplitude A, and damping 2γ = FWHM for the inelastic peak, convoluted with the resolution function. The commensurate fluctuations of the hidden order state are damped in the presence of Re-doping. Figure taken from [204]. 111

5.6 Locus of the half-widths in reduced wave vector, H, of spin fluctuations around (1.4 0 0). These inverse dynamic correlations lengths are narrow in wave vector for low energies, but they broaden significantly at higher energies. The black circles are the center of the peak, while the red squares are the FWHM of the peaks. The error bars for the low-energy data lie within the points. Figure taken from [204]. 113

5.7 The scattering intensity as a function of energy and scattering vector along (H 0 0) in the three phases studied: (a) at ambient pressure and 25 K, in the paramagnetic phase. The phonon at (2 0 0) is visible, as are the excitations at the incommensurate (1.4 0 0) wave vector. (b) at ambient pressure and 2 K, in the hidden order regime. The phonon is present with equal intensity, while the excitations at (1.4 0 0) have become gapped, and more slowly dispersing. The commensurate excitation at (1 0 0) is also present. (c) at 10.1 kbar and 4 K, in the antiferromagnetic phase. The scattering here looks qualitatively similar to the spectrum in the hidden order phase, with some additional intensity at the commensurate point. Figure taken from [205]. 115

5.8 Constant energy slices in the (H 0 L) plane in each of the three phases. Energies shown are 2, 5, 8 and 11 meV (clockwise from top left). The range of integration of energy for the slices was ±0.5 meV. Figure taken from [205]. 118

5.9 The energy-dependence of the scattering intensity at the commensurate (filled circles) and incommensurate (open circles) wave vectors in each phase. The lines are fits to the data as described in the text. (a) In the paramagnetic phase, no scattering is seen at the commensurate point, while a weak signal is seen at the incommensurate point. (b) In the hidden order phase, the scattering is much more intense at both wave vectors while opening a spin gap at (1.4 0 0). (c) In the antiferromagnetic phase, both peaks are still present. The incommensurate peak seems to have shifted to slightly higher energies. (inset) The scattering along (1 0 L) in the antiferromagnetic phase shows the substantially more intense peak at (1 0 0), arising from the large, ordered antiferromagnetic moment. Figure taken from [205]. 120

List of Tables

2.1 Ordering temperature of various heavy fermion materials with different ground state configurations. In the non-magnetic materials, the temperature stated corresponds to the lowest measured temperature. Data taken from [75, 87, 88]. 22

4.1 Values obtained for $n_s(0)$ and p from the power law fits shown in Fig. 4.7. Data taken from [173]. 89

4.2 Values obtained for the weighting factor, w, and superfluid density, $n_s(0)$, from the two-gap fits shown in Fig. 4.7. Data taken from [173]. 91

4.3 Results of fitting $1/\lambda^2(T)$ to Eq. 4.4 for T_{SC} (in K) and λ_0 (in nm). Also shown are values of λ_0 extrapolated to B = 0. Data taken from [174]. 96

5.1 Results of fitting the data in Fig. 5.9 to the dispersion described in Eq. 5.3. Data taken from [205]. 121

Chapter 1

Introduction to $Ba(Fe,Co)_2As_2$

1.1 Conventional and Unconventional Superconductivity

Superconductivity is a state that is characterized by two properties: perfect electrical conductivity and perfect diamagnetism. Discovered by Onnes in 1911, the property of perfect conductivity was the first signature of superconductivity [1], while Meissner and Ochsenfeld's discovery of the "Meissner Effect" (perfect diamagnetism) in 1933 [2] showed the second property of superconductors. The explanation for why superconductivity occurs didn't come until 1957 when it was shown by Bardeen, Cooper and Schrieffer (called BCS Theory) that any net attractive interaction between electrons would cause them to pair up, and that these "Cooper pairs" would be able to travel through the material with no resistance [3]. It was also Bardeen, Cooper and Schrieffer who explained that this attractive interaction could be mediated by phonons, thereby providing the mechanism responsible for superconductivity. These

properties along with a theoretical framework provided the beginnings of the characterization of a "conventional" superconductor.

Many of the properties of superconductors can be characterized by two parameters: the superconducting coherence length, ξ, and the magnetic penetration depth, λ. The value of ξ, roughly speaking, describes the size of the Cooper pairs, while λ denotes how far into the superconductor a magnetic field penetrates. These are both temperature-dependent and are illustrated in Fig. 1.1. Abrikosov determined that for values of $\xi/\lambda \leq \frac{1}{\sqrt{2}}$, the superconductor would form a 'mixed' state at a range of applied fields, $H_{c1} \leq H \leq H_{c2}$, where the field would penetrate in filament-like "vortices" [4]. The field-dependent phase diagram for a superconductor is shown in Fig. 1.2.

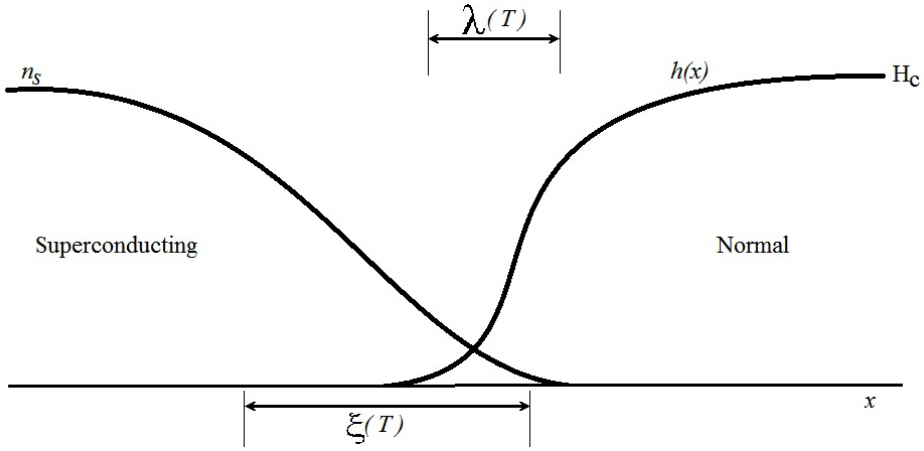

Figure 1.1: The interface between normal and superconducting regions, and how ξ and λ dictate the field strength and superconducting order parameter at the transition. Adapted from [5].

The mixed state occurs because for $\xi/\lambda \leq \frac{1}{\sqrt{2}}$, the mixed state has a lower free energy than the Meissner state for fields between $H_{c1}(T)$ and $H_{c2}(T)$.

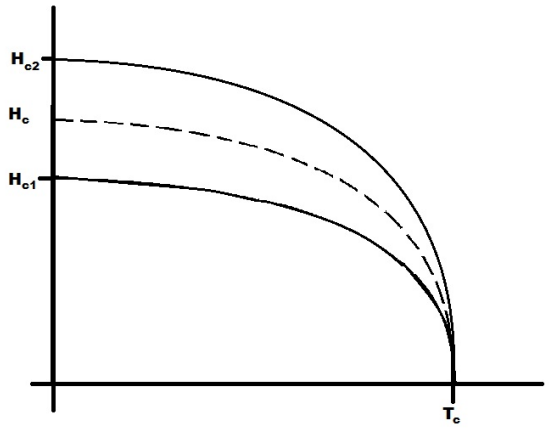

Figure 1.2: The H-T phase diagram for a superconductor. In a type-I superconductor, there is only one critical field, H_c, and the phase transition is given by the dotted line. In a type-II superconductor, shown by the solid lines, there are two transitions. For T $\leq$ T$_{SC}$ and $H \leq H_{c1}(T)$, the material is in the Meissner state. For T $\leq$ T$_{SC}$ and $H_{c1}(T) \leq H \leq H_{c2}(T)$, the material is in the mixed state. The values of H_c, H_{c1} and H_{c2} depend on the microscopic parameters. Adapted from [6].

Since the superconducting wave function is single-valued, the magnetic flux penetrating the sample is quantized such that each vortex carries a flux $\Omega = \frac{h}{2e}$ where h is Planck's constant and e is the fundamental charge constant.

The free energy in the superconducting phase can be derived from the specific heat (Fig. 1.3(a)), and is shown in Fig. 1.3(b) [7]. The difference in the free energy between the superconducting and normal state is called the condensation energy. This modification to the energy of a fraction of the metallic electrons in the system produces a discontinuity at T$_{SC}$. Below this temperature, the entropy decreases markedly. Measurements of the electronic contribution to the heat capacity as the temperature approached 0 K were found to be exponential, with a form given by,

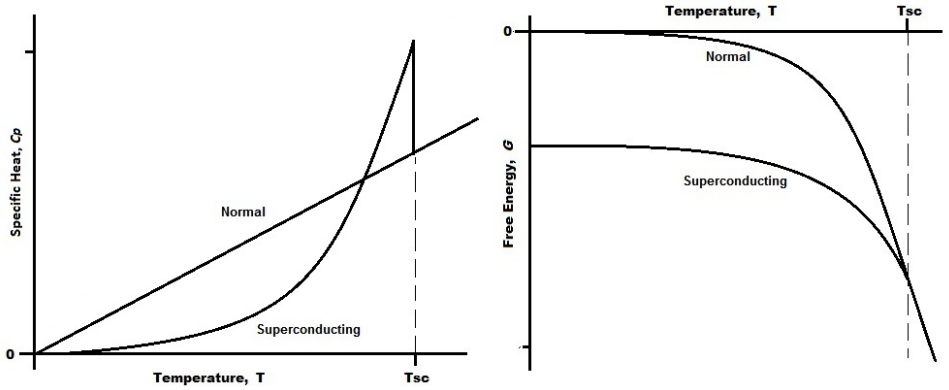

Figure 1.3: (Left) The specific heat of a normal metal and superconductor. This difference in entropy is reflected in the free energy (right). This illustrates the second-order transition to the superconducting state. Adapted from [7].

$$C_p \propto \exp\left(-\Delta/2k_BT\right) \tag{1.1}$$

This is the form for a fully, isotropically gapped system, where in a superconductor, Δ is known as the superconducting energy gap. The temperature dependence of the gap function, $\Delta(T)$ is shown in Fig. 1.4. This is predicted from Bardeen-Cooper-Schrieffer (BCS) theory, and shows excellent agreement with measurements of elemental superconductors such as Niobium and Tin [6, 8]. It was also a prediction of BCS theory that the size of the superconducting gap was given by [5]:

$$\Delta = 1.764 k_B T_{SC} \tag{1.2}$$

By considering a superconductor as two fluids, one normal and one superconducting, and using the techniques developed by London and London for

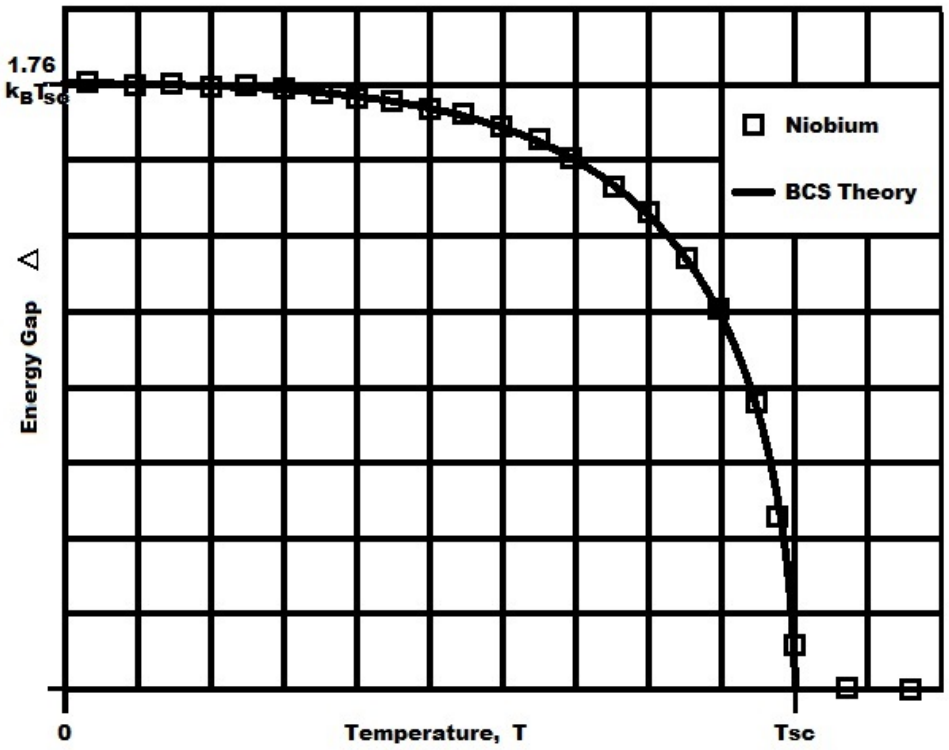

Figure 1.4: The temperature dependence of the superconducting gap, measured by electron tunnelling. This shows the excellent agreement between a conventional, elemental superconductor and BCS theory. Figure adapted from [6]. See also [9].

electrodynamics [10], one can classify the microscopic quantities of the superconductor in terms of quantities like the superfluid density, n_s. The London penetration depth, λ_L is given by:

$$\lambda_L = \sqrt{\frac{mc^2}{4\pi n_s e^2}} \tag{1.3}$$

This illustrates that the superfluid density, $n_s \propto 1/\lambda^2$ and so measurements of the penetration depth can reveal additional properties of the supercon-

ductor, such as the superconducting gap symmetry, an important connection for the measurements in Chapter 4. Later, the phenomenological model of Ginzburg and Landau [11] showed that the coherence length can be written as:

$$\xi = \frac{2\hbar v_F}{\pi \Delta} \tag{1.4}$$

Another important consequence of the BCS theory was that due to the mechanism of Cooper pairing and the energy scale of phonon spectra in real materials, superconductivity shouldn't be possible above ∼35 K. Thus, the discovery of $YBa_2Cu_3O_{7-x}$ with a superconducting transition temperature, T_{SC} = 95 K, in 1986 was extremely shocking and revolutionary[12]. In order for superconductivity to be feasible at this temperature, it was presumed that another pairing mechanism is responsible – something distinctly different from electron-phonon pairing, hence "unconventional". Many other superconductors have emerged where the pairing mechanism is unconventional, but the cuprate family of superconductors (those, like $YBa_2Cu_3O_{7-x}$, that are based on copper oxide planes) were the only known "high temperature" superconductors: those known to exceed the BCS limit of ∼35 K.

While many features of cuprate superconductors can be described with a modified version of BCS theory [13], the unpredictably high transition temperatures necessitate that there are some features that do not fit into this framework. The most notable is the anisotropy of the superconducting gap, shown in Fig. 1.5. While most conventional superconductors have an isotropic, *s*-wave gap, the structure of the gap in cuprates is *d*-wave. As shown in Fig. 1.5(a),

the gap changes sign as one moves around the Fermi surface and nodes are present along the ($\pm\pi$,$\pm\pi$)-directions, where the superconducting gap goes to zero. This was first seen by nuclear magnetic resonance spin-lattice relaxation rate measurements [14], and confirmed by subsequent microwave resonator measurements [15], then by μSR [16] and tri-crystal experiments [17]. The nodes in the gap lead to quasiparticle excitations that exist within Δ of the Fermi energy. Later, this pairing symmetry was confirmed by phase sensitive tunnelling experiments [18, 19, 20] and angle-resolved photoemission (Fig. 1.5(b)) [21].

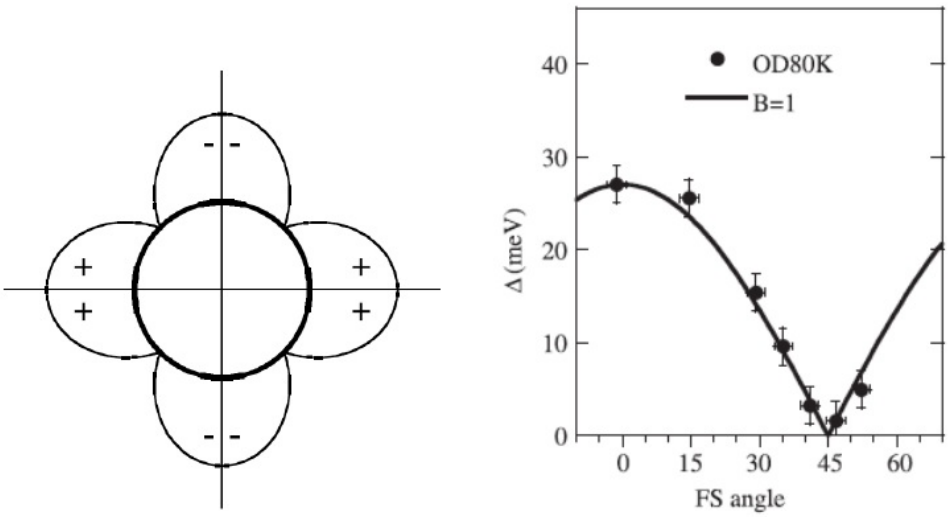

Figure 1.5: (a) A plot of the *d*-wave superconducting gap on a circular Fermi surface. Note the nodal points at which the gap changes sign. (b) The angular dependence of the gap energy as measured by ARPES in Bi-2212. Figure taken from [21] and used with permission.

Other unconventional aspects of the cuprate superconductors are the linear dependence of superfluid density [22] and magnetic fluctuation commensurability [23] on T_{SC}, known as the Uemura and Yamada relations, respectively. The high transition temperatures suggest that the mechanism of Cooper pairing in the cuprates is not the conventional electron-phonon interaction. Due to the relationship between T_{SC} and the magnetic fluctuations (in addition to the close proximity to magnetic order), a number of theories emerged that suggested that magnetic excitations may be the pairing mechanism in these materials [24]. There is an emerging consensus that spin fluctuations are the pairing mechanism responsible for high temperature superconductivity, but no comprehensive theory has yet emerged to describe this phenomenon [21, 25].

1.2 Iron Pnictide Superconductivity

The cuprate superconductors continue to be widely studied in an attempt to understand the nature of their pairing mechanism. However, a new avenue of research emerged in 2008 with the discovery of several of Iron pnictide superconductors based on layers of FeAs, with superconducting transition temperatures of up to 55 K [26]. These are another family of high-temperature superconductors, and so they form a natural basis for comparison to the cuprates. One of the most significant comparisons came when studying the phase diagram of the Iron pnictide superconductors. The pnictide phase diagrams appear very similar to those of the cuprates, where superconductivity appears only after electron- or hole-doping an antiferromagnetic parent compound.

The structure of these families are shown in Fig. 1.6, while a representative phase diagram is shown in Fig. 1.7 [27].

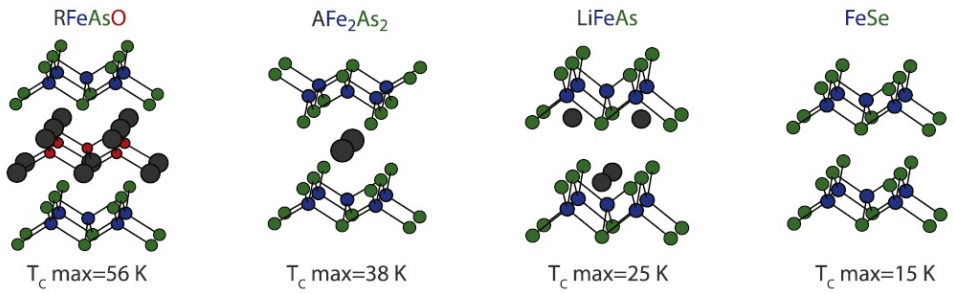

Figure 1.6: The structure of the various families of Iron pnictide superconductors. Figure taken from [27] and used with permission.

Of these families, the AFe_2As_2 family has received considerable attention due to the relative ease of growing large single crystals. This is important for measurements that depend on the size of the sample being measured, such as neutron scattering and to a lesser extent, muon spin relaxation. Superconductivity can be induced in several ways in these compounds: using rare-earth doping on the A-site, transition metal doping for Fe and using hydrostatic or uniaxial pressure [28]. Remarkably, all of these have very similar phase diagrams, which indicates that the chemical substitution does more than modify the carrier concentration by adding or removing electrons. This is another motivation to study this family of pnictide superconductors, since the wide variety of perturbations to the system may be probing the same physics. Hopefully, a comprehensive study of these perturbations may yield insight into the salient physics.

The parent compounds, AFe_2As_2 (A=Ba,Sr,Ca), display a first order phase transition from a high-temperature paramagnetic, tetragonal phase to a low-temperature orthorhombic, antiferromagnetic phase [29, 30, 31, 32, 33]. This is clearly seen in transport and thermodynamic measurements, shown in Fig. 1.8. This is accompanied by an $\sim$1 K thermal hysteresis in the orthorhombic splitting and Bragg peak intensity as seen by neutron scattering [34, 35].

The small peak and sharp drop in the resistivity below T_N points to a loss of scattering and a decrease in the density of states at this transition [28]. Following this behaviour under different chemical substitutions is important to understanding the effect of these dopants on the system.

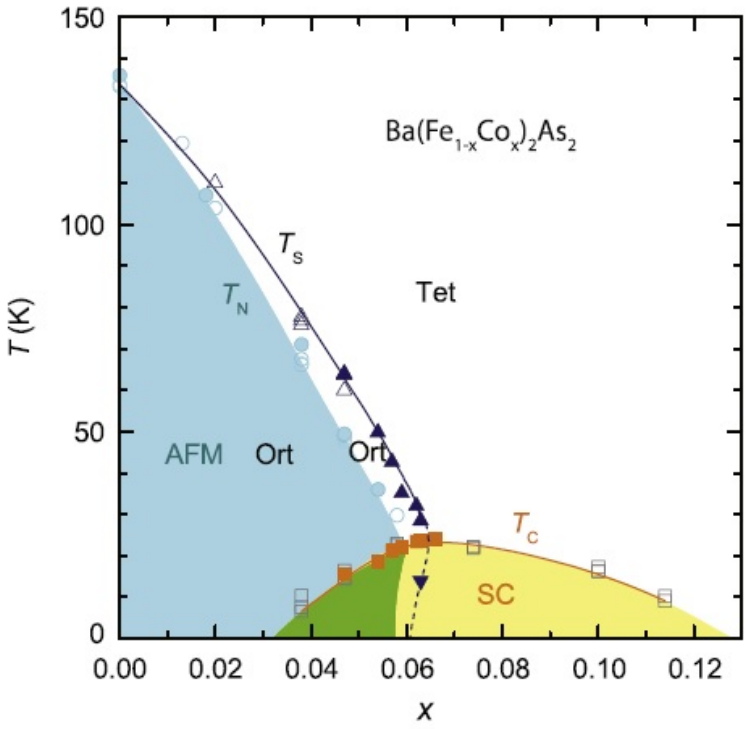

Figure 1.7: The phase diagram of $Ba(Fe,Co)_2As_2$. Most notable is the similarity to the cuprate phase diagram where superconductivity is also in close proximity to the antiferromagnetic phase of the parent compound. Figure taken from [27] and used with permission.

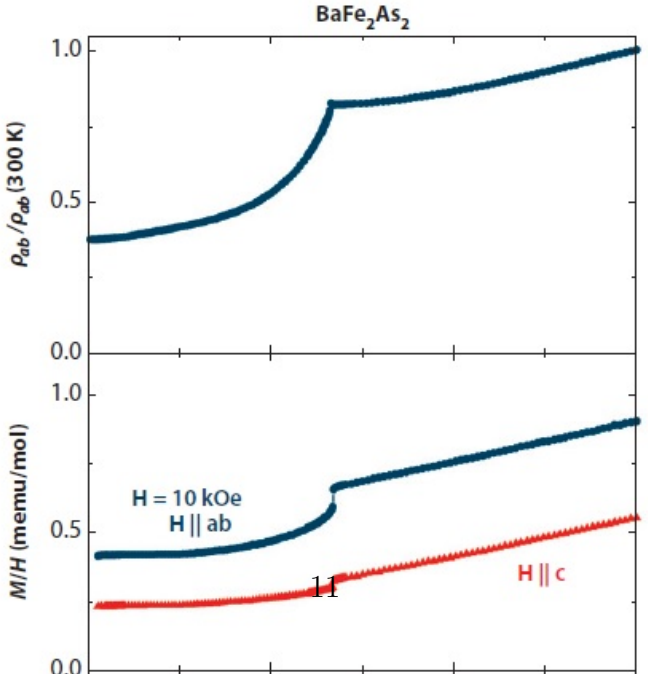

1.3 Experimental Survey of $Ba(Fe,Co)_2As_2$

One of the first members of this family to be successfully grown was using Barium as the rare earth ($BaFe_2As_2$) and doping Cobalt for Iron. This is unusual for a high-temperature superconductor, since it involves doping in the FeAs plane. In the cuprates, any dopant introduced into the CuO plane rapidly destroys superconductivity [36, 37]. Quite the opposite, the Iron pnictides appear very robust against this disorder, and the resulting superconducting phase has been shown to be quite homogeneous. The pnictides are usually grown from self-flux (FeAs) [38, 39, 40, 41], resulting in crystals of up to 1 x 1 x 0.2 cm^2 [28]. Using chemical analysis techniques, it has been shown that transition metal dopings, and in particular Co-doping, produces much more homogeneous doping than alkali doping on the A-site [28].

One of the first things to note is that the co-incident structural and magnetic transitions in $BaFe_2As_2$ split upon Co-doping the material. This is true of all the transition metal dopings, where both transitions are suppressed, but the antiferromagnetic transition is suppressed more rapidly. As Co replaces Fe, the signatures of the structural and magnetic transitions change shape in both resistivity and magnetization. The resistivity anisotropy is much larger ($\sim$2%) than the orthorhombicity ($\sim$0.1%) [42], implying that the electronic anisotropy is driving the structural transition. It is also noteworthy that the symmetry of the 3D spins ($\mathbb{O}(3)$) cannot be broken in 2D. However, neutron scattering has shown that the underlying antiferromagnetic structure to be either (π,0) or (0,π) [43], breaking the tetragonal symmetry, which Fernandes

et al. suggest as the explanation for why the structural transition necessarily occurs first [42].

At Co dopings above $x \sim 0.03$, superconductivity appears while the magnetism and orthorhombic phase are still being suppressed. The superconducting T_{SC} reaches a maximum around $x = 0.061$ in $Ba(Fe_{1-x}Co_x)_2As_2$, coincident (or nearly so) with the loss of orthorhombic and magnetic order. The structural phase transition and superconductivity also seem to be related through the anisotropy of the upper critical field, H_{c2}. The anisotropy is largest at higher dopings, while the most dramatic change in the anisotropy seems to take place at the loss of orthorhombic order [38].

The thermoelectric power and Hall coefficient also demonstrate dramatic changes around the onset of superconductivity and the loss of orthorhombicity. Shown in Fig. 1.9, they both suggest large distortions in the Fermi surface properties above $x = 0.24$ [44]. This is also seen in Cu- [44] and Ni-doped [45, 46, 47] compounds at the same level of electron doping. This has been confirmed by angle-resolved photoemission, which sees large changes in the Fermi surface pockets between $x = 0.24$ and 0.38, and which are most pronounced at low temperatures, but have been seen up to 150 K [48]. The interpretation of the data is that the top of the hole band moves below the Fermi energy above this doping.

Optical spectroscopy measurements have seen two Drude contributions to the *ab*-plane optical spectroscopy of $Ba(Fe,Co)_2As_2$ [49, 50]. The first "narrow" one has a small relaxation rate, $1/\tau$, while the second "broad" one has a larger relaxation rate. Both of these current carriers can contribute to the su-

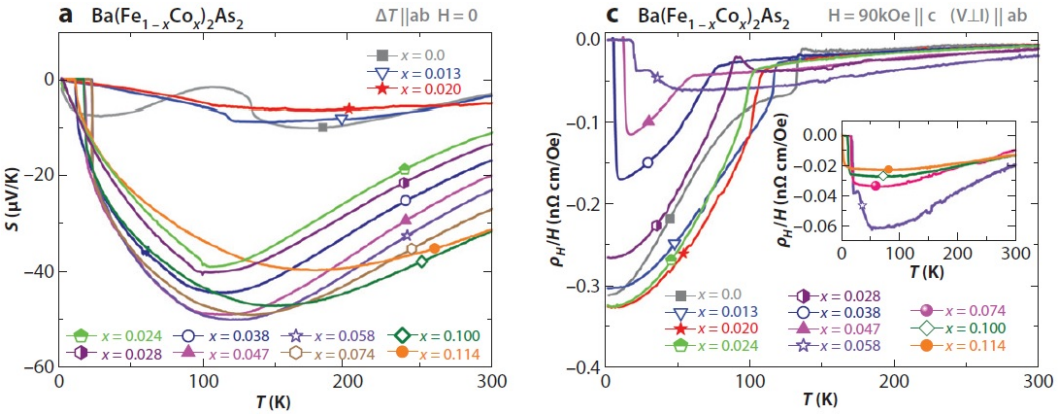

Figure 1.9: Thermoelectric power (left) and Hall coefficient (right) measurements over a range of Co-dopings. Dramatic changes are seen above $x = 0.24$, suggesting a topological change or distortion in the Fermi surface, coinciding with the onset of superconductivity. Figure taken from [44] and used with permission.

perconducting condensate, each with its own superconducting gap [50], which agrees well with the concept of multiple superconducting gaps in these materials (see below). Furthermore, strong-coupling theories predict the existence of two electronic carriers, with one set of carriers being low-energy carriers near E_F [51, 52]. Due to the difference in energy, these carriers could not be represented by a single Drude term in the optical conductivity [53].

Nuclear magnetic resonance measurements have observed a spin susceptibility, χ_{spin}, that increases monotonically with T and decreases with Co-doping [40, 54]. The value obtained for the parent material is close to the total susceptibility, suggesting that the orbital contributions to the susceptibility are small at high temperature. The increase in χ_{spin} with T has been interpreted in terms of a pseudogap, however measurements of this feature

by inelastic neutron scattering have not yet been attempted at the required energy transfer of ∼40 meV [55].

Neutron scattering measurements have found a substantial reduction from the free energy moment that would be present for a local moment system ($S = 2$ gives $\mu_{eff} = 4.9\ \mu_B$/Fe). The measured $\mu_{eff} = 0.28\ \mu_B$/Fe suggests that frustration and/or fluctuation effects suppress the moments in the antiferromagnetically-ordered state [55]. Magnetic excitations were also observed above T_{SC} at the antiferromagnetic wavevector and were indicative of quasi-two-dimensional spin fluctuations [56]. These fluctuations were present up to 200 K, where they had decreased to roughly 1/4 intensity.

Further neutron scattering measurements have found the magnetic structure present in the material for lightly-doped samples. For dopings below $x = 0.056$, the material exhibits a commensurate, $\vec{Q}_{AF}$ =(1 0 1) SDW static magnetic order [57, 58, 59]. For dopings ranging from $0.056 < x < 0.06$, the magnetic order becomes incommensurate in the transverse direction. The magnetic ordering vector $\vec{Q}$=(1 0±ϵ 1) shows an incommensurability, ϵ, that increases with increasing doping. However, the magnetism is still long-range and well-ordered [60]. Above $x = 0.06$, neutron scattering sees no long-range magnetic order. The phase diagram constructed from neutron scattering in this doping range is shown in Fig. 1.10.

These observations are somewhat in contrast to nuclear magnetic resonance [40, 61] and Mössbauer [62] measurements, that find disordered magnetism that becomes more disordered at higher dopings. One possible reconciliation is that magnetic fluctuations may exist on timescales to which neutron

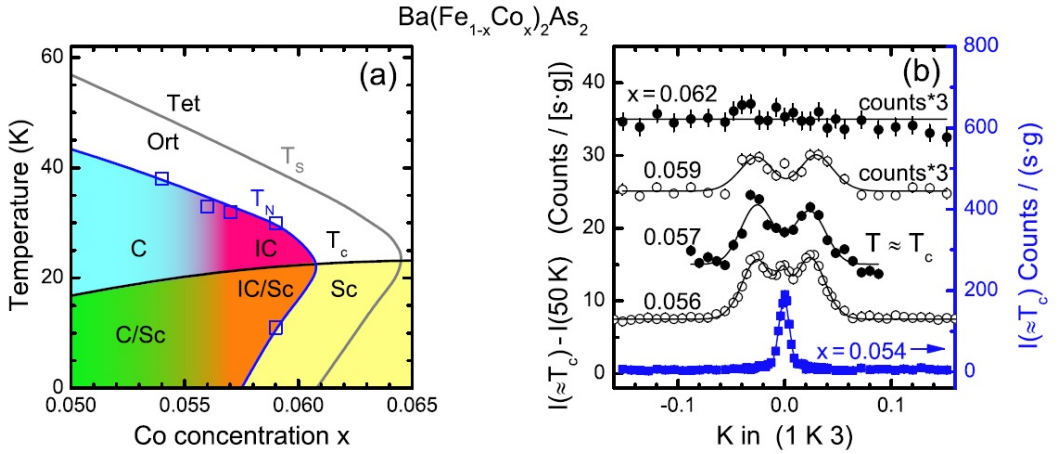

Figure 1.10: (Left) The phase diagram in the doping region near where static magnetism disappears. It shows the turnover of the magnetic and structural transitions, and the region in which the incommensuration appear. (Right) The neutron scattering measurements showing the change from commensurate to incommensurate order, and then to the loss of magnetic order at higher dopings. Figure taken from [60] and used with permission.

scattering are insensitive, but there may be other reasons for the differences in these observations.

Finally, it is important to comment on the issues with which this section began: the nature of the superconducting pairing mechanism and the gap symmetry. As in the cuprates, the high transition temperatures in the pnictides presuppose an unconventional type of pairing. In addition to magnetic fluctuations as the pairing mechanism, many other types have been proposed [63, 64], but this remains an open question.

The question of the gap symmetry, however, has progressed much further. Shown in Fig. 1.11 is the Fermi surface structure of electron- and hole-doped $BaFe_2As_2$, determined by LDA calculations [65]. This shows the two sets of

circular Fermi surface pockets, one at the Γ-point and one at the M-point. The theoretical proposal was that both of the sheets have a superconducting gap below T_{SC} [66, 65]. Whether these gaps were s- or d-wave and whether there was a phase difference between them was clarified by experiment.

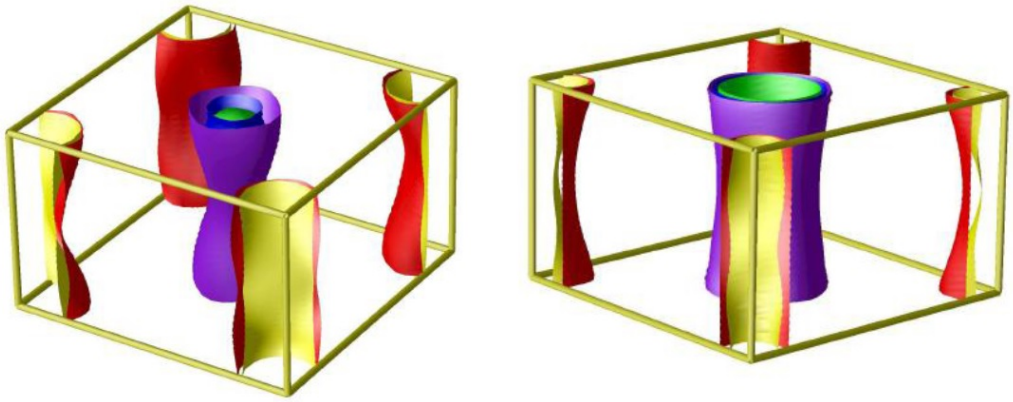

Figure 1.11: The Fermi surface structure of electron-doped (eg. $Ba(Fe,Co)_2As_2$, left) and hole-doped (eg. $(Ba,K)Fe_2As_2$, right) pnictide superconductors. Note the two sets of spherical Fermi sheets connected along $(\pm\pi,\pm\pi)$. Figure taken from [65] and used with permission.

Triplet pairing symmetries were ruled out by experiments fairly early [63], which excluded p- and f-wave gap symmetries. In a 3D system with tetragonal symmetry, only s, $d(xy)$, $d(x^2-y^2)$ and $d(xz \pm yz)$ are possible, and all of these d-wave symmetries must have gap nodes since the Fermi surface is quasi-two-dimensional [63]. Measurements of weakly-coupled Josephson junctions failed to see a spontaneous current that would be created in a system with gap nodes [67]. Gap nodes would also appear as orbital frustration in scanning SQUID measurements, which have not been seen in pnictide super-

conductors [68]. Both of these measurements suggest that the gap symmetry is likely s-wave.

Since we have two Fermi surfaces that each have an s-wave superconducting gap, it leaves two possibilities: they have the same phase, or they have a π-phase shift between them: called the s_{++} and $s_{\pm}$ states, respectively [66]. Several measurements have suggested that the $s_{\pm}$ state is the most likely candidate. A schematic of these two models is shown in Fig. 1.12.

First, inelastic neutron scattering measurements have observed a resonance peak at (π,0), which should only be present where this scattering vector produces a change in sign of the superconducting gap [69, 70]. This was detected in many different compounds across several pnictide families, suggesting the gap structure was a common feature of the pnictide superconductors. Additionally, measurements utilizing Josephson junction arrays [71, 72], quasiparticle interference [73, 74] and penetration depth all seem to be consistent with the $s_{\pm}$ model. The last of these quantities is the main parameter that is studied in Chapter 4.

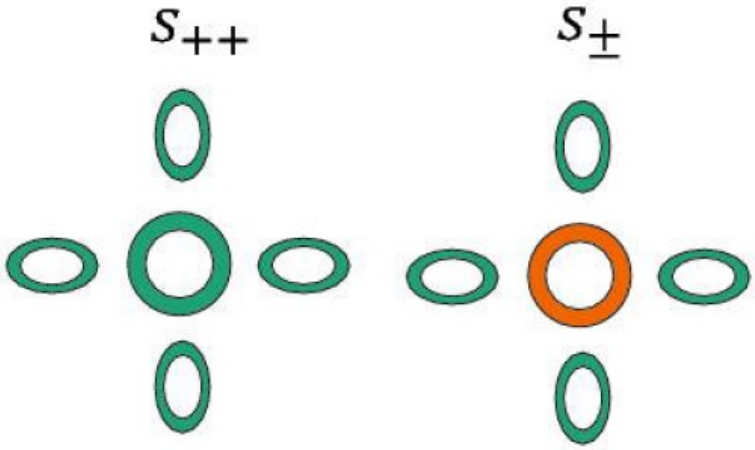

Figure 1.12: A schematic of the s_{++} (left) and $s_{\pm}$ (right) states. In the latter case, we see the sign changes as we move along the (π,0)-direction. Figure taken from [63] and used with permission.

Chapter 2

Introduction to URu_2Si_2

2.1 Heavy Fermion Materials

Heavy fermion materials are systems containing strongly-correlated electrons, and are so-named due to the large effective masses of the conduction electrons. This typically arises due to highly-localized *f*-electrons, so these materials are generally based on intermetallics such as Ce, Yb, and U, though not exclusively. At normal temperatures, these materials are ordinary paramagnetic metals, with weakly interacting magnetic moments. When the temperature is decreased, the moments created by the *f*-electrons become strongly coupled to the conduction electrons [75], hybridizing and forming the heavy fermion state. This increases the effective mass of the conduction electrons, to values that are 10 to 100 times the bare electron mass. This mass enhancement is clearly observed in a large electron contributions to the specific heat at low temperatures [76], thermal conductivity [77, 78] and heavy quasiparticles in the de Haas-van Alphen (dHvA) effect [79], as well as other quantum oscillation measurements.

The leading description of the heavy fermion phenomenon involves the competition between the Ruderman-Kittel-Kasuya-Yosida (RKKY) interaction and the Kondo Effect. The RKKY interaction is based on the existence of an indirect exchange through the polarization of the conduction electrons [80, 81, 82]. The Kondo interaction is an antiferromagnetic exchange between the localized and conduction electrons, leading to the enhancement in the effective mass [83]. This can occur between conduction electrons and a single magnetic impurity, or a lattice of magnetic ions. In the latter case, the lattice of magnetic atoms is called a Kondo lattice. This also appears as a reduction in the effective moment size in the system [84]. In *f*-band intermetallics, these atoms appear as magnetic moments with a large screening cloud, which changes between the high- and low-temperature regime. The cross-over between these two regions occurs due to a competition between inter- and intra-site interactions [85]. These interactions are both related through a common exchange coupling between the conduction electrons and local moments [84]. This cross-over appears in transport measurements as a maximum in the resistivity of the material, and indicates a loss in inelastic scattering below the cross-over [84].

The competition between the RKKY and the Kondo interactions depends on the same coupling parameter, since they both involve coupling of the *f*-electron moment and the conduction electrons. While the Kondo effect screens local moments, tending to a non-magnetic state, the RKKY interaction favours long-range magnetic order. This competition results in a phase diagram in which a magnetic region can form for a range of coupling constant values at low temperature, which has been dubbed the Doniach model [86]. This

phenomenon leads to materials with many interesting possible ground states, depending mostly on the strength of the interactions. The ground states are usually magnetic (both antiferromagnetic and ferromagnetic have been observed), superconducting, or in some cases, non-magnetic [75]. Table 2.1 shows some of the heavy-fermion materials, and their ground state.

		Ordering Temperature (K)
Antiferromagnetic		
	$UPtGa_5$	27.00
	$UAgCu_4$	18.15
	UCu_5	15.20
	U_2Zn_{17}	9.70
	UCd_{11}	5.0
	$U_{0.97}Th_{0.03}Be_{13}$	0.40
Ferromagnetic		
	UGe_2	52.00
	URhGe	9.50
	UCoGe	2.50
No Ordering		
	$UAuPt_4$	0.15
	$CeAl_3$	0.02
	$CeCu_6$	0.02
	UAl_2	0.02
	LiV_2O_4	0.02

Table 2.1: Ordering temperature of various heavy fermion materials with different ground state configurations. In the non-magnetic materials, the temperature stated corresponds to the lowest measured temperature. Data taken from [75, 87, 88].

The variations in the magnetic ground states in these materials is a result of the competition between the RKKY interaction and the Kondo effect. Since

they both depend on the same exchange interaction, J, between the *f*-electron moments and the conduction electrons, materials with different values of J may have different magnetic ground states. For example, in intermetallic Uranium compounds, the exchange parameter J depends in part on the inter-Uranium distance, d_{U-U}. For $d_{U-U} > 3.6$ the compounds are generally magnetic at low temperature, while for $d_{U-U} < 3.4$ the compounds generally have a non-magnetic ground state [89].

It is this complex electronic structure that accounts for the wide variety of phases seen in heavy fermion materials, including magnetism and superconductivity. However, the most complex phase arising in these materials seems to be the elusive 'hidden order' phase of URu_2Si_2, one of the two major areas of this thesis.

2.2 URu_2Si_2 and Hidden Order

URu_2Si_2 is a material having a tetragonal structure, space group I_{4mmm}, of the $ThCr_2Si_2$-type structure [90]. This structure is shown in Fig. 2.1. Interest in studying this material began in 1984 [91], when specific heat measurements clearly showed two transitions, one at $T_0 = 17.5$ K and the other at $T_{SC} = 1.2$ K [92, 93] (See Fig. 2.2). The lower transition was quickly identified as a superconducting transition, but the upper transition was a cause for debate. To date, the order parameter of this phase has not been identified, leading to the adoption of the term 'hidden order' phase to describe it.

As seen in Fig. 2.2, the contribution to the specific heat from this phase transition is quite large, approximately $0.2R \ln 2$. If this were a magnetic phase

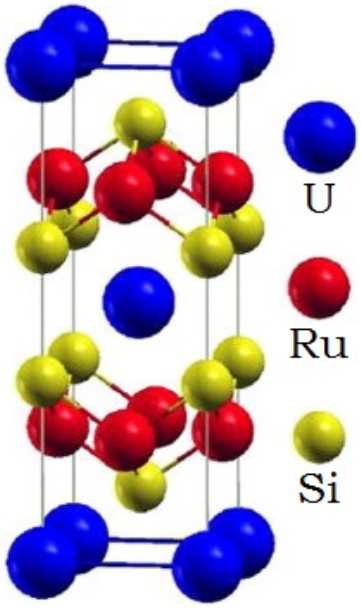

Figure 2.1: The structure of URu_2Si_2. It is tetragonal, space group I_{4mmm}, with the $ThCr_2Si_2$ structure.

transition, the size of the ordered moment required for this entropy change is easily detectable with a magnetic probe such as neutron scattering.

The magnetic susceptibility is shown in Fig. 2.3, which exhibits strongly Ising-like behaviour along the c-axis. The fit to a Curie-Weiss law gives a temperature $\theta_{CW} = -65\ K$ [94], indicative of moderate-strength antiferromagnetic correlations between the moments. The susceptibility deviates from the Curie-Weiss behaviour below T $\approx$ 150K, with a maximum occurring at $T^\star \approx 60$ K [95]. This is generally taken to be the coherence temperature, where the heavy electrons begin to form the heavy Fermi liquid. Approaching the hidden order state, the susceptibility drops and below T_0 it plateaus, clearly different from the behaviour of a conventional magnetic system.

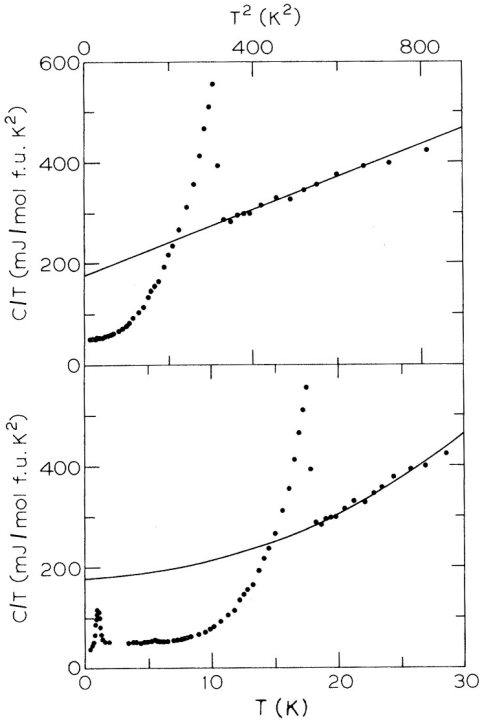

Figure 2.2: The specific heat of URu_2Si_2. This shows the phase transitions at $T_0 = 17.5$K and $T_{SC} = 1.2$K. This also demonstrates the fit to the large specific heat coefficient of $\gamma = 180$ mJ/mol K^2. Figure taken from [92] and used with permission.

Finally, resistivity demonstrates a complementary picture. Shown in Fig. 2.4, the high-T behaviour (top panel) shows the onset of lattice coherence at $T^\star$, while the low temperature behaviour (lower panel) shows the onset of superconductivity at $T_{SC} = 1.2$ K. It has been shown that the transport properties are not significantly affected by sample quality issues, with the coherence temperature and hidden order transition being quite robust against impurity-induced disorder. However, the low-temperature properties, most notably the resistivity, are affected by the purity of the starting materials [95]. The superconducting transition temperature has been shown to vary in the range of

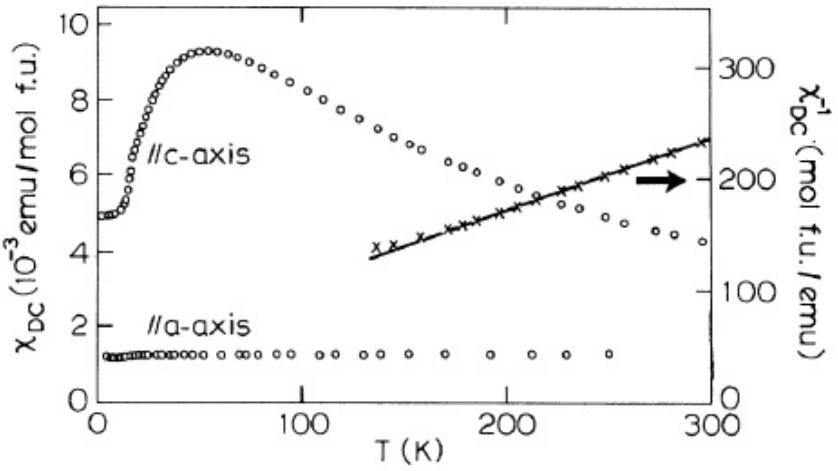

Figure 2.3: The susceptibility of URu_2Si_2 as a function of temperature. This indicates a $\hat{c}$-axis, Ising-like magnet, with Curie-Weiss behaviour above T = 150 K. From the high-T data, we see that T_{CW} = -65 K and the coherence temperature, $T^{\star} \approx 60$ K. We also see a drop and a plateau in the susceptibility around the hidden order transition. Figure taken from [94] and used with permission.

0.8 K to 1.5 K depending on the sample quality, but the hidden order transition is unaffected [96, 97].

As previously mentioned, the hidden order phase has been so named for the elusive order parameter present below T_0 = 17.5 K. In an attempt to explain the nature of this phase, many theories have been proposed – too many to describe in detail here. They range from higher-order magnetism (Quadrupolar ordering [98], Hexadecapolar order [99, 100] or higher), Charge- [101] or Spin- [102] density wave states, Modulated spin liquids [103, 104], Spin nematics [105, 106], Spin resonance [107], Topological spin-orbit ordering [108], Hybridization waves [109, 110], Hastatic order [111] and many others. None

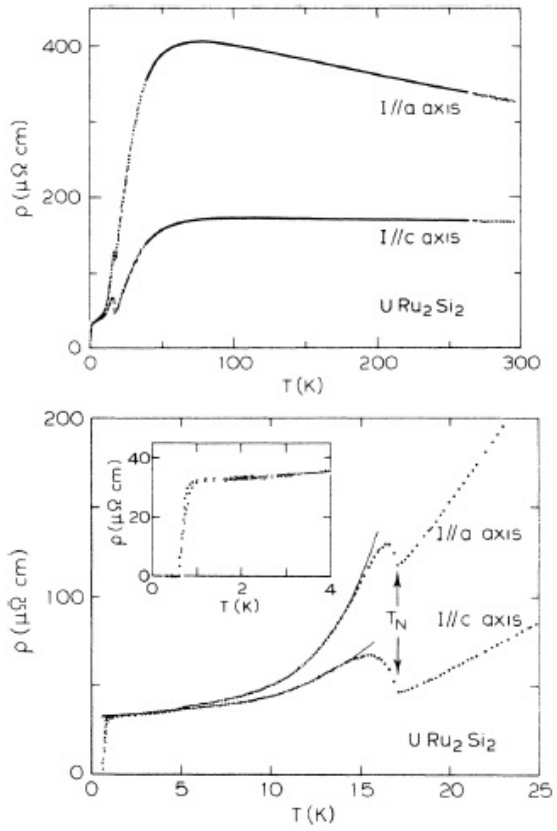

Figure 2.4: The resistivity of URu_2Si_2 as a function of temperature. Figure taken from [94] and used with permission.

of these theories have yet been proven correct, so it falls to experiments to distinguish between these many possibilities.

2.3 Experimental Survey of the Hidden Order Phase

The transport and specific heat measurements shown in Fig. 2.2 and 2.4 were consistent with a gapping of the Fermi surface. Fits to $C_e(T) \propto \exp(-\Delta/k_BT)$

in the hidden order phase gave a charge gap of $\Delta \approx 11$ meV with the gap opening over about 40 % of the Fermi surface [92, 93]. Hall effect measurements also saw evidence for the opening of a gap, accompanied by a sharp drop in the carrier concentration below T_0 [112]. Measurements of the coefficients of thermal expansion show peaks at T_0, indicating that the hidden order is coupled to the lattice [113].

Since many of the proposals for the nature of the hidden order state were magnetic in origin, neutron scattering was used to search for magnetic Bragg peaks [96, 114, 115]. These studies observed antiferromagnetism along the $\hat{c}$-axis, with alternating ferromagnetic ab-planes [96, 97]. However, several problems were observed with this magnetic structure. First, the magnetic Bragg peak intensity was quite small, corresponding to an ordered moment of $\mu \approx 0.04(1)\ \mu_B$/U. This was too small to account for the specific heat jump at T_0, and muon spin rotation (μSR) measurements gave an ordered moment that was an order of magnitude smaller than that [116]. Second, the observed magnetic correlation lengths were not resolution-limited, indicating that the magnetic ordering was not true long-range order. Third, the magnetic Bragg peak intensities did not show the temperature dependence that would be associated with an order parameter. And finally, the behaviour of the magnetic order was shown to have strong sample dependence – more than would be expected if the magnetic ordering were simply Neél order [95]. The common interpretation of these observations is that the small moments observed in the hidden order state are the result of stacking faults, due to the strong sample dependence. This was confirmed by μSR measurements that see spatially inhomogeneous regions of antiferromagnetic order [117, 118] and

nuclear magnetic resonance (NMR) measurements under hydrostatic pressure that similarly see antiferromagnetic regions with large (0.3 μ_B) moments [119].

The inelastic neutron scattering spectrum was measured to deduce the excitations present in this system. The first detailed study of these excitations found two distinct modes, one at the commensurate antiferromagnetic wavevector, $\vec{Q}_{com} = (1\ 0\ 0)$ and the other at the incommensurate wavevector $\vec{Q}_{inc} = (1 \pm 0.4\ 0\ 0)$ [115], shown in Fig. 2.5. This was later extended to a full inelastic measurement [120, 121, 122], shown in Fig. 2.6.

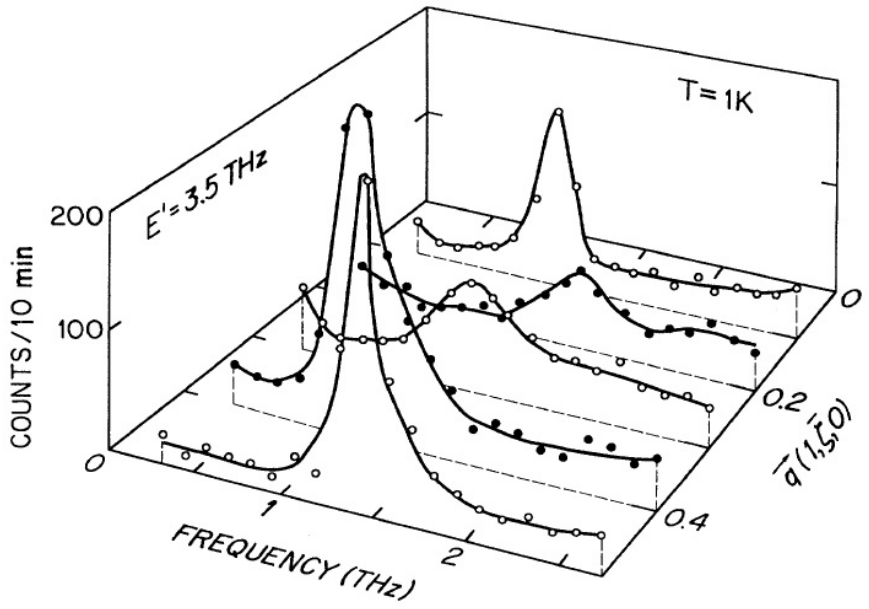

Figure 2.5: Neutron scattering measurements at various $\vec{Q}$ in the hidden order state. Both excitations are seen here: the commensurate $\vec{Q}_{com} = (1\ 0\ 0)$ dispersing in the top two cuts and the incommensurate $\vec{Q}_{inc} = (1\ 0.4\ 0)$ dispersing from that cut (2^{nd} from the bottom). Figure taken from [115] and used with permission.

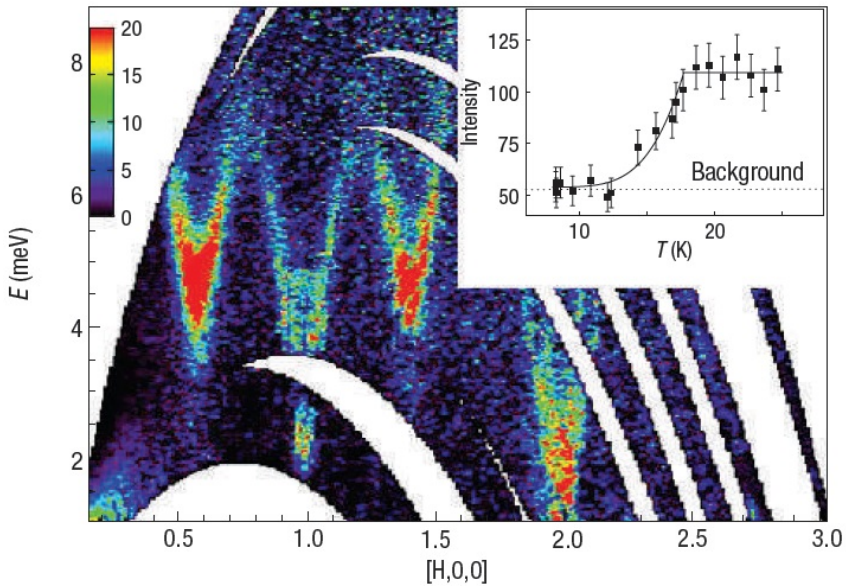

Figure 2.6: A series of inelastic neutron scattering measurements along the (H 0 0) direction, highlighting the excitations present in the hidden order phase. Here we see the gap in the incommensurate excitations, and the large spin wave velocities at both wavevectors. (inset) The quasi-elastic scattering at (1.4 0 0), showing the opening of the gap below $T_0 = 17.5$ K. Figure taken from [121] and used with permission.

The incommensurate modes are present in the paramagnetic phase ($T > T_0$), but are weak and sharply dispersing. It is believed that they are related to the heavy quasiparticles that form below the coherence temperature [121]. Below T_0, both modes appear much more strongly, with the incommensurate excitation acquiring a gap of 2 to 4.5 meV [115, 120, 121]. Although these were originally classified as magnon modes, they are longitudinal rather than transverse, which would be expected for low-energy spin fluctuations. It was shown by Wiebe *et al.* that the opening of the gap in the excitation spectrum at T_0 [120] would result in an entropy change on the order of that seen by

specific heat measurements. Furthermore, the opening of this gap was shown to behave in an order-parameter-like way [121], shown in the inset to Fig. 2.6. Finally, it was noted that as the temperature approaches T_0 from below, the commensurate mode softens and the damping increases, which rules out crystal field effects as an origin of the hidden order state [123]. While these observations do not solve the nature of the hidden order parameter, it has provided an avenue of research that is being studied intensely, both experimentally and theoretically.

To determine the Fermi surface structure within the hidden order regime, many quantum oscillations measurements were performed, both de Haas-van Alphen and Shubnikov-de Haas [124, 125, 126, 127]. Within the hidden order phase, three small closed Fermi surface pockets were observed [124], a drastic deviation from the large Fermi surface present in the paramagnetic regime. Later, a fourth, larger sheet was found, but only in an ultraclean sample [125]. Angle-dependent Shubnikov-de Haas measurements have seen a fifth pocket [126], as well as the splitting of one of the branches [127]. These measurements have been shown to be consistent with one another, establishing a clear picture of the Fermi surface in the hidden order state.

In addition to the sharp changes in Fermi surface properties, the carrier concentration, effective mass and scattering rate show very dramatic changes upon entering the hidden order state. Hall effect measurements show hole concentrations of 0.10 per U atom above T_0, which decreases to 0.02 per U atom below [112, 128, 129]. Nernst effect measurements also confirm the

increased scattering rate and a very low density of itinerant electrons that carry the large entropy. [130].

Many other probes have been brought to bear on the hidden order problem. Spectroscopic probes have been particularly useful in probing the nature of the hidden order state. Far-infrared reflectance also sees evidence for a charge gap and Fermi surface reconstruction in the hidden order state [131], which combined with the other probes mentioned produces evidence of both a charge and spin gap within the hidden order phase. More recent optical spectroscopy measurements have seen evidence of a hybridization gap that exists at temperatures above 40 K [132], pointing to a reconstruction of electronic states well above T_0. Scanning probe microscopy observes a Fano lineshape in the differential conductance [133, 134], suggesting a Kondo temperature of $T_K \approx 120$ K in this material. At T_0, the hidden order gap ≈ 5 meV appears within the Fano structure. The largest density of states was found near the U sites, and have been interpreted as evidence for hybridization of non-localized $5f$ electrons. These measurements have highlighted the need for new theoretical descriptions of the electronic structure around the U sites [95]. Finally, angle-resolved photoemission spectroscopy (ARPES) has been instrumental in studying various Fermi surface properties. Most notably, it was found that the differences in the electronic structure across T_0 reveal a doubling of the unit cell along the *c*-axis that occurs at the hidden order transition [135], a conclusion that is consistent with quantum oscillation measurements [127]. Time-resolved ARPES has also demonstrated the dramatic increase of the quasiparticle lifetime within the hidden order phase [136].

These experiments provide an extensive, but not yet complete, picture of the hidden order phase. While measurements of URu_2Si_2 are still on-going, the experimental study has branched out considerably to include the effects of chemical doping, applied pressure and applied fields. In fact, the studies have become so broad as to include multiple magnetic field orientations, both uniaxial and hydrostatic pressure, and chemical dopings of (U,Th)Ru_2Si_2, (U,Ce)Ru_2Si_2, U(Ru,Rh)$_2Si_2$, U(Ru,Re)$_2Si_2$, U(Ru,Co)$_2Si_2$ and U(Ru,Fe)$_2Si_2$ among others. The studies of these effects are too extensive to cover here, so the two that are relevant for this thesis will be explored: chemical doping of Re for Ru, and the application of hydrostatic pressure.

2.3.1 U(Ru,Re)$_2$Si$_2$

Chemical doping is a common way to probe the robustness of a system, and thus it has often been used as a probe for URu_2Si_2. Chemical substituents for Ru include Mn, Tc, Th, Re, Os, Rh, Ir and Fe. All except Fe act to suppress the hidden order, and except for Os, all of these suppress the hidden order by $\approx$ 5 % chemical doping [137]. Only Fe, Rh and Re have been studied at dopings beyond those needed to suppress the hidden order phase: Fe and Rh display antiferromagnetism that arises before the complete suppression of the hidden order phase. In contrast, Re doping has complete suppression of the hidden order phase, where a quantum critical point occurs at the border between hidden order and ferromagnetism (See Fig. 2.7).

The long-range nature of the ferromagnetic state has been confirmed by neutron scattering [138] and ^{29}Si nuclear magnetic resonance [139]. The mo-

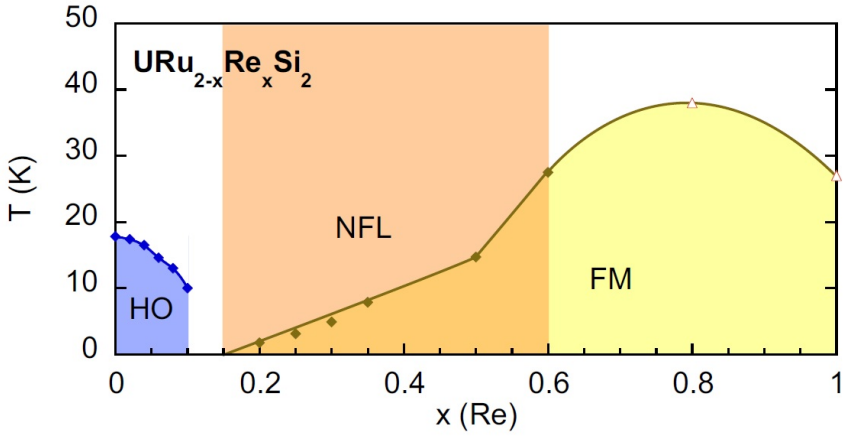

Figure 2.7: The phase diagram up to 50 % Re substitution. The hidden order is continuously suppressed, with a quantum critical point estimated around $x = 0.10$. A ferromagnetic phase then arises, which extend up to at least 50 % doping, but displays non-Fermi liquid-like behaviour. The quantum critical point and ferromagnetism are a departure from other chemical substitutions, where an antiferromagnetic phase usually emerges from within the hidden order dome. Figure taken from [137] and used with permission.

ments are small ($\approx 0.2\ \mu_B$ at $x = 0.5$) and itinerant, with no specific heat or electrical resistivity anomalies at the ferromagnetic transition, T_C [137]. At all Re dopings studied, including in the ferromagnetic region, the heavy fermion nature remains intact, with an enhanced electronic specific heat [140] and a narrow Drude peak in the optical conductivity at low T [141].

Around T_0, there are peaks in the electrical resistivity and specific heat, as shown in Fig. 2.8. The specific heat anomaly is still clearly present at dopings below $x = 0.12$, indicating that the Fermi surface gapping that occurs in the parent ($x = 0$) material continues to occur with light Re doping [93, 137]. Magnetometry measurements on the Re-doped series also display evidence for a transition to ferromagnetism between $x = 0.10$ and $x = 0.12$ [137].

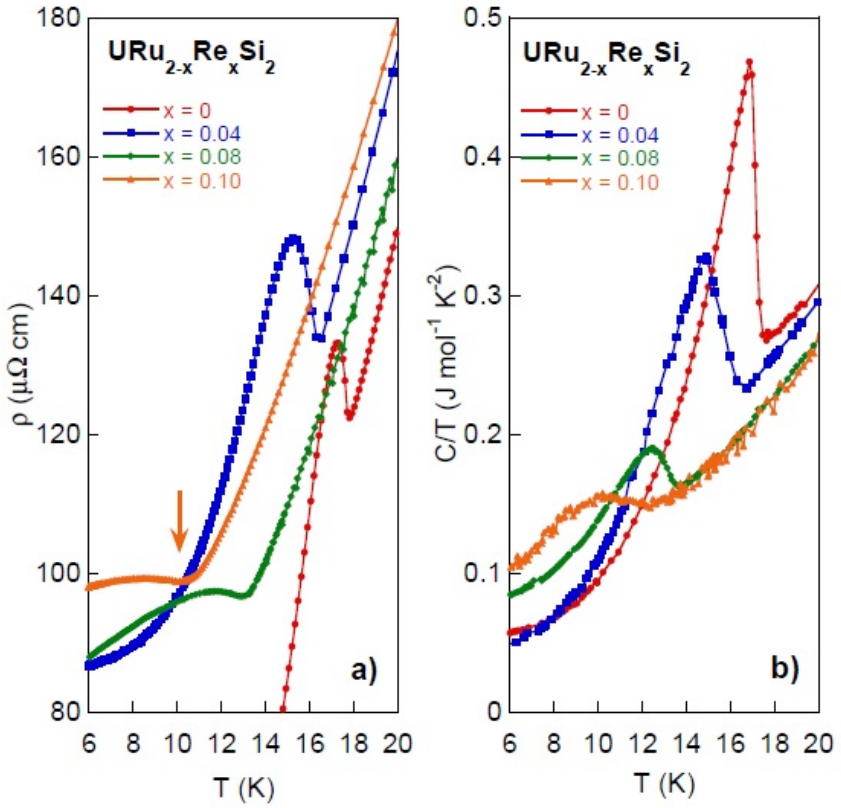

Figure 2.8: The electrical resistivity (a) and the specific heat (b) of $URu_{2-x}Re_xSi_2$ as a function of temperature. Both quantities display discontinuities as T_0. Despite the decrease in the transition temperature the features remain well-defined, suggesting that the gapping of the Fermi surface is fairly robust against this disorder. Figure taken from [137] and used with permission.

It is of interest to study the effects of Re doping on the other properties of the hidden order phase noted in Section 2.3. In this thesis, the spin excitations observed by neutron scattering were measured in one of the Re-doped samples. The results of this work are discussed in Section 5.2.

2.3.2 URu_2Si_2 Under Hydrostatic Pressure

Another perturbation which has been used to shed light on the nature of the hidden order phase is the application of hydrostatic pressure. This initially serves to strengthen the hidden order phase and increases T_0, as shown by specific heat measurements [94] in Fig. 2.9. This is a marked difference from other perturbations such as chemical pressure or applied magnetic fields that tend to destroy the hidden order phase. At higher applied pressures, a standard Neél ordered phase emerges from within the hidden order dome. Since this region has a larger antiferromagnetic moment ($\sim 0.4\ \mu_B$) than the hidden order region, it has been called the large moment antiferromagnetic (LMAF) phase. The pressure-temperature phase diagram is shown in Fig. 2.10.

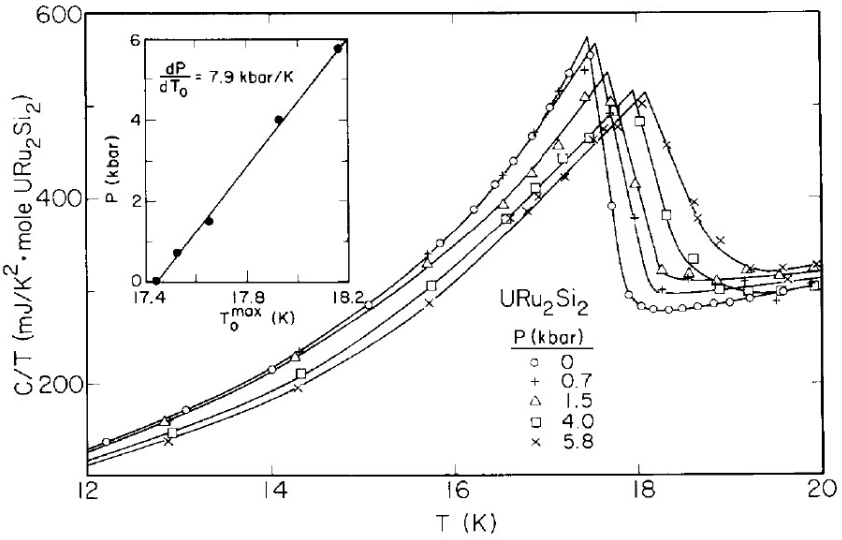

Figure 2.9: The specific heat of URu_2Si_2 as a function of pressure and temperature. This shows the phase transition at $T_0 = 17.5$K, which increases slightly with applied pressure. Figure taken from [94] and used with permission.

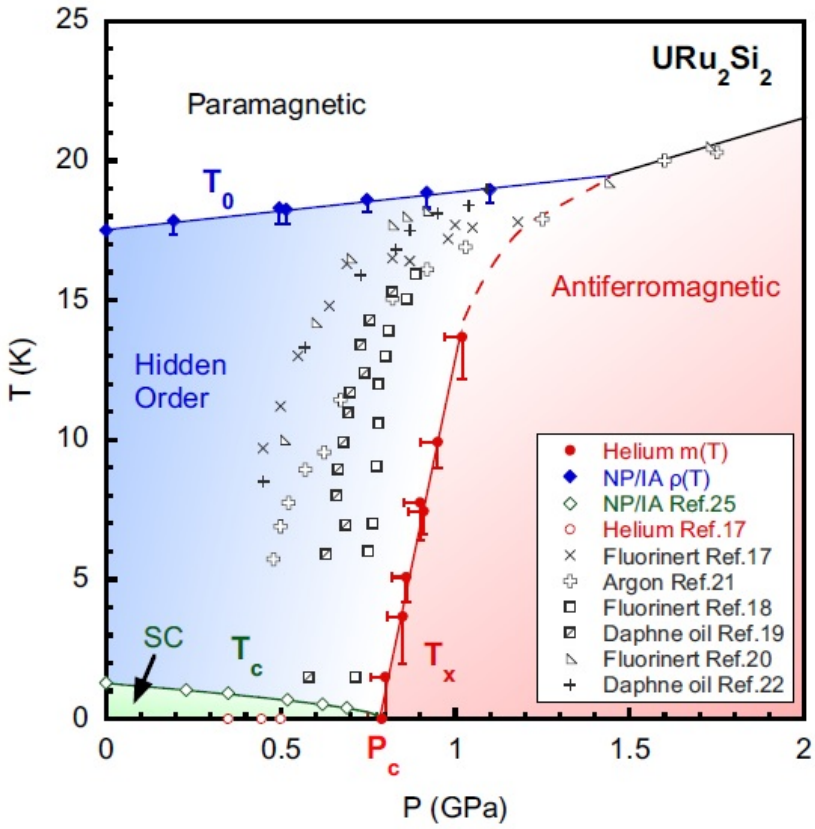

Figure 2.10: Pressure-temperature phase diagram of URu_2Si_2 using He as a pressure medium, compared to various other media. Applied pressure initially increases T_0 before an antiferromagnetic phase emerges above 0.5 GPa. It is suspected that superconductivity and antiferromagnetism meet at a multicritical point. Figure taken from [142] and used with permission.

Early resistivity measurements also saw the increase in T_0 with applied pressure, as well as finding an increase in the transport gap [143], with the hidden order gap being $\approx$ 70 % to 80 % of the LMAF gap [144, 145, 146]. And while the magnetic Bragg peak intensity jumps sharply at 0.5 GPa, there is no signature of this transition in resistivity or specific heat [95, 143, 147]. When pressure-dependent ^{29}Si-NMR measurements were performed, there was

evidence for phase separation between non-magnetic and LMAF regions, with the latter occupying just a few percent of the volume [119, 148]. This offers an explanation for the small moment seen by neutron scattering within the hidden order region, where impurities and defects create stress in the lattice constants. This pushes them past critical values and creates small, localized regions of the LMAF phase [95]. Though it is now believed that the hidden order region does not contain intrinsic moments, the LMAF phase has retained that name.

To observe any changes in the Fermi surface topology within the LMAF phase, quantum oscillation measurements were performed. Surprisingly, there was almost no change detected in the Fermi surface across the transition to the LMAF phase [127, 149], as shown in Fig. 2.11. The only noticeable change is a decrease in the cyclotron effective mass (Fig. 2.11(d)) due to the increase in the magnetic moment size. This is consistent with neutron scattering measurements, that observe the same nesting vector in the LMAF phase [150]. Combined with the lack of a specific heat peak, this suggests no Fermi surface reconstruction or entropy change between the hidden order and LMAF phases.

This suggests a remarkable similarity between the hidden order and LMAF phase properties. One aspect of the LMAF phase not yet discussed is the spin correlations and their similarities to those observed in the hidden order region. This is one of the topics of study in this thesis, thus these measurements and the comparison to other work of this type will be left for Section 5.3.

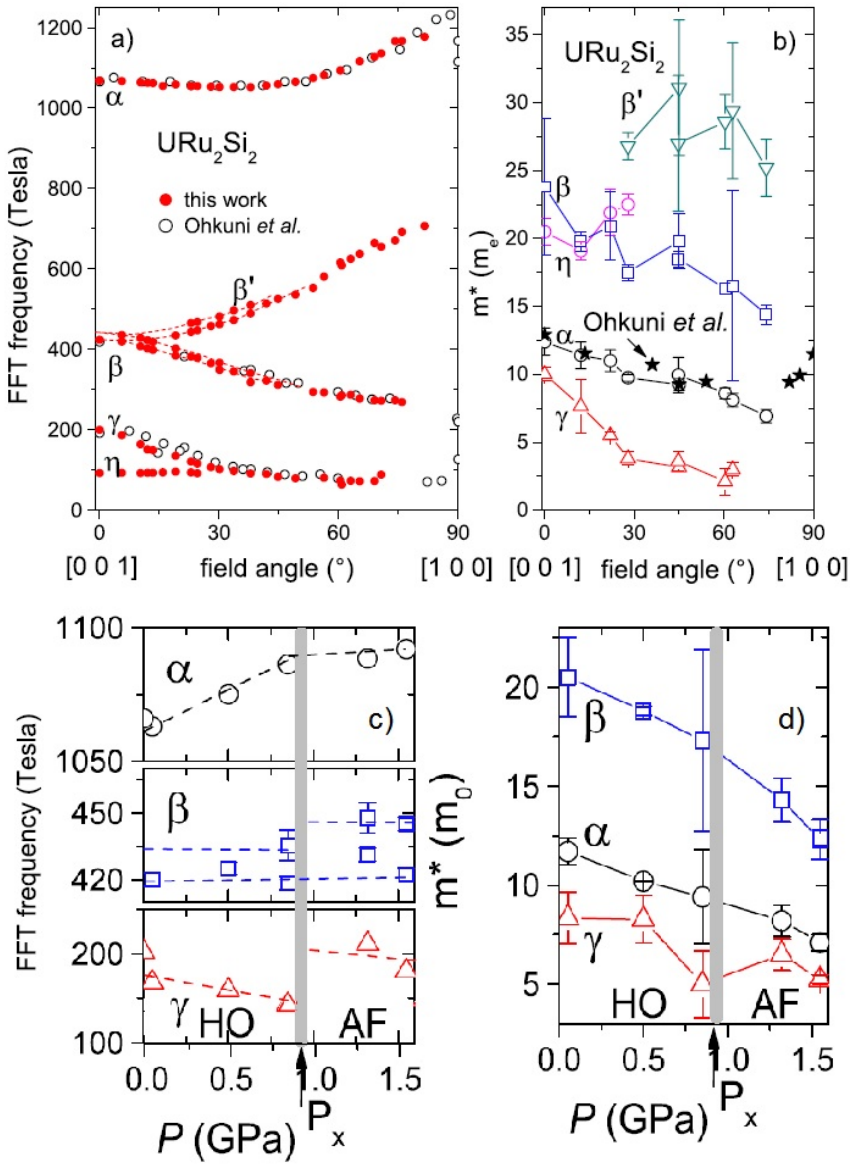

Figure 2.11: Shubnikov-de Haas measurements as a function of field angle (a & b, in the LMAF phase) and pressure (c & d, summed over the entire Fermi surface pocket). No dramatic changes in the Fermi surface are seen in the LMAF phase, and only slight changes in the cyclotron effective mass due to the increased moment size. Figure taken from [127] and used with permission.

Chapter 3

Experimental Techniques

This chapter will cover the three primary experimental techniques used in this thesis. First, the method of crystal growth will be discussed, in the capacity to which it was used by the author. Next, the two techniques of muon spin rotation/relaxation/resonance (μSR) and neutron scattering will be discussed, as they represent the primary measurements performed in Chapters 4 and 5, respectively.

While they will be discussed separately, it would be ignorant not to comment on the similarities and, more importantly, the complementary nature of the two measurement techniques. Both depend on the use of particles incident on the material to measure its electronic and magnetic properties. The complementary nature appears when we notice that μSR is a local, real-space probe of magnetism, while neutron scattering is a bulk, reciprocal space probe. They also work on slightly different timescales, allowing for a comparison of dynamical properties observed by both techniques. In this way, μSR and neutron scattering can provide complementary information about the properties of the system being studied, a theme that is highlighted by the results presented in this thesis.

3.1 Crystal Growth

For some of the neutron scattering measurements of URu_2Si_2, the measurements were performed on crystals grown at McMaster University using the Czochralski method, described below.

The samples were made with high-purity depleted Uranium (>99.9% Uranium, >99.5% ^{238}U) produced by electro-refinement at Ames Laboratory, high-purity Ruthenium (>99.99%) and Silicon (>99.999%). The constituents were mixed in stoichiometric amounts to achieve the ratio necessary to form URu_2Si_2. They were combined in a mono-arc furnace (shown in Fig. 3.1) and put through several cycles of melting and solidifying to ensure homogeneity of the materials.

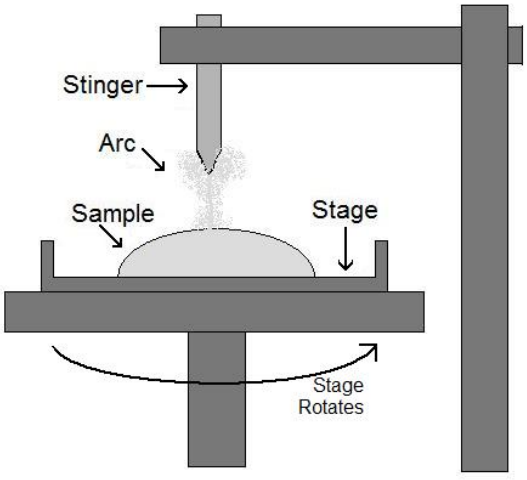

Figure 3.1: Schematic of the mono-arc furnace used for premelting of the samples. A welding arc from a high-voltage supply heats the material, which is in an inert Ar atmosphere.

In order to create larger single crystals, the resulting boule was placed into a tri-arc furnace (see Fig. 3.2). The crystal was grown using the Czochralski method in a continuously gettered Ar atmosphere. This method is commonly used to grow larger single crystals for both scientific and industrial applications, and is described in detail elsewhere [151].

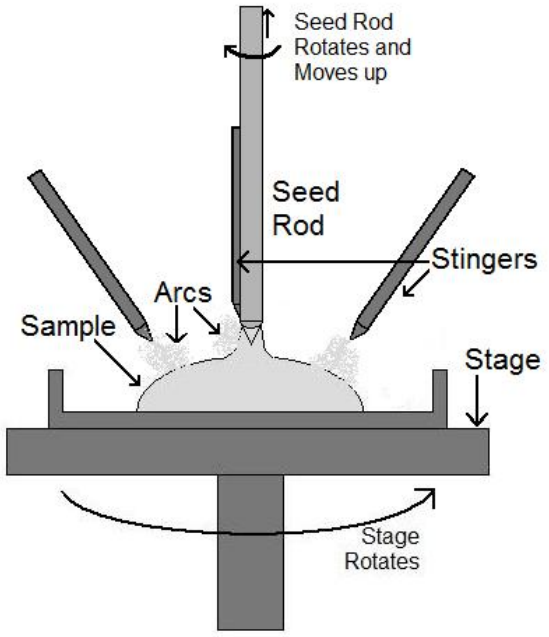

Figure 3.2: Schematic of the tri-arc furnace. The sample is placed on the stage and melted with the arcs. The seed rod is lowered into the sample, crystallizing material on it. As the seed rod is raised, more material solidifies, forming a long, single-crystalline rod.

In the apparatus used for growing URu_2Si_2 crystals here, the polycrystalline boule from the mono-arc furnace is loaded onto the stage and melted in an analogous way with three welding arcs. A water-cooled seed rod is then lowered into the sample, crystallizing some material. While the stage and sample rod

are counter-rotated to promote even heating and crystallization, the seed rod is slowly raised (∼20-30 mm/hr) producing a long rod that is mostly of a single grain.

For the neutron scattering experiments described in Chapter 5, the sample needed to be measured in the *ac*-plane. Since the pressure cell containing the sample could only be inclined $\sim 5°$, the crystal needed to be grown with the $\hat{b}$-axis within 5° of the growth axis. This was accomplished by taking a piece of URu_2Si_2 from a previous growth, and cutting it along this direction. This small (∼0.5 g) piece was attached to a specially-designed seed rod, allowing the piece to function as a seed for the growth to be attempted. The intention was to promote the growth of the larger crystal with this particular orientation.

This growth was attempted four times, resulting in the creation of a large, 8.4 g single crystal. The $\hat{b}$-axis was aligned 2.4° from the growth axis, allowing a piece of suitable size to be cut to fit the pressure cell. The Czochralski method tends to accumulate impurities near the end of the growth [151] and the beginning of the growth tends to be polycrystalline, so these parts were removed during the cutting process.

The final piece used for the measurements had a mass of 1.2 g, a size suitable for the measurements to be performed. Other pieces of the same sample were retained for further measurements, including electrical and thermal transport, magnetization and other spectroscopic techniques that were not a part of this work.

3.2 Muon Spin Relaxation/Rotation/Resonance (μSR)

3.2.1 Principles of μSR

The technique of muon spin relaxation/rotation/resonance (μSR) is one of the most sensitive experimental techniques for measuring local magnetic properties within a material. μSR is a local, real-space probe of condensed matter systems. It utilizes muons implanted in the sample to measure the response of the muons to the local magnetic field.

Muons are fundamental particles, a lepton like the electron, with which it shares many properties. The muon also has spin $S = \frac{1}{2}$ and a charge of $\pm e$. However, muons are much heavier, with a mass $m_\mu = 207\ m_e$ and consequently a larger gyromagnetic ratio, $\gamma_\mu = 135.54\ \frac{MHz}{T}$. They are also unstable, decaying with a mean lifetime $\tau_\mu = 2.197\ \mu s$ [152]. To generate muons used for these experiments, a proton accelerator is used to generate pions. This is done by colliding high-energy protons with a low-Z target. At TRIUMF, where the μSR measurements for this thesis were performed, the protons have an energy of 500 MeV and the target is Beryllium or Carbon. Three principle processes will generate pions in this case [153]:

$$p + p \rightarrow p + n + \pi^+ \tag{3.1}$$

$$p + n \rightarrow n + n + \pi^+ \tag{3.2}$$

$$p + n \rightarrow p + p + \pi^- \tag{3.3}$$

After a mean lifetime of 26 ns, they then decay via the weak interaction [153]:

$$\pi^+ \rightarrow \mu^+ + \nu_\mu \tag{3.4}$$

$$\pi^- \rightarrow \mu^- + \bar{\nu}_\mu \tag{3.5}$$

In the rest frame of the pion, weak decay can only produce left-handed neutrinos: neutrinos with spins that are opposite of their linear momentum. This is a feature of parity violation in the weak interaction. After generation, some pions migrate to the surface of the target. Pions themselves have no spin moment, so to preserve both linear and angular momentum, the muons must also be generated left-handed. Thus all of the muons generated through the processes above will have their spin antiparallel to their momentum, and so this produces a beam of nearly 100 % spin-polarized muons, with a kinetic energy of 4.119 MeV. While surface pions do not need to be used for μSR experiments, this produces the only fully-polarized beam, but also produces only positive antimuons. In addition, surface pions produce a muon beam that is quite luminous and at an energy that is very suitable for implantation into a sample.

It is these muon beams that are used for the μSR experiments in this work. Using magnetic steering and Wien filters, the muons can be implanted into a sample one by one. Since both muons (μ^-) and antimuons (μ^+) are produced in these processes, either type can be used for performing μSR experiments. Negative muons involve more complicated interactions and analysis, which is why nearly all μSR experiments tend to be performed using positively-charged antimuons [152, 153]. All of the μSR experiments in this these were performed with positively-charged, antimuon beams.

When the positive-muon is incident on the sample, it will stop within the sample at a position that is an electrostatic potential minimum. The muons will stop even in fairly thin samples, since the stopping range is fairly small, $\sim$120 mg/cm^2 in Carbon. This "muon site" is usually located near the negative ions in a sample (such as F^- or O^{2-}), but maybe not be crystallographically unique. Further, some experiments see evidence of muon "hopping": movement of the muons between muon sites, but this has been shown to be highly dependent on the structure and composition of a material [153]. When a muon is in a region of non-zero local magnetic field, it undergoes Larmor precession, with a frequency that is proportionally dependent on the magnitude of the local field and its gyromagnetic ratio [153]:

$$\nu = \gamma_\mu * H_{loc} \tag{3.6}$$

As noted above, muons are unstable, decaying with a mean lifetime of $\tau_\mu = 2.197$ μs. Positive muons decay through the weak interaction via the process [153]:

$$\mu^+ \rightarrow e^+ + \nu_e + \bar{\nu}_\mu \tag{3.7}$$

which gives off a positron and two neutrinos. The two neutrinos are not detected in the experiment, but information can be extracted by measuring the positron. Since this is also a weak decay process, it also violates parity. This is a three-body final state, and so there is a probability associated with the decay. The positron is ejected preferentially along the direction of the muon spin at the time of decay, with a probability distribution that depends on the energy of the positron [153]. This is shown in Fig. 3.3.

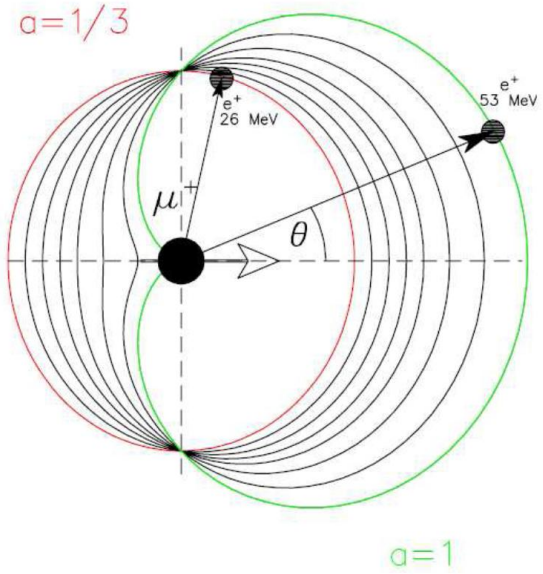

Figure 3.3: A representation of the probability distribution of the positron momentum produced from muon decay. When the positron carries all of the energy ($\sim$ 53 MeV, the rest energy of the muon) the decay is highly anisotropic. The distribution becomes more isotropic with lower energy, becoming completely symmetric at half the rest energy ($\sim$ 26 MeV). Figure taken from [154].

This distribution has a probability, W, that depends on the angle from the muon spin, θ, give by [153]:

$$W(\theta) = 1 + a(\epsilon)\cos(\theta) \tag{3.8}$$

where $a(\epsilon)$ is called the "asymmetry factor" and increases with the kinetic energy of the positron, ϵ.

The ejected positrons are detected by positron counters placed around the sample. These counters are largely insensitive to the positron energy and thus sum over all values of ϵ. However, the detectors have time resolution on the order of nanoseconds, and so the time taken from a muon entering to a positron being detected can be measured for each event. By counting many millions of positron events, a histogram of counts versus time for each counter can be created and the time dependence of the muon spin in the sample can be extracted. More details on how this is done, and the information gathered from this quantity will be discussed in the following sections.

3.2.2 Zero-Field (ZF)-μSR

The schematic of a Zero-Field (ZF)-μSR experiment is shown in Fig. 3.4. This type of experiment is generally performed with the muon spin antiparallel to its momentum, though a perpendicular arrangement can be used as well. Since ZF-μSR is performed, by definition, in zero applied magnetic field, the only difference between these two arrangements is the orientation of the muon spin with respect to the crystallographic orientation.

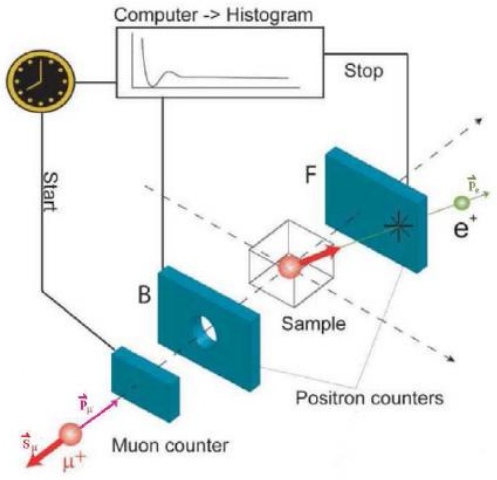

Figure 3.4: The experimental geometry of a ZF-μSR experiment. Here, we define $\hat{z}$ as being the beam direction, $\hat{y}$ is Up-Down and $\hat{x}$ is Right-Left. Figure taken from [154].

Prior to entering the sample, the muons pass through a thin scintillation detector, which acts as a signal to start a timer. As described above, the muon will stop in the sample and Larmor precess with a frequency given by Eq. 3.6. If $\hat{z}$ is the initial direction of the muon spin, then the z-component of the spin evolves in a manner described by [154]:

$$S_z(t) = \cos^2\theta + sin^2\theta \cos(\gamma_\mu H_{loc} t) \tag{3.9}$$

where $\cos\theta = \frac{\vec{H}_{loc}\cdot\hat{z}}{H_{loc}}$.

When the muon decays and emits a positron, it may be detected by one of the scintillation detectors around the sample. When a positron count is detected, it stops the timer, and so the time that the muon was precessing

in the sample can be determined. If no positron is detected, or two positrons are detected, the event is vetoed. Similarly, if another muon enters the sample before the positron from the previous muon is detected, the event is also vetoed.

Using the amount of time that the muon was in the sample, a histogram of the number of positron events in a counter versus time can be determined. For the geometry described in Fig. 3.4, the number of counts in the Forward/Backward counter pair is given by:

$$N_{B,F}(t) = N_{0B,F}[B_{B,F} + \exp(-t/\tau_{nu})(1 \pm A_{B,F}P_z(t))] \tag{3.10}$$

where the initial muon spin is in the Back ($-\hat{z}$) direction, and the +/- refer to the Back/Forward counter. $A_{B,F}$ are the intrinsic detector asymmetries for the Back or Forward counters, $N_{0B,F}$ are normalization factors and $B_{B,F}$ are time-independent backgrounds, which can be measured in the experiment. In general, $A_F \neq A_B$ and so we define $A_F = \beta A_B$. The factor β is difficult to measure experimentally, but except for very thick samples or where the detectors have large differences in their angular coverage or geometry, $\beta \approx 1$ [153, 155]. Finally, $P_z(t)$ is the ensemble average muon spin polarization along the $\hat{z}$ direction.

A typical histogram for a single counter is shown in Fig. 3.5. Here, we see that the overall behaviour is exponential, due to the radioactive decay of the muon with its mean lifetime of $\tau_\mu = 2.197\mu$s. Superimposed on this is the oscillation that is generated b y the precession of the muon spin in the local magnetic field of the sample. All of the information about the magnetic

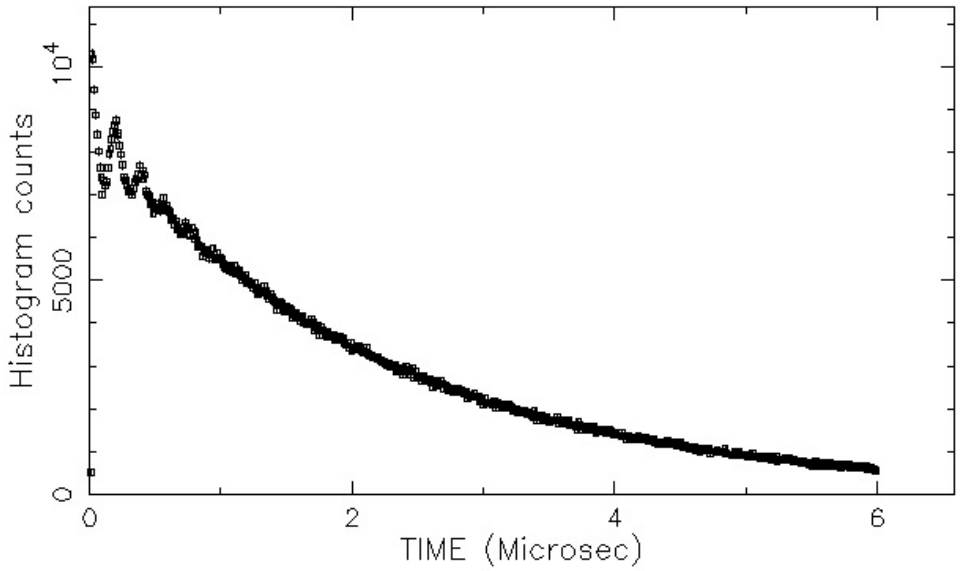

Figure 3.5: An example of a μSR histogram in one counter. This shows the oscillatory behaviour of the rotating muon spin, which decreases over time, superimposed on the exponential from the radioactive decay of the muon. Data taken by the author as part of [155].

environment of the muon is contained in a measurement of this type. However, in order to see the effects more clearly and to remove the effects of the muon lifetime, one often plots the asymmetry of two opposing counters, such as the Back and Forward counters, defined by:

$$A_z(t) = \frac{(N_B(t) - B_B) - \alpha(N_F(t) - B_F)}{(N_B(t) - B_B) + \alpha(N_F(t) - B_F} \tag{3.11}$$

Here, the parameter α is introduced to account for any differences in the counter efficiency, solid angle and other factors. Unlike β, this values is not always close to 1, but it can be easily measured with a μSR experiment in

a para- or non-magnetic phase with a small applied field ($\sim$ 50 G) [153]. A representative asymmetry, with identical data to Fig. 3.5 is shown in Fig. 3.6.

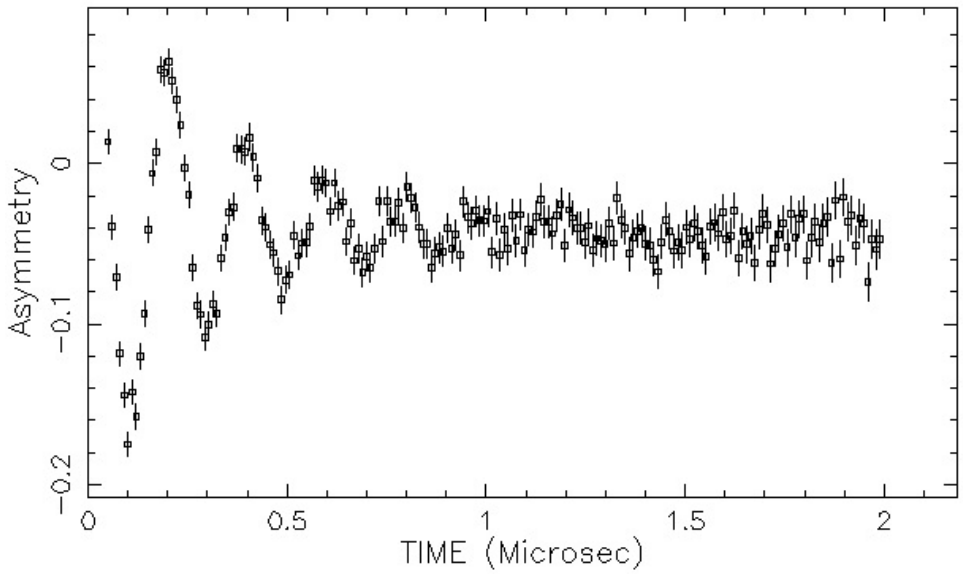

Figure 3.6: An example of a μSR asymmetry using two counters. This shows the oscillatory behaviour of the rotating muon spin more clearly, including its decreases over time. The exponential arising from the radioactive decay of the muon has been cancelled out with this method. Data taken by the author as part of [155].

The asymmetry is proportional to $P_z(t)$ through $N_{B,F}(t)$, so we want to analyze the behaviour of $P_z(t)$, since it contains the information about the magnetism within the sample. In the case of static magnetic moments, $P_z(t)$ can be obtained by weighting Eq. 3.9 with the components of the magnetic field at the muon site:

$$P_z(t) = \iiint S_z(t)\mathrm{P}(H_x)\mathrm{P}(H_y)\mathrm{P}(H_z)dH_x dH_y dH_z \tag{3.12}$$

where $\mathrm{P}(H_n)$ is the probability of the muon seeing a field H_n in the $\hat{n}$-direction.

In the case of long-range, static magnetic order, the field distribution is given by one or more delta functions, reducing Eq. 3.12 to a cosine plus a constant. This represents the coherent precession of the muon ensemble about the perpendicular component of the local magnetic field. In reality, the magnetic order is not completely uniform and so a distribution of local fields is present. For example, each delta function may be more like a Gaussian distribution of fields. This causes a dephasing of the muon spin ensemble, and the rate at which this occurs is known as the muon "relaxation rate". This is an important quantity that carries information about processes that tend to dephase the muon spins, such as field inhomogeneity, interaction with the magnetic moments (spin flips), muon hopping and others [152, 153]. As an example, for the case of a single Gaussian distribution of fields about $H = 0$, we have:

$$\mathrm{P}(H_i) = \frac{\gamma_\mu}{\sqrt{2\pi}\Delta} \cdot \exp(-\gamma_\mu^2 H_i^2 / 2\Delta^2) \tag{3.13}$$

where $i = x, y, z$. Applying this to Eq. 3.12 gives the polarization function [156]:

$$P_z(t) = \frac{1}{3} + \frac{2}{3}(1 - \Delta^2 t^2) \exp(-\frac{1}{2}\Delta^2 t^2) \tag{3.14}$$

This equation is known as the Gaussian Kubo-Toyabe and corresponds to a system of randomly oriented spins such as a spin glass [157]. The constant term corresponds to the fraction of random local fields that point along the direction

of the initial muon spin polarization. We also see that the information about the width of the local field distribution (Δ, the Gaussian width) is contained in the relaxation rate of the polarization function.

The local field distribution is what carries the information about the magnetism in the system being studied and finding the functional form of $P_z(t)$ is one of the main objectives of a μSR experiment. Various function forms for $P_z(t)$ arise for different kinds of magnetism in a sample, depending on the size, distribution and dynamics of the magnetic moments. These forms are used to fit the μSR measurements, and the quantities extracted from such fits describe the character of the magnetism in the material. Where the μSR data is presented in Chapter 4, these functional forms will be discussed in more detail.

3.2.3 Transverse Field (TF)-μSR

Transverse Field (TF)-μSR experiments involve applying a magnetic field perpendicular (transverse) to the direction of the initial muon spin polarization. This can be done by either applying the field perpendicular to the beam direction (parallel to the muon momentum), or applying the field along the beam direction and rotating the muon spin by $90B.Sc.\ (Hons.),\ M.Sc.$ [158]. For small fields, either method produces the same results, however large fields tend to produce significant deflection in the beam when directed perpendicular to the muon momentum. Consequently, the latter is the more common method when fields exceed $\sim$100 G. A schematic of this experimental geometry is shown in Fig. 3.7.

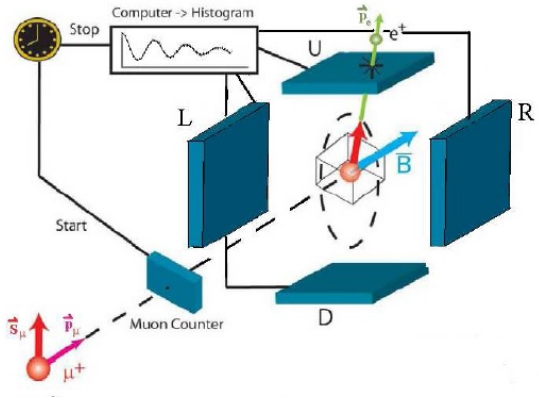

Figure 3.7: The experimental geometry of a TF-μSR experiment. This shows the latter of the two arrangements, where the muon spin has been rotated to be perpendicular to the beam direction (the muon momentum). The magnetic field is then applied along the direction of the muon momentum. Figure taken from [154].

It can be seen from Fig. 3.7 that the muon spin will precess through four counters arranged in two opposing pairs (Up/Down and Left/Right). Thus, two asymmetry functions can be defined through Eq. 3.11, one for each pair. They can be fit simultaneously to obtain information about the local magnetic field at the muon site. Since the precession frequencies are often quite large, it becomes more useful to combine these two asymmetry function in a "rotating reference frame" analysis. This is a method by which the asymmetry function is generated in a reference frame that effectively rotates the positron counters with respect to the laboratory frame at a rate that is very close to the muon precession frequency. Fitting the data in this manner proves much more effective. For a more detailed discussion, see Ref. [159].

Muons in a large transverse field will precess at a frequency given by Eq. 3.6. The applied fields are, in general, much larger than the local field due to the magnetism within the sample, so all of the muons tend to see nearly the same field, and very nearly perpendicular to their spin direction. This greatly simplifies the task of analyzing the μSR data, since the $\hat{x}$-component of Eq. 3.12 reduces to:

$$P_x(t) = \int \mathrm{P}(H_z)\cos(\gamma_\mu H_z t)dH_z \tag{3.15}$$

This is a Fourier transform, so it can readily be seen that the TF-μSR asymmetry in the $\hat{x}$-direction is proportional to the cosine Fourier transform of the distribution of local magnetic fields in the $\hat{z}$-direction, assuming a static magnetic system. This is also somewhat apparent from Eq 3.6, where the muon precession frequency is directly proportional to the local field. So the muon ensemble probes the distribution of local fields within the sample environment.

For example, a Gaussian distribution of local fields would have a probability distribution:

$$\mathrm{P}(H_z) = \frac{\gamma_\mu}{\sqrt{2\pi}\Delta} \cdot \exp(-\gamma_\mu^2(H_z - H_{app})^2/2\Delta^2) \tag{3.16}$$

where H_{app} is the applied magnetic field. This gives a precessing muon polarization that is convoluted with a Gaussian form of relaxation:

$$P_x(t) = \cos(\gamma_\mu H_{app} t) \cdot \exp(-\frac{1}{2}\Delta^2 t^2) \tag{3.17}$$

As in the case of ZF-μSR, there will be some relaxation in the signal due to disorder, fluctuations, etc. This contains similar information to the ZF case, but differs due to the presence of the magnetic field. In this thesis, the primary use of TF-μSR was to measure properties of the mixed (vortex) state of type-II superconductors, which is discussed in the following section.

3.2.4 μSR in the Vortex State of Type-II Superconductors

As discussed in Section 1.1 and shown in Fig. 1.2, a type-II superconductor will exist in the Meissner state for $H_{app}<H_{c1}$, while for $H_{c1}<H_{app}<H_{c2}$, the material exists in the mixed, or vortex, state. Both of these states are described by the superconducting properties discussed in Sec. 1.1, but the vortex state contains an ordered arrangement of normal and superconducting regions. This can allow the extraction of information about the superconducting state which may lead to a more detailed understanding of the microscopic pairing mechanism in unconventional superconductors.

In particular, measurements of the magnetic penetration depth, λ, are one way of probing low-energy electronics, since λ^{-2} is proportional to the superfluid density (the density of superconducting carriers), n_s [10]. In the vortex state, as in the Meissner state, magnetic fields are not perfectly screened, so the field decays outside of the vortex core over the length scale λ. Within the vortex core, the superfluid density, n_s, the superconducting order parameter, $\psi(r)$, and the supercurrent density, $J_s(r)$ are strongly suppressed, as shown in Fig. 3.8 [160].

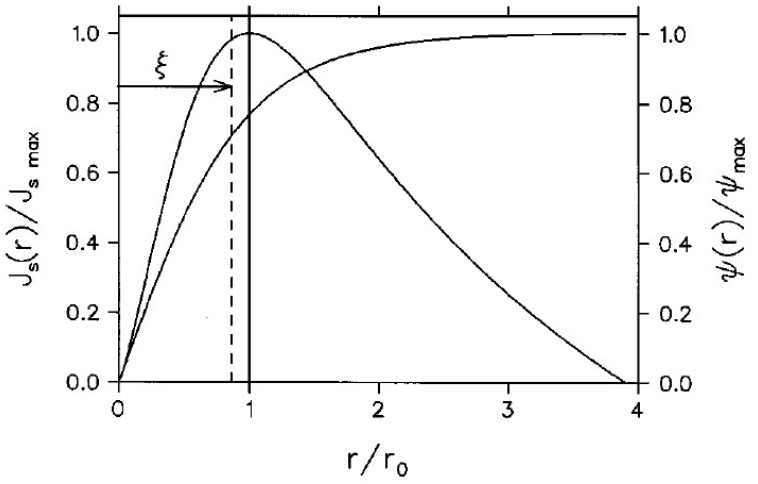

Figure 3.8: The spatial variation of the superconducting parameters $J_s(r)$ and $\psi(r)$ around a conventional vortex core. The parameters are shown normalized to their maximum values, which occurs at $r = r_0$ for the supercurrent density and $r = \infty$ (far from the vortex core) for the superconducting order parameter. Figure taken from [160] and used with permission.

The order parameter is zero at the center of a vortex and rises sharply to a maximum outside the vortex core on a length scale called the coherence length, ξ. This is thus closely related to the size of the vortex cores, while the decay of the magnetic field arising from the vortex core is determined by λ. Both of these parameters can be determined by studying the magnetic field distribution within the vortex state. Thus, μSR is is a technique that is well-suited to this type of measurement. Using μSR, both of the characteristic length scales λ and ξ can be determined by analysing the field distribution arising from a regular Abrikosov vortex lattice [160, 4].

As described in Section 3.2.1, muons stop at interstitial sites within the crystal lattice. The precise location of the muon site is often hard to deter-

mine. However, since the spacing between adjacent vortex is generally large for a μSR experiment (usually performed with $H_{app} \leq 8$ T) compared to the crystallographic unit cell and is usually incommensurate, the muons stop at random locations with respect to the vortex lattice. In this way, the muon ensemble randomly samples the entire field distribution within the sample, regardless of the actual muon stopping site.

If we assume that the field is applied in the $\hat{z}$-direction, then the vortices will also be oriented in that direction, as is the net field everywhere. So we can write the time evolution of the total muon polarization, $P_x(t)$, as [160]:

$$P_x(t) = \frac{1}{N} \sum_{i=1}^{N} \cos[\gamma_\mu B(\vec{r}_i)t + \omega] \tag{3.18}$$

where the sum is over all muon sites and $B(\vec{r}_i)$ is the magnitude of the local field at site i. Since we can assume that the muons randomly sample the entire vortex lattice, we can extend the sum into an integral:

$$P_x(t) = \int_0^\infty \bar{n}(B) \cos(\gamma_\mu B t + \omega) dB \tag{3.19}$$

where $\bar{n}(B)$ is the ideal probability field distribution. In other words, $\bar{n}(B)dB$ is the probability that a muon sees a field between B and $B+dB$, and so precesses with a frequency $\nu = \gamma_\mu B$. Here we see that the mean precession frequency and the relaxation rate (rate of dephasing) is determined by the field distribution $\bar{n}(B)$. An example of this probability distribution is shown in Fig. 3.9, for a hexagonal vortex lattice, known as an Abrikosov lineshape. Here, we see that there is a peak frequency, determined by the most probable

field, which is the saddle point between two adjacent vortices. There are also a low-field and a high-field cutoff. The lowest possible field is at the center of a three-vortex arrangement, while the highest field is at the vortex core. Relating this to the superconducting properties, the high-field cutoff is mostly determined by ξ, while the overall width is related primarily to λ.

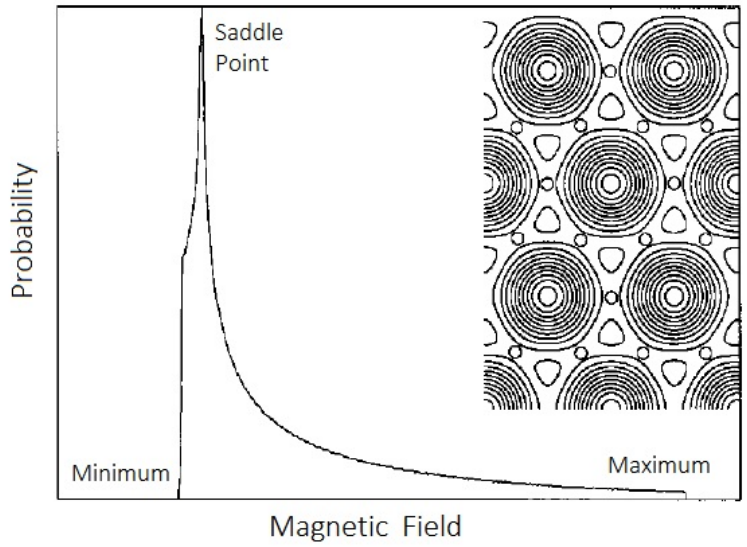

Figure 3.9: The theoretical field distribution for a hexagonal vortex lattice. The maximum, minimum and most probable (saddle point) fields are shown. The inset shows a contour plot of such an arrangement of vortices. Figure adapted from [160].

In a real material, there are deviations from an ideal vortex lattice, that will change the field distribution, and will introduce a depolarization function, $G(t)$ [160], which accounts for the effect of weak disorder:

$$P_x(t) = \int_0^\infty n(B)\cos(\gamma_\mu B t + \omega)dB \tag{3.20}$$

All of the information on the field distribution within a sample is contained in $n(B) = G(t) \cdot \bar{n}(B)$. As stated above, an ideal vortex lattice will have a characteristic field distribution that is given by an Abrikosov model. Factors such as vortex pinning, lattice disorder, sample geometry and others will also contribute to $n(B)$. To a good approximation, these deviations can be accounted for with a Gaussian depolarization function, $G(t)$ [161]. In general, vortex pinning is the largest contribution to the imperfections in the field distribution of the vortex lattice [160, 162]. An example of this field distribution in a sample of $YBa_2Cu_3O_{6.95}$ is shown in Fig. 3.10. All of these contributions will, in general, provide a Gaussian broadening to the field distribution.

To more readily identify the magnetic field distribution seen my the muon ensemble, a fast Fourier transform (FFT) is often performed. Since the time-frequency relationship is related by the local magnetic field (see Eq. 3.6), a FFT of the complex muon polarization, $\tilde{P}(t)$, yields a good approximation of the internal field distribution. Now, fitting the muon frequency spectrum is equivalent to fitting the magnetic field distribution, which can be done to a form determined by the geometry of the vortex lattice (square, hexagonal, etc), and the microscopic superconducting properties such as λ and ξ. In this way, μSR can provide simultaneous absolute values for these parameters.

This was done for some of the samples discussed in Chapter 4. For this analysis, the data was fit in the time domain, with a theoretical field distribution, $\bar{n}(B)$, given by the Abrikosov form. This lineshape was convoluted with a Gaussian to account for lattice disorder, as described above. More details of the fitting will be discussed in that chapter.

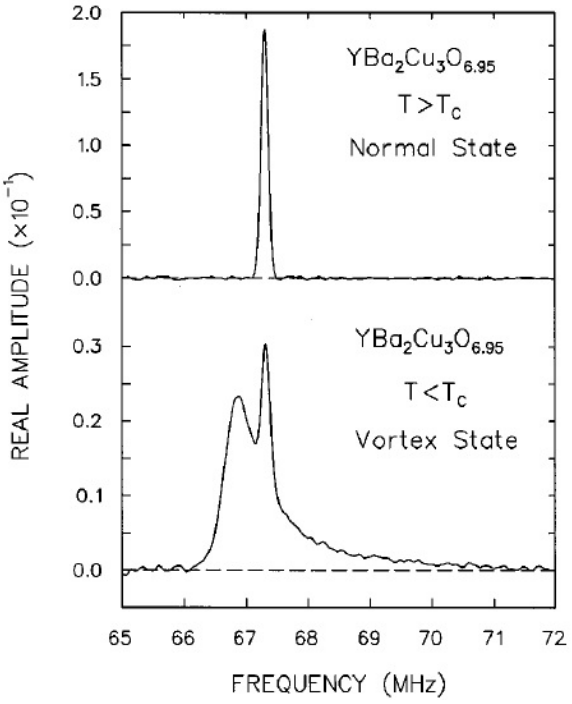

Figure 3.10: The field distribution measured in the normal (top) and mixed (bottom) states of $YBa_2Cu_3O_{6.95}$, which has a hexagonal vortex lattice. In the normal state, the field distribution is a narrow Gaussian about the applied field. Below T_{SC}, the Abrikosov lineshape appears. Superimposed on this is a Gaussian with the same frequency and smaller amplitude than the normal state. This is due to a volume fraction or background that is not superconducting. Figure taken from [160] and used with permission.

3.3 Neutron Diffraction

3.3.1 Introduction to Neutron Scattering Properties

Neutron scattering has proven itself as one of the primary methods for the study of long-range order, both in terms of crystallographic structure and magnetic structure. Like μSR, it uses particles from outside the system (in

this case, neutrons) to probe the properties of the material. Neutrons are particles normally found in the nucleus of atoms, and are weakly interacting with matter. Samples can often be several centimeters thick, and typically only 1 in 1000 neutrons will interact with the sample. They are uncharged, and so do not interact through the Coulomb interaction. The main interaction with the material comes through the strong force with the nuclei. This force is extremely short-ranged, requiring the neutrons to be on the order of femtometers from the nucleus. A reasonably accurate model of the interaction is a delta function at the nucleus.

When a neutron does interact with the sample, it is usually a scattering event, where the momentum and/or the energy of neutron is changed. Multiple scattering events for the same neutron is not generally a concern, except in special cases [163]. Neutrons also behave as waves, so scattering of neutrons is analogous to scattering of electromagnetic waves. We can assume the atoms in a crystal to be arranged in periodic planes, separated by a distance d. When a plane wave, such as those from a neutron wavefunction, is incident on these planes, the waves will scatter at an angle θ. Scattered waves will interfere with one another, and will generally cancel each other out, since different planes will produce all possible phase differences. However, at specific angles, the path length between waves incident on successive planes will be an integer multiple of the wavelength. This will produce no phase difference between the outgoing waves, and will produce constructive interference. This principle is known as Bragg's law [164], and can be described by the equation [5]:

$$n\lambda = 2d\sin(\theta) \tag{3.21}$$

where $n \in \mathbb{Z}$ is an integer, λ is the neutron wavelength, assumed to be the same for the incoming and outgoing waves, d is the separation between scattering planes and θ is the angle that the incoming and outgoing waves make with the normal to the scattering plane. *ie.* the angle between the incoming and outgoing waves is 2θ. This is shown in Fig. 3.11.

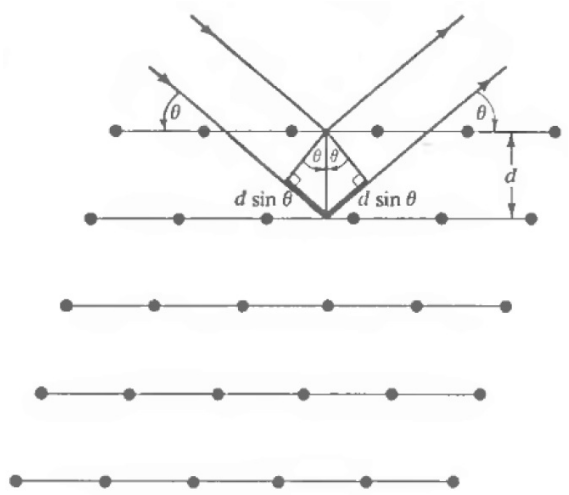

Figure 3.11: An illustration of Bragg's law in a periodic crystal. The path length difference is $2d\sin(\theta)$, which is an integer multiple of the wavelength to obtain constructive interference. Figure taken from [5].

This condition will be satisfied in any direction where planes of scatterers exist within the crystal. This is necessarily related to the crystal structure, and so it is natural to rewrite Bragg's law in terms of reciprocal lattice vectors, $\vec{Q}$, since the scattering exists in reciprocal space. In other words, Bragg's law

is satisfied for any reciprocal lattice vector that is the difference between the outgoing and incoming wavevectors that also satisfy Bragg's law:

$$|\vec{Q}| = \frac{4\pi \sin(\theta)}{\lambda} \tag{3.22}$$

where $\vec{Q} = \vec{k}_f - \vec{k}_i$ is the difference between the outgoing, $\vec{k}_f$ and incoming, $\vec{k}_i$ wavevectors. This can also be extended to inelastic scattering – where the incoming and outgoing wavevectors correspond to waves of differing energies. This is a case where the neutron has given energy to the lattice in the form of an excitation of the system. A phonon (lattice vibration) is an example of an excitation that can be detected by its inelastic neutron scattering spectrum.

Neutrons also have magnetic dipole moments, $\vec{\mu}_n = \gamma_n \mu_N \vec{\sigma}_N$, where γ_n is the neutron gyromagnetic ratio, μ_N is the nuclear magneton and $\vec{\sigma}_N$ is the spin-$\frac{1}{2}$ Pauli spin operator. For this reason, neutrons interact with magnetic moments, and so can be scattered by these moments in a material. The scattering is analogous to Bragg scattering, and the Eq. 3.21 and 3.22 are equally valid for magnetic structures. Since the strength of magnetic scattering and nuclear scattering is often quite comparable [163, 165], neutron scattering is a useful probe of long-range magnetic structure in condensed matter systems.

Fermi's Golden Rule provides an accurate description of the scattering cross section of the interaction between the neutron and the system being measured. This is an expression based on first-order perturbation theory, and given by:

$$\frac{d^2\sigma}{d\Omega dE'} = \frac{k'}{k}\left(\frac{m_n}{2\pi\hbar^2}\right)^2 |\langle k'\sigma'\lambda'|V|k\sigma_0\lambda_0\rangle|^2 \cdot \delta(E_{\lambda_0} - E_{\lambda'} + \hbar\omega) \tag{3.23}$$

Here, σ is the cross section, Ω is the solid angle into which the neutrons are scattered and E' is the final energy of the neutron. k and k' are the initial and final wavenumbers of the neutron, V is the interaction potential and $\hbar\omega$ is the energy transfer. The delta function ensures energy conservation in the collision.

The scattering cross-sections contain information about the excitations of the system that are too diverse to cover in detail here. The width, in energy E or momentum $\vec{Q}$, of the scattering feature can be a result of the scattering cross section (rather than experimental resolution). This can be indicative of short-lived excitations (E) or features with a finite spatial correlation length ($\vec{Q}$), as examples.

The following section will serve to provide more detail about the experimental technique of triple-axis neutron scattering that is used in this thesis.

3.3.2 The Triple-Axis Neutron Scattering Technique

The triple-axis neutron scattering technique was pioneered by B. Brockhouse and C. Shull, and was such an important development that it was awarded the 1994 Nobel Prize in Physics. Triple-axis is so named because it uses three Bragg scattering events for a very precise measurement of the

nuclear and magnetic structure of a material. A simplified schematic of the triple-axis technique is shown in Fig. 3.12 [166].

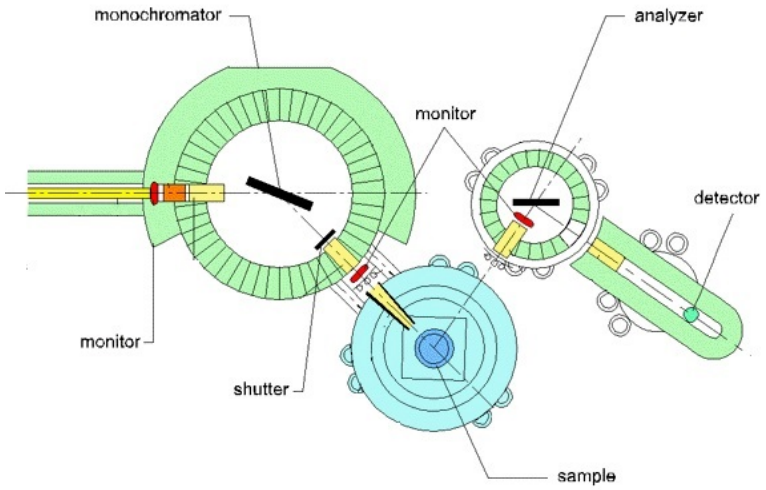

Figure 3.12: A schematic representation of a triple axis experimental setup. Here, a beam of neutrons from a source is incident on the monochromator crystal, selecting an incoming energy. The neutrons are then scattered from the crystal, and the outgoing beam is scattered from the analyzer crystal, picking out one particular outgoing energy. The resultant flux is then measured by a detector. Figure taken from [166].

Many neutron scattering experiments use neutrons that are generated from nuclear fission reactions that are thermalized by a moderator, usually heavy water at room temperature, and so are called "thermal neutrons". These neutrons come over a wide range of energies and thus a range of wavelengths. This would serve to produce a range of angles for the scattered beam, and so is not used for most experiments (though there are experiments that make use of this). In order to obtain a mono-energetic beam of neutrons, the thermal neutron beam is Bragg-scattered from a large single crystal called the monochromator. This is usually done with a material such as Silicon or Graphite, which

produce a relatively clean (in terms of energy) beam of neutrons. Primarily, a single energy of neutrons will be diffracted from the monochromator, called the initial energy, E_i. By rotating the monochromator crystal, a different E_i can be chosen [165].

This beam of neutrons is then incident on the sample, where it is Bragg-scattered again. By looking at different scattering angles and different orientations of the sample, all possible scattering vectors $\vec{Q} = \vec{k}_f - \vec{k}_i$ can be studied. This is often done with a diffractometer, a device that allows for movement in any combination of the four possible rotation axes: the three crystallographic rotation axes (α, β and γ) and the scattering angle (θ). A schematic of such a four-circle diffractometer is shown in Fig. 3.13.

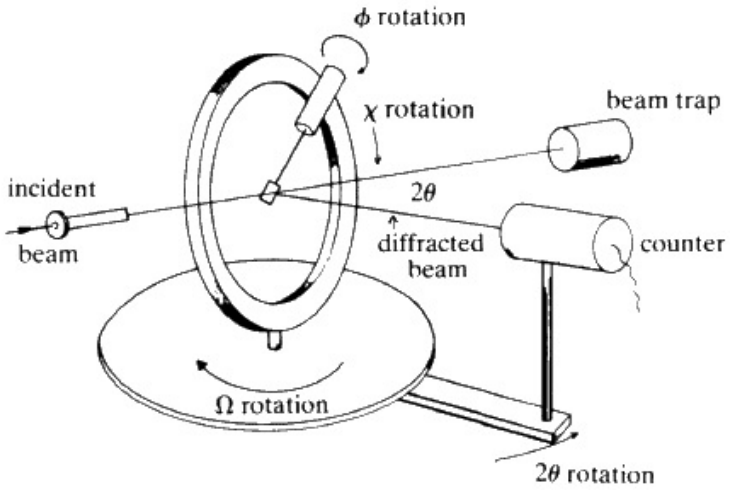

Figure 3.13: A schematic representation of a four-circle diffractometer. This is used to rotate the crystal through α, β and γ, and to change the scattering angle, θ, to achieve any desired scattering vector $\vec{Q}$. Figure taken from [167].

Following this, the outgoing neutron beam is incident on the analyzer crystal. This behaves exactly the same as the monochromator by selecting a par-

ticular energy. This defines the final energy for the neutrons, E_f. For elastic scattering, $E_i = E_f$, but in the case of measuring inelastic features (phonons, magnons, *etc.*), $E_i > E_f$, indicating that the neutron gave energy to the crystal in the form of excitations. By rotating the analyzer crystal, various E_f will be measured. Lastly, the neutrons hit a detector, usually composed of ^{3}He, allowing them to be counted.

We have seen how to measure a specific $\vec{Q}$ by changing the angle settings of the diffractometer or spectrometer. To measure any $E = E_i - E_f$, we can change the angle of the monochromator or the analyzer. The former is "fixed E_f" mode and the latter is "fixed E_i" mode. For the neutron scattering measurements in this thesis, both methods were used; the measurements in Section 5.2 used a fixed E_f, while the measurements in Section 5.3 used a fixed E_i. The two instruments that were used will now be addressed in more detail.

3.3.3 The C5 DUALSPEC Spectrometer

For the measurements in Section 5.2, experiments were performed on the C5 DUALSPEC Spectrometer at the Canadian Neutron Beam Center, at Chalk River National Laboratories in Chalk River, Ontario, Canada [167]. A picture of the C5 spectrometer is shown in Fig. 3.14.

This instrument allows scattering at angles up to 115°, in steps of 0.001°. It can be fitted with a variety of collimators, filters and different kinds of monochromator/analyzer crystals. The specific experimental details will be discussed in Section 5.2.

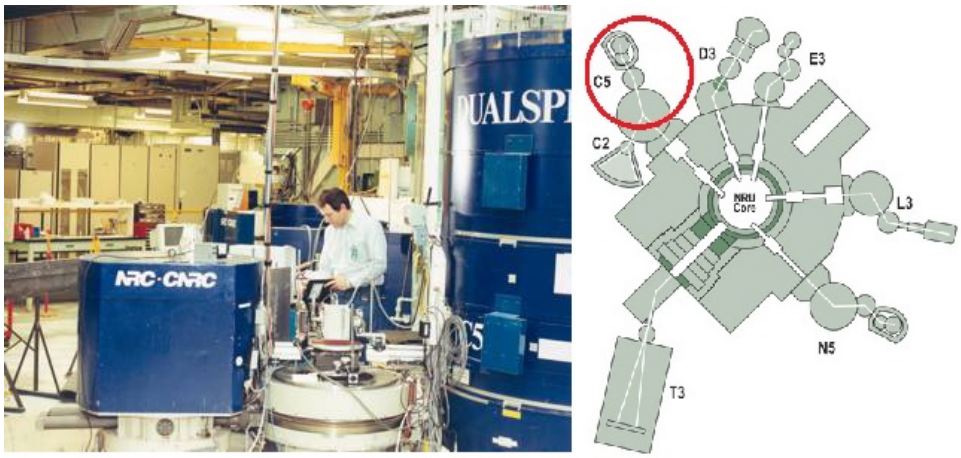

Figure 3.14: (Left) An image of the C5 Spectrometer, showing the sample in between the analyzer & detector and the monochromator and source. (Right) The layout of the beamline floor at Chalk River Laboratories, indicating the location of C5, and showing the three axes for the instrument. Figure taken from [167].

3.3.4 The Multi-Axis Crystal Spectrometer

For the measurements in Section 5.3, experiments were performed on the Multi-Axis Crystal Spectrometer (MACS) at the National Institute for Standards and Technology (NIST) National Centre for Neutron Research (NCNR) in Gaithersburg, Maryland, USA [168]. A schematic of the MACS instrument is shown in Fig. 3.15.

The operation of MACS is based on the same principles as a conventional triple axis instrument. It uses a reactor-based neutron source, however, the neutrons are moderated to emerge with a lower energy than conventional thermal neutrons. These "cold" neutrons allow for lower energy neutrons to be incident on the sample so that better energy resolution can be achieved. The MACS instrument allows for energy resolution down to 0.2 meV.

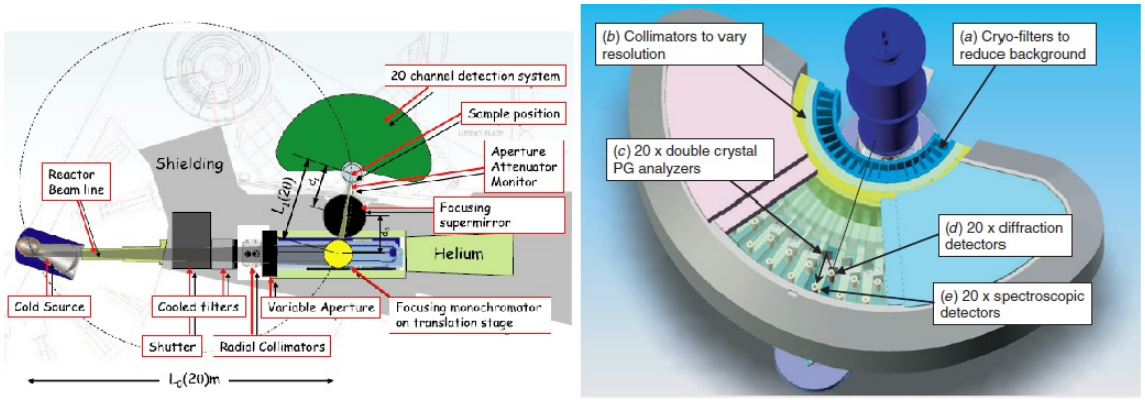

Figure 3.15: (Left) An overhead schematic of MACS, showing its various components. (Right) A closer view of the sample station and the 20 detector channels. Figure taken from [168] and used with permission.

A single crystal analyzer is used and the neutrons scatter from the sample as previously described. However, the third leg of the diffractometer is set up with multiple channels, essentially allowing for multiple scattering angles from the sample. These 20 detector channels are quite closely spaced ($\sim 8°$) and each has its own analyzer crystal. This allows comprehensive coverage of the scattered neutrons, generating much more data more quickly.

More details about the particular configuration of the instrument will be given in Section 5.3.

3.3.5 Instrumental Resolution Function

The discussion of neutron scattering in Sections 3.3.1 and 3.3.2 has focused on a technique in an abstract way, and in this sense all of the measured peaks should appear as points in $(\vec{Q}, E)$-space. However, the details of the instru-

mentation in Sections 3.3.3 and 3.3.4 clearly indicate a minimum accuracy in measuring such points, giving them width in both $\vec{Q}$ and E. This is due to the limited resolution of each instrument, and depends on quantities such as the degree of focusing, the width of the detectors and the mosaic of the crystals. In attempting to extract quantitative values from a measured spectrum, the influence of the instrumental resolution must be considered.

To do this, one defines the instrumental resolution function, which is the probability of detecting a neutron of energy $E = \hbar\omega$ and momentum $\vec{Q}$ when the instrument is configured to measure a scattering process at $(\vec{Q}, E)$ [169]. To a first approximation, the mosaic spread of the monochromator and analyzer and the transmission function of the slit systems are Gaussian distributions. This allows the resolution function to be defined everywhere in $(\vec{Q}, E)$-space for any value of the instrumental parameters.

While this can be done in a functional form, it is more efficient to compute it numerically. This is done by constructing the Cooper-Nathans matrix [169, 170], a combination of the instrumental parameters (divergences) from the slits, monochromator and analyzer. With the definition of other such matrices to include the differences with respect to scattering angles and energy transfer, the resolution matrix can be constructed. A more complete mathematical treatment of this method is given in Ref. [171].

This resolution matrix can then be convoluted with the 4D dataset to obtain data that has been corrected for this resolution, allowing for more accurate calculations of physical parameters. This was included for both neutron

scattering experiments described in Chapter 5, using the numerical program RESLIB [171].

Chapter 4

μSR Measurements of $Ba(Fe,Co)_2As_2$

This Chapter details a series of μSR measurements performed on single crystals of the pnictide superconductors $Ba(Fe_{2-x}Co_x)_2As_2$ as well as a single crystal of $Sr(Fe_{0.87}Co_{0.13})_2As_2$. This work has been previously published, in part. The work in Sec. 4.2 is contained in a manuscript that will be submitted for publication shortly [172]. The work of Sec. 4.3 was published in [173], while the work of Sec. 4.4 and 4.5 has been published in [174].

4.1 Introduction

Several single crystals of the series $Ba(Fe_{2-x}Co_x)_2As_2$ were measured with Cobalt concentrations $x = 0.038$, 0.047, 0.061, 0.074, 0.107 and 0.114, as well as a single crystal of $Sr(Fe_{0.87}Co_{0.13})_2As_2$ using μSR. As described in Chapter 1, these samples are grown from self-flux and produce relatively large, homogeneous single crystals of approximately 1 cm^2 surface area. These materials have been shown to have very clean transitions, in particular the superconducting transition as shown in Fig. 4.1 for $x = 0.074$.

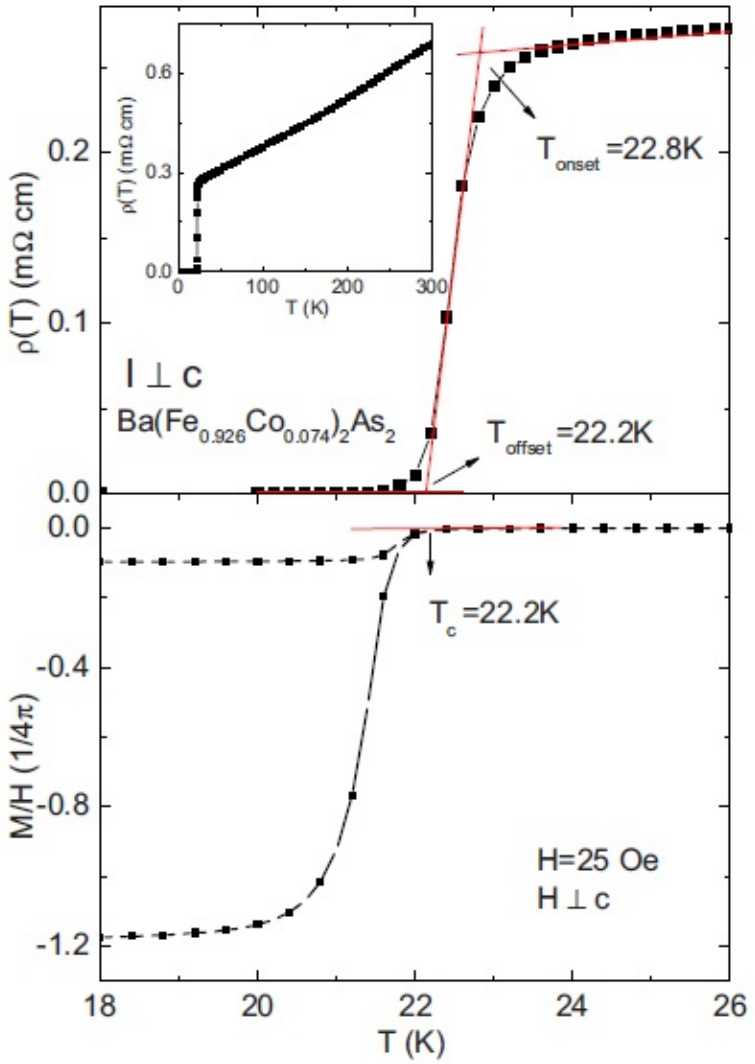

Figure 4.1: (Top) Resistivity of $Ba(Fe_{0.926}Co_{0.074})_2As_2$ in the vicinity of T_{SC} and (inset) from 2 to 300 K. (Bottom) Field-cooled and zero-field-cooled magnetization in the vicinity of T_{SC}. Figure taken from [173].

The samples were taken to TRIUMF, where the μSR measurements were performed. All of the measurements in Sections 4.3, 4.4 and 4.5 were performed on the M20 surface muon beamline, while the measurements of Section 4.2 were performed on both the M20 and M15 surface muon beamlines. In all cases,

the measurements were performed in a Helium gas flow cryostat using a low background sample holder, such that only muons landing in the sample were measured in the μSR spectra.

4.2 Coexistence of Magnetism and Superconductivity in Underdoped $Ba(Fe,Co)_2As_2$

The two samples with lowest Co-doping, $x = 0.038$ and $x = 0.047$, are in the portion of the phase diagram that contains both static magnetic order and superconductivity. To measure the properties of the magnetically ordered region, Zero-field (ZF)-μSR spectra were collected on both samples over a range of temperatures and were compared to the parent ($x = 0$) material. Representative spectra for these three dopings measured at T = 1.65 K are shown in Fig. 4.2.

In the parent material, there is a clear precession signal indicative of long-range magnetic order. In the doped samples, this signal is highly-damped, suggesting a broad distribution of internal fields at the muon site(s). This would result from a substantial degree of disorder in the magnetic ordering in the doped materials. The solid lines in Fig. 4.2 are fits to a model based on two precessing muon sites and a non-precessing background signal:

$$A(t) = A_1 \cos(\omega_1 t) * e^{-\lambda_1 t} + A_2 \cos(\omega_2 t) * e^{-\lambda_2 t} + A_e e^{-\lambda_e t} \qquad (4.1)$$

This fitting function seems reasonable given previous studies of the underdoped and parent compound in which two muon sites have been observed [175,

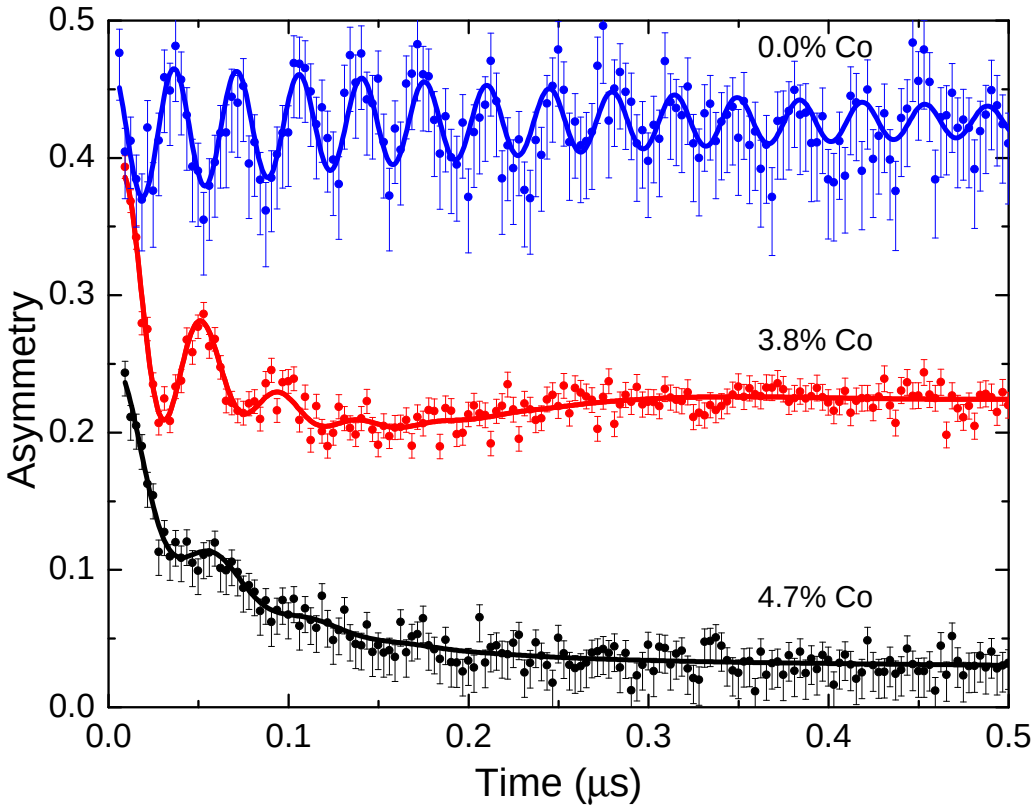

Figure 4.2: The zero-field (ZF)-μSR spectra taken at T = 1.65 K for the parent $x = 0$ (blue), $x = 0.038$ (red) and $x = 0.047$ (black). The $x = 0.038$ data is vertically offset by +0.15 and the $x = 0$ data is vertically offset by +0.3 for clarity. The solid lines are fits to the data, as described in the text. Here, clear precession is seen in the parent material, but the precession in the doped compounds are strongly damped, indicating significantly disordered magnetism. Figure taken from [172].

176], as well as DFT calculations supporting two local electrostatic minima in the crystal structure [177]. Furthermore, a single damped exponential did not fit the data well. The frequencies extracted from the fits were found to scale with one another, consistent with the signals being from two muon sites with different local fields. This characteristic was found in the initial analysis, and

so the frequencies and asymmetries of the two signals were fixed to be a constant ratio of one another. These ratios were included as fitted parameters, but were fixed to be temperature-independent using the whole temperature range below T_{SDW}. The ratio for the parent was found to be 0.24(1), while for the 3.8% sample, the ratio was 0.20(4), decreased slightly from the parent compound. This continues with the 4.7% sample, where the ratio has decreased to $2.3(4) \times 10^{-3}$. The decrease in the ratio may reflect an increase in the impurities that distort the magnetically-ordered lattice. In the 4.7% doped sample, the small ratio value may be a result of the nearly complete loss of long-range magnetic order. With a large degree of disorder, all of the muon sites appear to have different local fields, removing most of the distinction between the high- and low-field sites.

The frequencies that are observed decrease with increasing doping, as shown in Fig. 4.3. This could be due to the replacement of Fe moments with Co, reducing the size of the internal field. Neutron scattering has observed a reduction in the ordered Fe moment in the isostructural $Ca(Fe_{1-x}Co_x)_2As_2$ [178] and an incommensurate magnetic structure for dopings above $x \approx 0.05$ [60].

These samples were also measured in a transverse field (TF) of 4 mT to measure the paramagnetic volume fraction. In a weakly magnetic or paramagnetic region of the sample, the muons see a local field equal to the applied field, and so can be fit to a simple exponentially-damped cosine:

$$A(t) = A\cos(\omega t) * e^{-\lambda t} \tag{4.2}$$

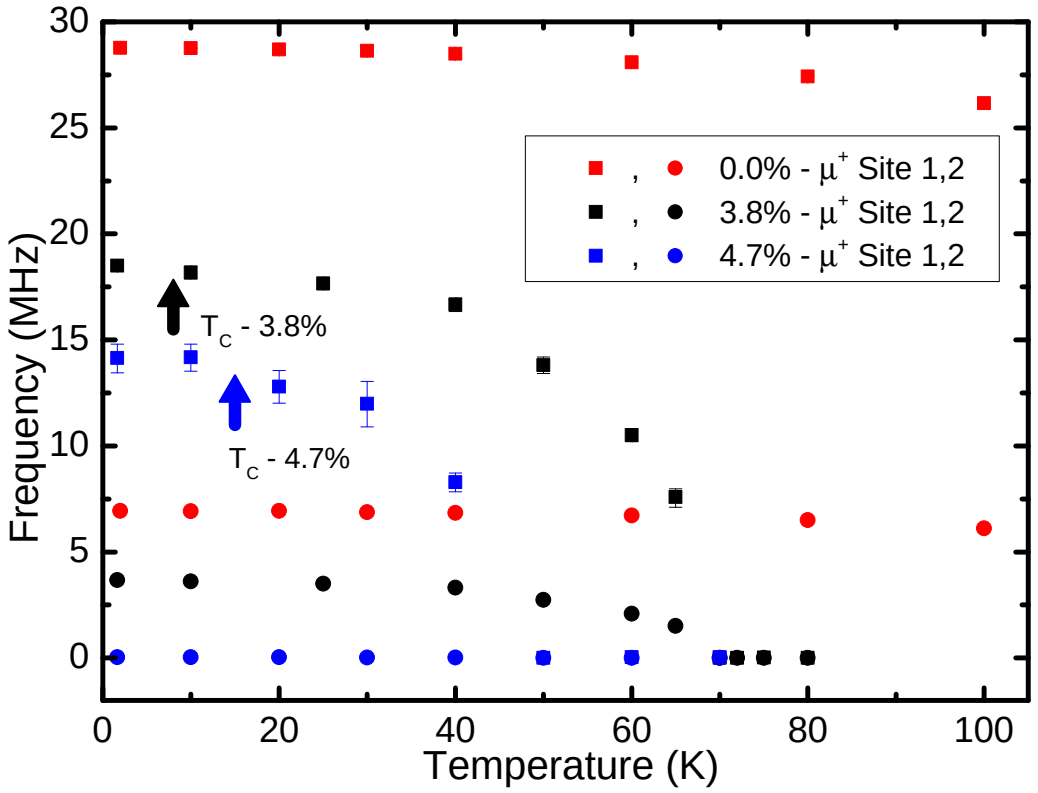

Figure 4.3: (a) ZF-μSR spectra for $Ba(Fe_{1-x}Co_x)_2As_2$ for $x = 0.038$ ($T_{SDW} = 71$ K and $T_{SC} = 8$ K) and $x = 0.047$ ($T_{SDW} = 45$ K and $T_{SC} = 15$ K). There is a clear onset at T_{SDW}, where the precession frequency becomes non-zero. There is no change below T_{SC}. Figure taken from [172].

where $\omega = \gamma_\mu H_{app}$.

Below a magnetic ordering transition, the local field becomes a vector sum of the applied and ordered field (generally, much larger than the applied field). For this reason, the muons no longer precess at the same value of ω above, and so the amplitude of the precessing signal, A, decreases. However, any muons still landing in a para- or weakly magnetic region will still precess at this

frequency. This allows TF-μSR to be used to measure the volume fractions of region of static magnetic moments.

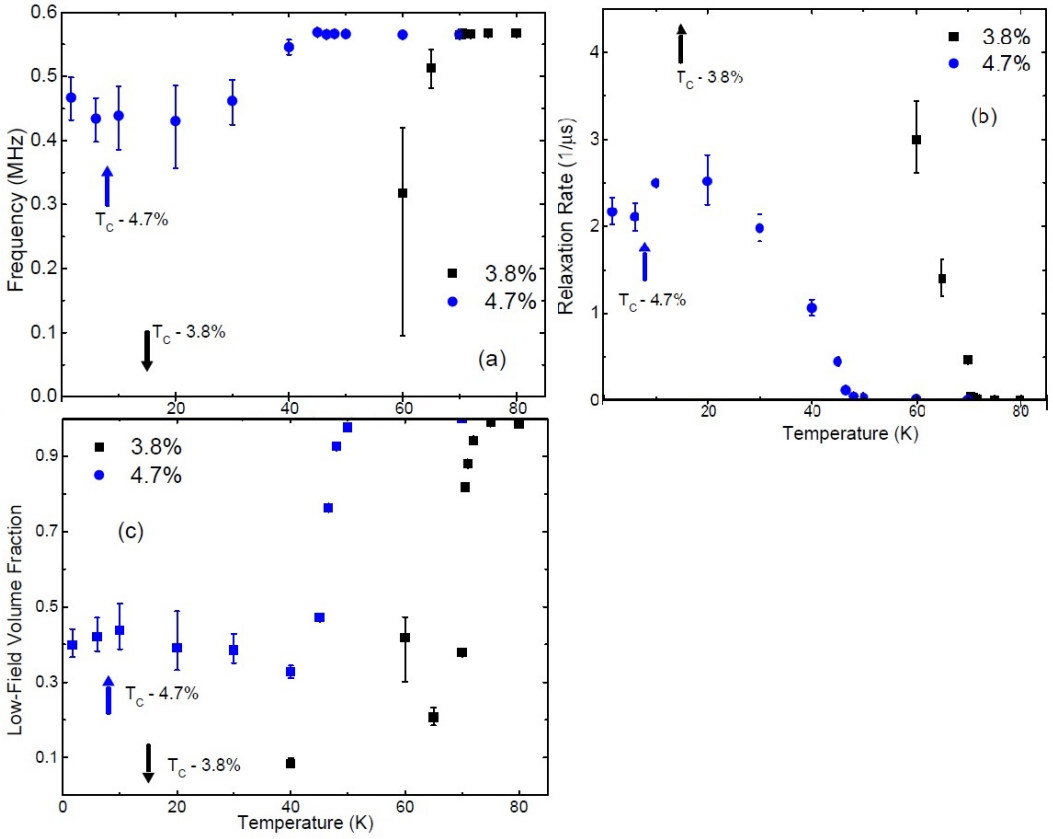

Figure 4.4: TF-μSR measurements of $x = 0.038$ and 0.047 in TF = 4 mT. (a) The frequency shows a drop below the magnetic ordering temperature, but slowly increases again towards T = 0. This may be indicative of field-induced ordering. (b) The relaxation rate increases sharply below T_{SDW}, saturating well before T = 0. This indicates that the local field is fairly inhomogeneous in these samples, which causes dephasing of the muon polarization in the ordered part of the phase diagram. (c) We see a 100% paramagnetic signal above T_{SDW}, which drops sharply at the transition. Below the ordering temperature, there is a residual signal from the low-field region, about 40% for $x = 0.047$ and less than 10% for $x = 0.038$. Due to the small residually-precessing volume present in the 3.8% doped sample, the points below 50 K are omitted from (a) and (b). Figure taken from [172].

Fig. 4.4 shows the results of fitting the temperature-dependent TF-μSR signals to Eq. 4.2. The paramagnetic volume fraction (shown in Fig. 4.4(c)) is normalized to its value above T_{SDW}, and a sharp drop is observed below the transition. The signal saturates quickly, levelling off within 15 K of the ordering temperature. In the 4.7% sample, there is a residual signal that still precesses down to the lowest temperatures measured, but the relaxation rate is still increasing below T_{SDW} indicating that it is only weakly magnetic. This low-field region is less than 10% in the $x = 0.038$ sample, while it is approximately 40% for $x = 0.047$ (see Fig. 4.4(c)).

It is also worth noting that the TF-μSR spectra do not relax to zero asymmetry in the ordered region when the spectra are measured in the direction of the initial muon spin polarization, shown in Fig. 4.5. While the precessing fraction relaxes completely, there is a fraction of the signal which does not precess and does not relax. This indicates that the local field is largely along this direction, corresponding to the $\hat{c}$-axis crystallographic direction. This is confirmed by measuring the TF-μSR spectra in a perpendicular direction, and noting that the spectra do relax to zero in this case (also shown in Fig. 4.5). This is consistent with other techniques that find that the internal field tends to lie in the $\hat{c}$-axis for various dopings [176]. These measurements found fields in excess of 0.15 T, consistent with the local field at the high-field muon site in our measurements, which precessed at a frequency corresponding to an internal field of 0.13 T. Additionally, that the precessing signal in the TF-μSR spectra completely relax within the first 0.5 μs indicates that they still see a local field from the sample. This means that the regions of low-field magnetism

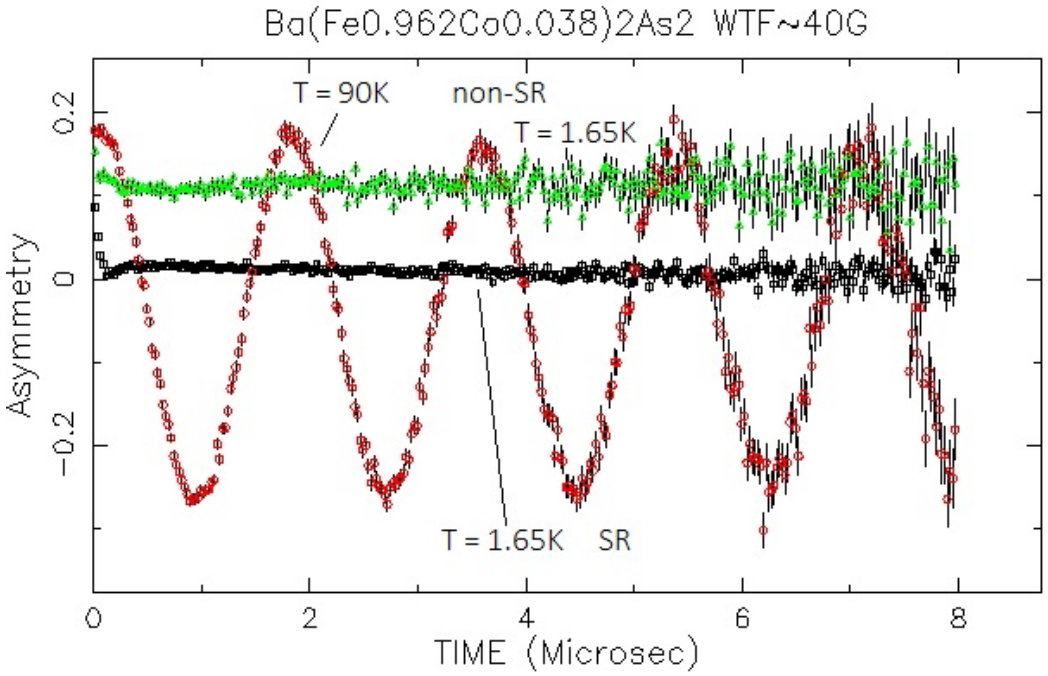

Figure 4.5: Representative TF-μSR spectra measured in $Ba(Fe_{0.962}Co_{0.038})_2As_2$ in a field TF = 40 G. The black squares are data taken at T = 1.65 K in a spin-rotated (SR) configuration, such that the initial muon spin direction is perpendicular to the crystallographic $\hat{c}$-axis. The other two sets of data, the red circles (T = 90 K) and the green triangles (T = 1.65 K) are taken in a non-spin rotated (non-SR) configuration, so that the initial muon spin direction is along $\hat{c}$. These spectra provide evidence for strong $\hat{c}$-axis magnetism, and no macroscopic phase separation of strongly- and weakly-magnetic regions.

must be small (on the order of nanometers), so that muons landing there will see the effect of the high-field contribution.

Fig. 4.4(a) and (b) show the precession frequencies, ω and relaxation rates, λ, from the TF-μSR data. The frequency decreases below the magnetic ordering transition, attributable to the decrease in local field, caused by an increase in the magnetic field disorder in the ordered region. Coupled with the in-

crease in the relaxation rate at the ordering temperature, there is significant evidence of magnetic disorder present in this system. The relaxation rate also saturates at a constant value towards T = 0, indicating that the disorder is not eliminated by removing thermal excitations. This picture of a highly disordered local magnetic structure is in agreement with other local probes, such as NMR [61, 40] and Mössbauer [62] that see a similarly disordered structure.

This is in contrast to neutron scattering measurements that see sharp magnetic Bragg peaks at all dopings where magnetism exists [59]. Below T_{SC}, there is a loss in intensity, but the peaks remain well-defined. Additionally, for dopings between $x = 0.056$ and $x = 0.060$, an incommensuration is observed in the magnetic structure that, while the shift depends on doping, continues to represent a well-defined magnetic structure [60]. Three particular explanations may provide a way to reconcile these two contrasting pictures: the timescale of the measurements, an incommensuration in the magnetic structure, or a combination of an ordered and a disordered magnetic moment.

The first explanation depends on fluctuations in the system that are dynamic (producing disorder) on the timescale of the μSR experiments, but appears static (producing order) on the neutron timescale. This would agree with the other local probes that work on similar timescales to μSR, such as NMR and Mössbauer ($\sim 10^{-7}$s). The second stems from the above-mentioned neutron experiments that saw incommensuration for higher Co-dopings than were studied in this experiment. Those measurements saw an incommensuration that increased with increasing doping, but was relatively small for all dopings studied [60]. It is possible that lower dopings, such as the ones studied in this

thesis, contain an incommensurate magnetic structure but that the splitting in the magnetic Bragg peaks is too small to be detected by neutron scattering. This would produce a broad distribution of local fields, appearing as magnetic disorder when measured with μSR. Finally, the magnetic moments in the system may be composed of two components: one that is well-ordered and one that is random. As a reciprocal space probe, neutron scattering would only be sensitive to the ordered component, producing well-defined magnetic Bragg peaks, while real space probes would see both components and appearing as disordered magnetism. This should manifest itself as a decrease in the ordered Fe moment as the disorder increases, which has been seen by neutron scattering in the isostructural $Ca(Fe_{1-x}Co_x)_2As_2$ [178]. In this compound, there is a reduction in the ordered moment per Fe atom of $\sim$25% at a relatively similar doping level.

By measuring TF-μSR in a larger field of TF = 0.02 T in both a field-cooled and zero-field cooled experiment, evidence of flux pinning is seen. This is seen through a strong increase in the relaxation between the two orientations, confirming the presence of superconductivity in these samples. Since the entire sample sees magnetism, superconductivity must exist in or near regions of strong local magnetism. There may be phase separation on a nanoscale, in agreement with scanning tunnelling spectroscopy measurements that finds no phase separation at longer length scales [179].

4.3 Superfluid Density of Optimally-Doped $Ba(Fe_{0.926}Co_{0.074})_2As_2$)

Measurements of the microscopic parameters through the method outlined in Sec. 3.2.4 can only be accurately performed in the absence of magnetic order. To check for static magnetism on the μSR timescale, ZF-μSR measurements were performed at T = 2 K and above T_{SC}. These spectra were identical, exhibiting only weak, temperature-independent relaxation. This is characteristic of a system of nuclear dipole moments, a fits to this data gave a characteristic relaxation rate of 0.15 μs^{-1}.

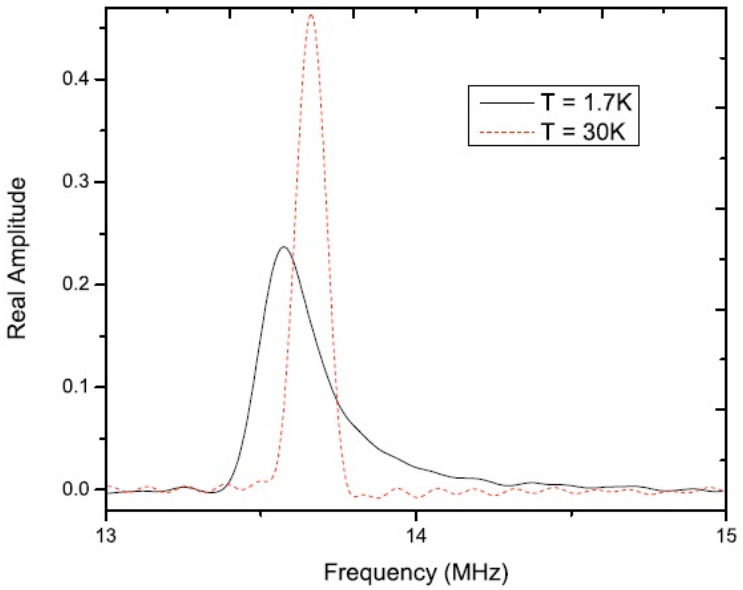

Figure 4.6: Fast Fourier transform of the TF-μSR signal in B = 0.1 T applied along the $\hat{c}$ crystallographic axis. The solid black line is taken at T = 1.7 K while the red dashed line corresponds to T = 30 K. The anisotropic shape at low temperature is characteristic of a well-ordered vortex lattice. Figure taken from [173].

Fig. 4.6 shows a fast Fourier transform (FFT) of the TF-μSR spectrum measured in TF = 0.1 T and T = 1.7 K and T = 30 K, the latter of which is above T_{SC}. The high temperature data is well-described by a Gaussian distribution, centered on $\nu = \gamma_\mu \cdot B_{app} = 13.54$ MHz, the precession frequency generated by $B_{app} = 0.1$ T. This Gaussian distribution of fields is the expected field distribution for a paramagnet. At low temperature, the field profile becomes anisotropic and is characteristic of an Abrikosov vortex lattice (See Sec. 3.2.4). This indicates the presence of at least a locally well-ordered vortex lattice within the superconducting state. The lower cutoff in the field distribution corresponds to muons landing at the center of three vortices (farthest from the vortex cores) while the high-field cutoff comes from muons landing in the vortex cores. The overall width of the lineshape is determined mostly by λ and the high-field cutoff is highly dependent on ξ. At the highest applied fields, far from the London limit, the field would be finite at the vortex cores, giving the most reliable measure of ξ.

This lineshape can be fit to an analytic Ginzburg-Landau model [180]. This allows the calculation of the magnetic field distribution in terms of the microscopic parameters, such as the penetration depth and the coherence length. These field distributions were then inverse Fourier-transformed, constructing theoretical time spectra that could be compared to the measured data. This allowed for the determination of λ and ξ by minimizing χ^2 with respect to these parameters. From this, it was possible to determine the Ginzburg-Landau parameter, $\kappa = \lambda/\xi$, obtaining $\kappa = 44$. This value was held fixed for the remainder of the analysis. This can be done since measurements performed at lower fields are insensitive to κ as long as it is large.

In addition to the Ginzburg-Landau model, a temperature-independent relaxation rate was included to account for nuclear dipole fields; this was fit using data above T_{SC} and then fixed to the fitted value of 0.089 μ^{-1}. Additionally, small-angle neutron scattering has detected a highly disordered vortex lattice in fields above 0.2 T [181]. The effect of this was included in the analysis by convoluting the model with a Gaussian in the frequency domain to account for a Gaussian broadening of the signal [161, 182]. It is assumed that this broadening was proportional to $1/\lambda^2$, as has been observed in previous studies of cuprates and other high-κ superconductors [180].

The fitted results for the RMS deviation of the vortex position, ($< s^2 >^{1/2}$, in units of length), relative to the vortex separation, L_0, is $< s^2 >^{1/2} / L_0 \approx 2.4\,\%$ at T = 1.7 K and H_{app} = 0.1 T. This deviation decreases with increasing temperature and decreasing field. (7 % in H_{app} = 0.05 T and 30 % in H_{app} = 0.02 T). In higher fields, this relatively low amount of vortex disorder is somewhat in contrast to small-angle neuron scattering [181], but may reflect that μSR, as a real-space probe, is less sensitive to the loss of true long-range order than reciprocal space probes. Bitter decoration measurements have shown at least a locally well-ordered vortex lattice [181], supporting this conclusion. This also lends support for the way this disorder was included in the fitting, and it is noted that the fitted values of the penetration depth are not particularly affected by this disorder.

With this fitting procedure, it was possible to reliably fit the rest of the parameters in the μSR signal, including the penetration depth, λ(H,T). Results for this analysis, plotted as $1/\lambda^2 \propto n_s/m^\star$ where n_s is the superfluid density,

are shown in Fig. 4.7 for applied fields of 0.1, 0.05 and 0.02 T. It can be clearly seen that both the temperature dependence and the zero-temperature value, n_s(T→0) depend on the applied field.

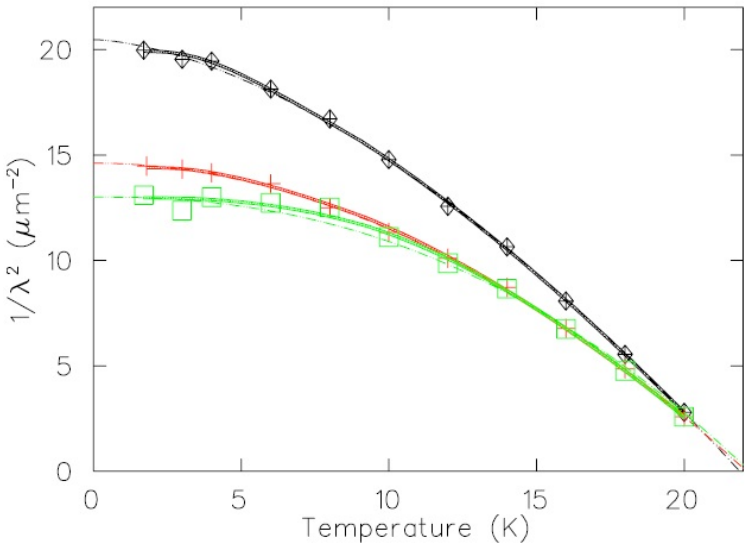

Figure 4.7: Combined two-gap fit (solid line) and power-law fit (dashed line) to the superfluid density measured from TF-μSR at fields of 0.02 T (black diamonds), 0.05 T (red crosses) and 0.1 T (green squares). Error bars are smaller than the plotting symbols. Figure taken from [173].

The temperature dependence of the superfluid density reflects how easily thermal fluctuations are able to create quasiparticles. In conventional weak-coupling BCS theory (See Chapter 1), one finds that the low-temperature behaviour of n_s becomes exponentially flat, whereas the presence of gap nodes is reflected in power-law behaviour. For example, one observes $n_s \propto$ T in the cuprate superconductors. To check for this behaviour, one can fit the data to a power law, given by:

$$n_s(T) = n_s(0)[1 - (T/T_{SC})^p] \tag{4.3}$$

The results of the fit are shown by the dashed lines in Fig. 4.7. The fitted power decreases with increasing field while the superfluid density at T = 0 decreases with field, as shown in Table 4.1. This model provides a fairly good fit to the data, but the strong dependence of both of these parameters on the magnetic field is surprising considering that all of the fields are much less than the upper critical field, H_{c2} [38]. This prompts an effort to try other models that may characterize the behaviour of the superfluid density.

Field (T)	n_s**(0)** (μ**m**$^{-3}$)	**Power,** p
0.02	20.47±0.15	1.62±0.03
0.1	13.01±0.05	2.27±0.03

Table 4.1: Values obtained for $n_s(0)$ and p from the power law fits shown in Fig. 4.7. Data taken from [173].

As described in Chapter 1, a leading proposal for the superconducting gap structure is a combination of two s-wave gaps, in the $s_\pm$ configuration. Multi-gap superconductors have been realized in other systems, including MgB_2 [183, 184] and $NbSe_2$ [185], which can be clearly observed by measuring the temperature dependence of the magnetic penetration depth using μSR [180, 186]. To check if these measurements are consistent with such a multi-gap picture, the data was fit to a phenomenological two-gap

model [187, 188] which was successfully employed in a previous μSR study of LaFeAs(O,F), Ca(Fe,Co)AsO and (Ba,K)Fe_2As_2 [189], given by:

$$n_s(T) = n_s(0) - w \cdot \delta n_s(\Delta_1, T) - (1 - w) \cdot \delta n_s(\Delta_2, T) \tag{4.4}$$

where w is the relative weight of the first gap, Δ_1. The gap functions are given by:

$$\delta n_s(\Delta, T) = \frac{2n_s(0)}{k_B T} \int_0^\infty f(\epsilon, T) \cdot [1 - f(\epsilon, T)] d\epsilon \tag{4.5}$$

where $f(\epsilon, T)$ is the Fermi distribution:

$$f(\epsilon, T) = (1 + e^{\sqrt{\epsilon^2 + \Delta(T)^2}/k_B T})^{-1} \tag{4.6}$$

Here, Δ_i ($i = 1$ and 2) are the energy gaps at T = 0 and $\Delta_i(T)$ are taken to follow the standard BCS temperature dependence. The size of the gaps, Δ_1 and Δ_2, and T_{SC} were fit globally while $n_s(0)$ and the weighting factor, w, were allowed to be field-dependent.

The results of this fitting are shown by the solid lines in Fig. 4.7. This gives a very good fit to the data, with a χ^2 that is approximately half of that for the power law fit. Based on the other experimental support for the two gap model, this validates the choice of this fitting function. From the fits, the values of the gaps were $2\Delta_1/k_B T = 3.768 \pm 0.009$ and $2\Delta_2/k_B T = 1.57 \pm 0.05$. The fits also gave $T_{SC} = 22.1 \pm 0.2$ K. The larger of the two gaps is close to the BCS value while the smaller gap is roughly half the BCS gap. This is lower than has been

reported for other pnictide compounds, which presumably indicates that the strength of the superconducting pairing varies from system to system. These values are, however, in excellent agreement for other measurements of the two gap values reported by specific heat, $2\Delta_1/k_BT = 3.75$ and $2\Delta_2/k_BT = 1.65$, at the same doping [190, 191].

The relative weighting factor for the larger gap increases with B_{app} and the superfluid density decreases with B_{app}, as shown in Table 4.2. This indicates that the effect of the applied field is to weaken superconductivity on the bands with the smaller gap.

Field (T)	**Weighting factor,** w	n_s**(0)** (μ**m**$^{-3}$)
0.02	0.655±0.007	19.1±0.1
0.05	0.766±0.006	14.411±0.004
0.1	0.909±0.004	13.0±0.1

Table 4.2: Values obtained for the weighting factor, w, and superfluid density, $n_s(0)$, from the two-gap fits shown in Fig. 4.7. Data taken from [173].

Finally, the magnetic field dependence of the penetration depth and superfluid density were studied at the lowest measured temperature, T = 1.7 K, using field cooling through T_{SC}. By simultaneously fitting pairs of μSR spectra at T = 1.7 K and in the normal state, at each measured field, using the same procedure as outlined above, the value of the penetration depth (and thus, the superfluid density) can be reliably obtained. The results of this analysis are shown in Fig. 4.8. The superfluid density shows a small peak near 0.02 T, then decreases with increasing field, in agreement with the temperature scans. The

peak at low field may reflect the proximity to the lower critical field, estimated to be ≈ 0.007 T at T = 5 K [192]. The penetration depth also tends to a constant value of around 300 nm at higher fields. Recalling the field-dependence of the weighting factor, this may reflect the loss of superconductivity on the bands with the smaller gap.

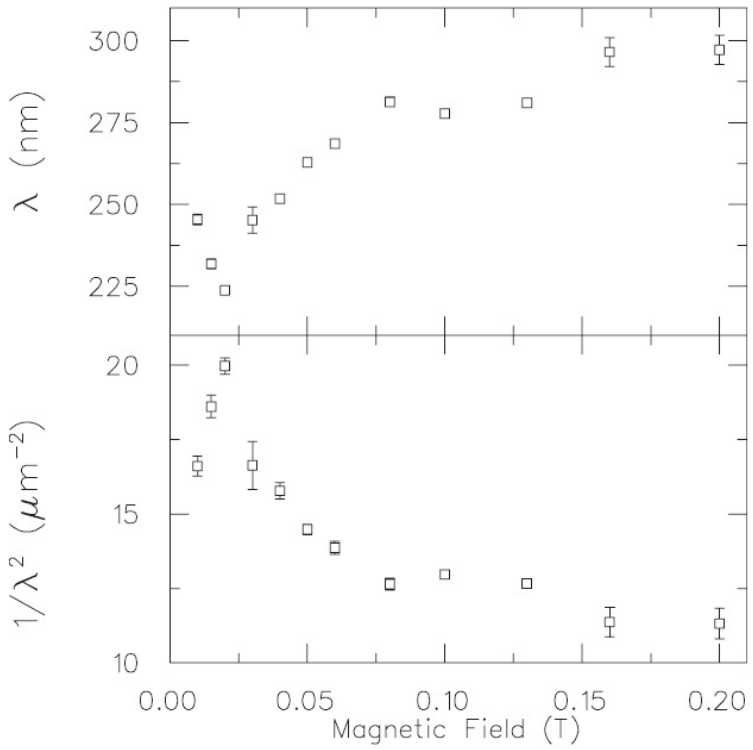

Figure 4.8: (Top) Magnetic field dependence of the magnetic penetration depth in $Ba(Fe_{0.926}Co_{0.074})_2As_2$ measured at T = 1.7 K. (Bottom) $1/\lambda^2 \propto$ superfluid density, n_s, measured at T = 1.7 K. Figure taken from [173].

4.4 Superfluid Density of Overdoped $Ba(Fe,Co)_2As_2$

Extending the analysis of Section 4.3 to other dopings in the series, the lineshapes characteristic of an Abrikosov lattice continue to be present at dopings above $x = 0.061$, as well as in the related compound $Sr(Fe_{0.87}Co_{0.13})_2As_2$, shown in Fig. 4.9. It is also noted at ZF-μSR spectra in all of these samples confirm that there is no static magnetic order or spin freezing down to T = 1.7 K.

As with the analysis in Section 4.3, Fourier transforms of the TF-μSR spectra were constructed, and all dopings measured show an anisotropic lineshape below T_{SC} characteristic of an Abrikosov vortex lattice. The lineshapes for some of the dopings measured are shown in Fig. 4.9 for applied fields of 0.02 T and 0.1 T. These measurements are indicative of at least locally well-ordered vortices, and all are consistent with a triangular vortex lattice. This can be inferred because a square lattice would show a peak (most likely field) that is much more separated from the minimum in the field distribution, owing to the larger average separation between the vortices [160].

Fitting to the analytic Ginzburg-Landau model, as above, yields reliable values for the penetration depth, λ, and the coherence length, ξ. Similarly, the effect of vortex lattice disorder was incorporated via a Gaussian broadening of the lineshape. The trends found in the optimally-doped sample were found to exist at all dopings. Namely, the RMS deviation fo vortex positions is greatest in lower fields (up to 30% in 0.02 T, but as small as 2% in 0.1 T) and decreases

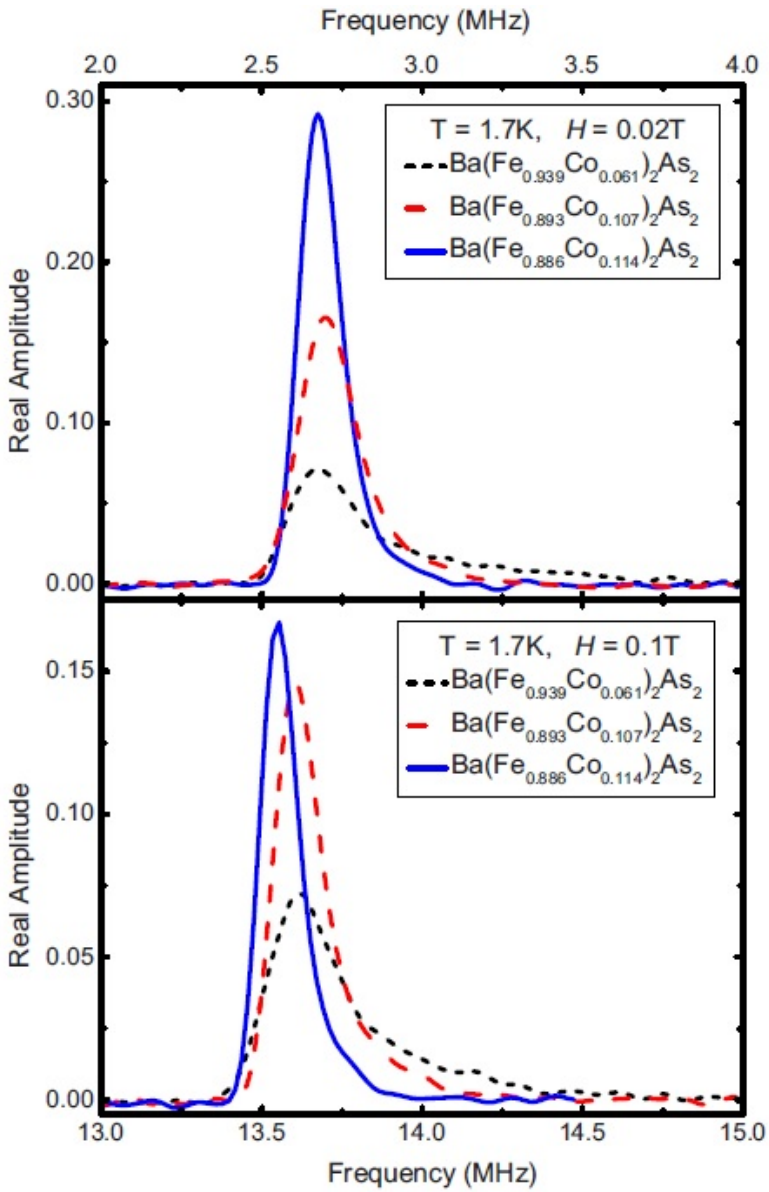

Figure 4.9: Fourier transforms of the TF-μSR spectra for $Ba(Fe_{1-x}Co_x)_2As_2$, showing the anisotropic lineshapes characteristic of an Abrikosov vortex lattice. Figure taken from [174].

with increasing temperature. Furthermore, the samples with the highest T_{SC} showed the largest amount of lattice disorder.

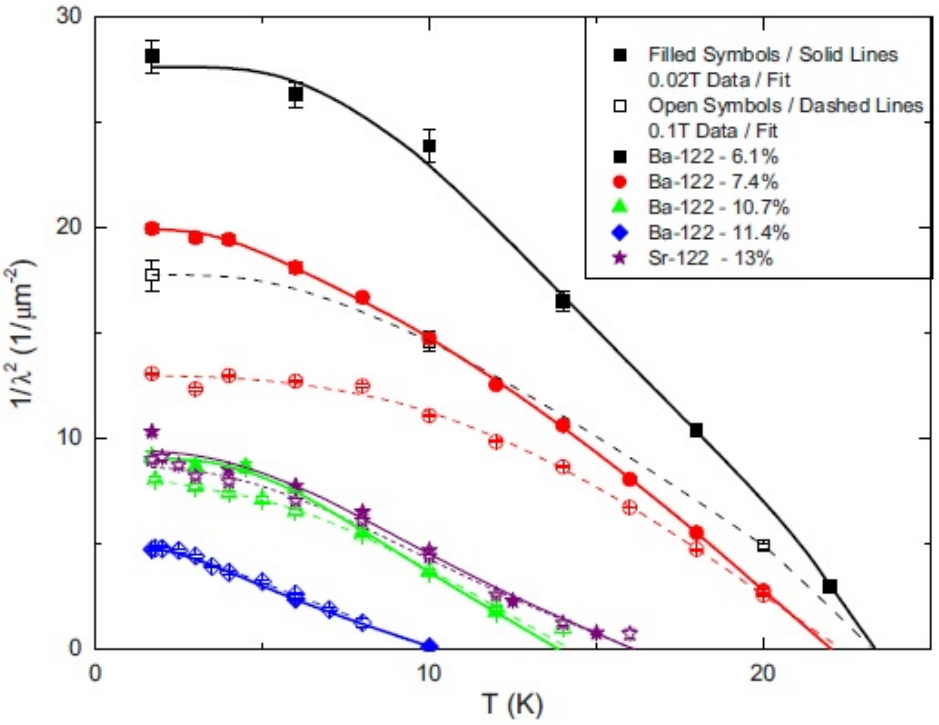

Figure 4.10: Superfluid density $n_s \propto 1/\lambda^2$ as a function of temperature for the $(Ba,Sr)(Fe,Co)_2As_2$ samples measured. The filled symbols and solid lines are the measured values and two-gap fits in TF = 0.02 T, respectively, while the open symbols and dashed lines are the measurements and fits in TF = 0.1 T. Figure taken from [174].

Fig. 4.10 show the results of this analysis for applied fields of 0.02 T and 0.1 T. The lines show fits to the data using a phenomenological model given in Eq. 4.4. Once again, the gap values and T_{SC} were fit globally, while the weighting factor, w, and the superfluid density were allowed to be temperature and field-dependent. Additionally, no parameters were common between the different dopings, allowing the doping-dependence of each parameter to be studied. As was the case with the optimal doping, the two-gap model fits the

data with a very reasonable χ^2 and fits using a single s-wave gap did not give satisfactory results.

For most samples, the larger gap was $2\Delta/k_BT_{SC} \approx 3.7$, which is close to the BCS value. For the $Sr(Fe_{0.87}Co_{0.13})_2As_2$ sample, the larger gap value was $2\Delta/k_BT_{SC} \approx 2.7$, lower than the BCS value. For the larger Co-dopings, $Ba(Fe_{0.893}Co_{0.107})_2As_2$ and $Ba(Fe_{0.886}Co_{0.114})_2As_2$, most of the weight was on the smaller gap. This may suggest gap anisotropy or even nodes in this doping regime. The steep temperature dependence of the superfluid density shows that the gap is not a single s-wave, though whether this is evidence for a non-s-wave gap as suggested by tunnel diode resonator measurements [192, 193] or multiple s-wave gaps is not possible to distinguish. However, our fits do allow a reliable extraction of the penetration depth approaching T = 0, $\lambda_0 \equiv \lambda(T \to 0)$. This was done at both fields, which then allowed extrapolation to B = 0. These results are given in Table 4.3.

	T_{SC}	λ_0(0.02 T)	λ_0(0.1 T)	λ_0(B = 0)
$Ba(Fe_{0.939}Co_{0.061})_2As_2$	23.6	189.4 ± 1.1	240.5 ± 2.0	182.6 ± 1.4
$Ba(Fe_{0.926}Co_{0.074})_2As_2$	22.1	224.2 ± 0.6	277.4 ± 1.0	216.8 ± 0.7
$Ba(Fe_{0.893}Co_{0.107})_2As_2$	14.1	332.2 ± 2.2	348.3 ± 4.6	329.3 ± 3.4
$Ba(Fe_{0.886}Co_{0.114})_2As_2$	10.3	453.8 ± 2.6	448.0 ± 2.4	454.9 ± 3.6
$Sr(Fe_{0.87}Co_{0.13})_2As_2$	16.2	325.5 ± 0.5	339.8 ± 0.6	322.8 ± 0.7

Table 4.3: Results of fitting $1/\lambda^2(T)$ to Eq. 4.4 for T_{SC} (in K) and λ_0 (in nm). Also shown are values of λ_0 extrapolated to B = 0. Data taken from [174].

Over the range of dopings studied, $1/\lambda_0^2$ varies considerably, nearly an order of magnitude, from 5 μm^{-2} to 30 μm^{-2}. The field dependence is rather pronounced for the $x = 0.061$ and 0.074 dopings, but almost entirely absent for the

higher dopings, due to the smaller superfluid density. This field-dependent behaviour has been observed in other pnictide samples by other techniques [194]. Calculations of the field-dependence of a multiband superconductor suggest that strong field dependence should be observed for fields on the order of the smaller gap [195], which could partially explain this behaviour in the $x = 0.107$ and 0.114 samples, particularly because most of the weight was on the smaller gap for these samples. However, the field dependence seen here is actually larger than would be expected. This likely indicates that one or both of the gaps are anisotropic and/or have nodes.

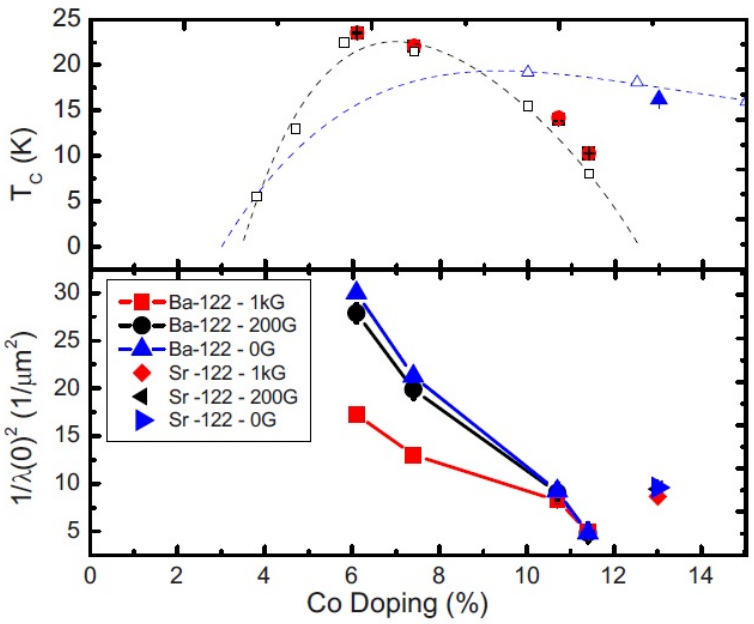

Figure 4.11: Superconducting T_{SC} and $1/\lambda_0^2$ for $Ba(Fe_{1-x}Co_x)_2As_2$ and $Sr(Fe_{1-x}Co_x)_2As_2$ as a function of Co concentration x, measured in TF = 0.02 T and 0.1 T, and for extrapolated values to B = 0. The open points and dashed lines are the measured T_{SC}'s and the superconducting dome taken from [31] for $Ba(Fe_{1-x}Co_x)_2As_2$ and from [196] and [197] for $Sr(Fe_{1-x}Co_x)_2As_2$. Figure taken from [174].

The calculated values of λ_0 at both fields as a function of Co doping is shown in Fig. 4.11. Also shown is the superconducting dome, the plot of T_{SC} versus Co-doping using data from [31, 196, 197]. As described in Section 1.1, the cuprates exhibit a strong, roughly linear correlation between T_{SC} and the superfluid density divided by the effective mass [22]. To check for this relation in this system, the extrapolated zero-temperature superfluid density was plotted against T_{SC} in Fig. 4.12. In contrast to Fig. 4.11, the points from the two fields here lie on almost the same line. This suggests that the superconducting T_{SC} is apparently determined by the carrier density divided by the effective mass.

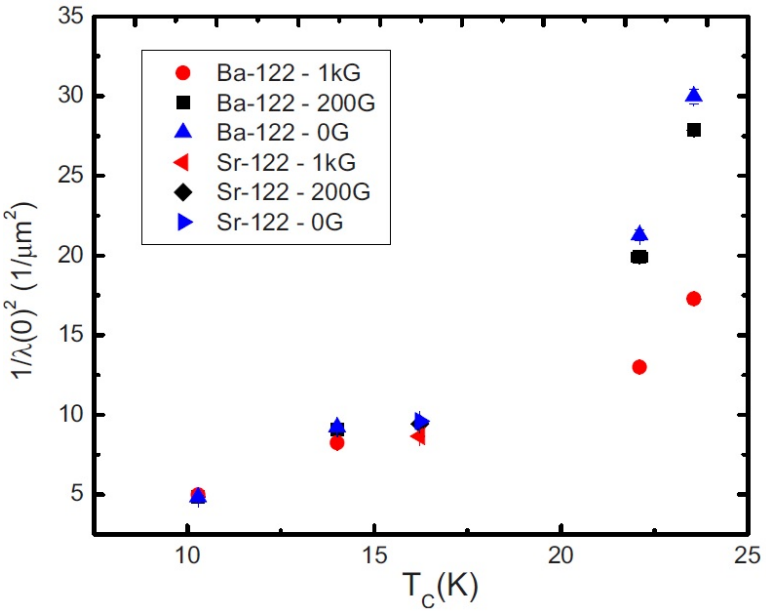

Figure 4.12: Superconducting T_{SC} versus $1/\lambda_0^2$ for $Ba(Fe_{1-x}Co_x)_2As_2$ and $Sr(Fe_{1-x}Co_x)_2As_2$ as a function of Co concentration x, measured in TF = 0.02 T and 0.1 T, and for extrapolated values to B = 0. Figure taken from [174].

Specific heat measurements of the superconducting transition found that the jump at the superconducting transition was correlated with the value of T_{SC} as $C_p/T_{SC} \propto T_{SC}^2$ [198]. Comparing this to the measured superfluid density data (shown in Fig. 4.13), it can be seen that both sets of data fit well to a straight line with $n \approx 2$, indicated by the dashed line. This correlation in both the specific heat and superfluid density was observed in cuprates [199, 200, 201], suggesting some commonalities between them.

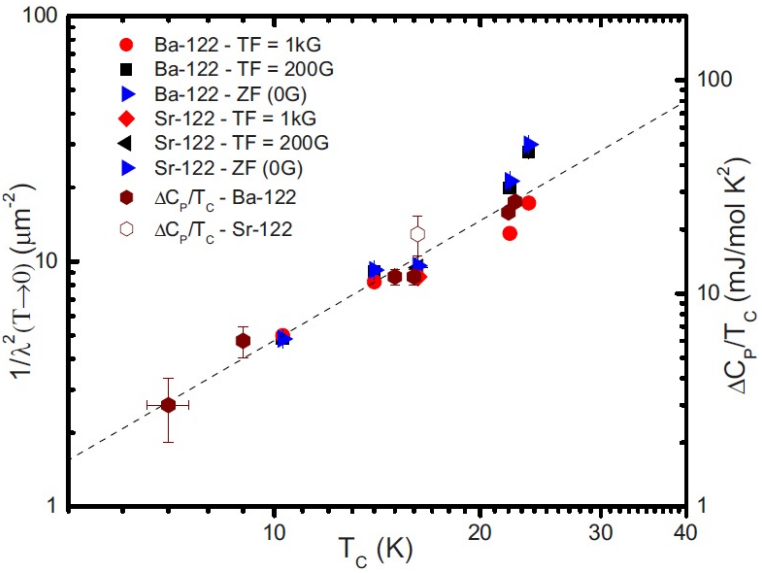

Figure 4.13: $1/\lambda_0^2$ versus superconducting T_{SC} for $Ba(Fe_{1-x}Co_x)_2As_2$ and $Sr(Fe_{1-x}Co_x)_2As_2$ as a function of Co concentration x, measured in TF = 0.02 T and 0.1 T, and for extrapolated values to B = 0. This is plotted with $\Delta C_p/T_{SC}$ from [198]. The dashed line has slope $n = 2$ and is a guide to the eye. Figure taken from [174].

4.5 Field-Induced Magnetism in Overdoped $Ba(Fe,Co)_2As_2$

The fitting process described in the preceding sections contains several parameters that are fit from the data. One of these is the average muon precession frequency, ν_μ, which is slightly larger than the peak frequency. In the normal state, this precession frequency can be expressed as:

$$\nu_\mu = (1 + K_\mu)\gamma_\mu B_{app} \tag{4.7}$$

where B_{app} is the applied magnetic field, γ_μ is the muon gyromagnetic ratio and K_μ is the muon Knight shift. In the superconducting state, the precession frequency is usually slightly reduced compared to the normal state, due to flux expulsion. The fractional shift in the muon precession frequency, $\nu_S/\nu_N - 1$ as a function of temperature is shown in Fig. 4.14. It can be seen that, except for a negative shift below T_{SC} for some samples due to bulk screening, all samples show an increasing frequency shift with decreasing temperature. This is not what is expected from a bulk superconductor with triplet pairing (temperature-independent shift) or singlet pairing (Yoshida function). Similar shifts have been observed in other pnictide superconductors [202], and cannot be explained by bulk screening, which only gives a negative contribution.

The fractional shift is much larger in TF = 0.02 T as compared to 0.1 T. In fact, the absolute frequency shift, $\nu_S - \nu_N$, is roughly the same for the two fields. The shift is also larger for samples with larger T_{SC}'s and superfluid densities, $n_s/m^\star \propto 1/\lambda_0^2$. Previous μSR studies of the electron-doped cuprate

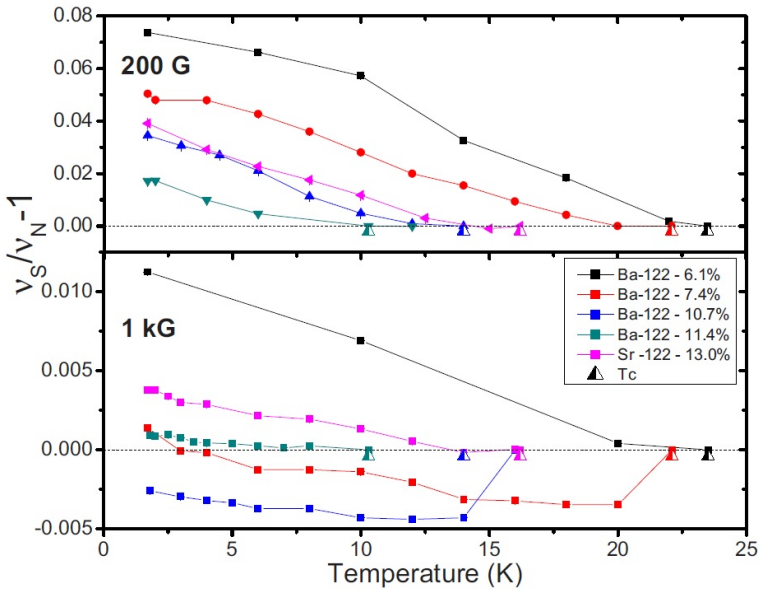

Figure 4.14: Fractional shift of the muon precession frequency, $\nu_S/\nu_N - 1$, relative to the normal state frequency, ν_N. The superconducting transition temperatures are indicated by triangular symbols. Figure taken from [174].

superconductor $Pr_{2-x}Ce_2CuO_4$ also exhibited a positive frequency shift below T_{SC} which was taken as evidence for field-induced magnetism [203]. In that case, the absolute shift decreased with increasing field, indicating moments aligned perpendicular to the applied field. In the pnictide case, that the absolute shift appears to be field-independent may suggest that the field-induced magnetism is along the ĉ-axis, the direction of the applied field, and is ferromagnetic in character. An antiferromagnetic alignment would produce a split of the precession frequency, rather than a shift. Finally, since it onsets at T_{SC}, it suggests that this is a property of the superconducting state.

4.6 Conclusions

Measurements of the underdoped samples ($x = 0.038$ and $x = 0.047$) showed strong $\hat{c}$-axis magnetism, occurring below T_{SDW}. The size of the local field and the magnetic volume fraction did not change below the superconducting transition. There is a residual volume fraction that displays low-field magnetism, increasing with increasing Co-doping. The measurements suggest that the local magnetic field is increasingly disordered as the concentration of Co increases.

Since neutron scattering measurements see well-ordered magnetic moments [59], the disorder seen by local probes (such as the experiments of Sec. 4.2) must be reconciled. Possible explanations of this discrepancy are that there are fluctuations on the timescale of the μSR experiments to which neutron scattering is insensitive, that there exists an incommensuration in the magnetic order that is too small to be detected, or that there are both an ordered and a disordered moment in the system.

These samples were shown to exhibit both superconductivity and magnetism using larger transverse field of 0.02 T. This may suggest some nanoscale phase separation, but that the entire samples sees magnetism means that superconductivity exists in or near regions of strong magnetic order.

The samples of $Ba(Fe_{1-x}Co_x)_2As_2$ with $x = 0.061$, 0.074, 0.107, 0.114 and the sample of $Sr(Fe_{0.87}Co_{0.13})_2As_2$ were measured with ZF-μSR and no magnetic ordering was found down to T = 1.65 K. This allowed TF-μSR measurements to be performed on these samples to study their superconducting properties.

In the first sample studied, $Ba(Fe_{0.926}Co_{0.074})_2As_2$, an analytic Ginzburg-Landau model was used to fit the data and obtain absolute values for the penetration depth, λ. The fitted value for the Ginzburg-Landau parameter $\kappa = 44$, confirming that the material is in the extreme type-II limit. The temperature-dependence of the superfluid density, $n_s \propto 1/\lambda^2$ can be well-described by an s-wave two-gap model where the field-independent gaps are $2\Delta_1 = 3.77 k_B T_{SC}$ and $2\Delta_2 = 1.57 k_B T_{SC}$.

Expanding the analysis to the remaining compounds by fitting to the two-gap models produces similarly successful results, where the gaps follow the same temperature dependence. It was found that the superfluid density as $T \to 0$, $n_s(0)$, varies roughly quadratically with the superconducting transition temperature, T_{SC}. The superfluid density also decreases with increasing doping, *ie.* as normal state charge carriers are added to the system. This may suggest a form of electronic phase separation, either in real or reciprocal space. Finally, a paramagnetic frequency shift was observed below T_{SC}, where the absolute frequency shift was independent of the applied magnetic field. This, coupled with the decrease of the absolute shift with increasing Co concentration, suggests that the Fe moments experience field-induced magnetism along the $\hat{c}$-axis below the superconducting transition.

Chapter 5

Neutron Scattering Measurements of URu_2Si_2

This Chapter details two neutron scattering measurements of URu_2Si_2 under different perturbations to the "hidden order" state. When Re is substituted for Ru, the hidden order phase is suppressed and the system moves towards a ferromagnetic phase. These results are presented in Sec. 5.2, and have been previously published in [204]. Under hydrostatic pressure, the system is perturbed into an antiferromagnetic phase. This is the basis for the measurements in Sec. 5.3, and are contained in a paper that will soon be submitted for publication [205].

5.1 Introduction

As described in Section 2.3, neutron scattering measurements have seen spin correlations at commensurate (1 0 0) and incommensurate (1.4 0 0) wave vectors. These are thought to be connected to the nature of the hidden order in this material.

Transport measurements on $URu_{2-x}Re_xSi_2$ had been performed previously [137, 206, 207] and had found that Re-doping suppresses the hidden order, as shown in the phase diagram (Fig. 5.1). It has also been shown that the application of hydrostatic pressure enhances T_0 before giving rise to an antiferromagnetic phase.

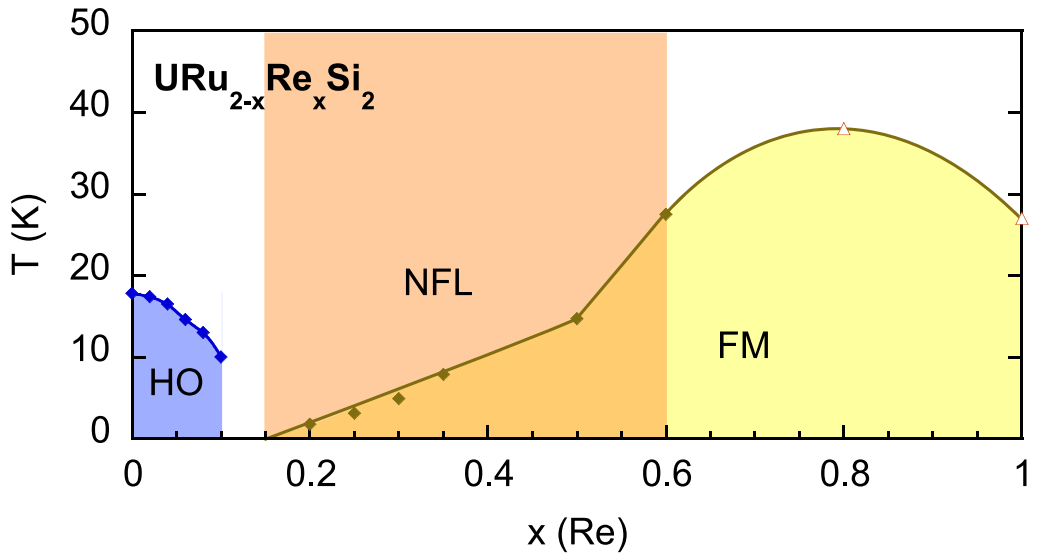

Figure 5.1: Magnetic Phase diagram of $URu_{2-x}Re_xSi_2$ showing the antiferromagnetic (hidden order) and ferromagnetic phases. Figure taken from [137] and used with permission. See also [206] and [207].

The response of the spin correlations under these perturbations are discussed in this Chapter, in an effort to elicit the properties of the hidden order phase.

5.2 Measurements of Re-doped $URu_{1.9}Re_{0.1}Si_2$

To check for static magnetism, elastic scattering was performed at 2 K, in the hidden order phase, and no peaks were observed at either the commensurate or incommensurate points. This is in contrast to the parent material, where a minority phase creates weak elastic scattering at these points [120], so any static moment in the Re-doped compound must be smaller than what is observed for the parent compound $\sim 0.03\ \mu_B$.

To measure the change in the inelastic spectrum across T_0, the scattering along the (H 0 0) direction at an energy transfer of 2.9 meV was measured at 2 K and 40 K, shown in Fig. 5.2. At 2 K, the scattering shows the relative strength expected from the magnetic form factor at equivalent incommensurate wave vectors (0.6 0 0) and (1.4 0 0). At this temperature, the scattering at the commensurate (1 0 0) position also exhibits comparable strength. The fast neutron background is shown, as well as the total sample background, obtained from the fitting, described below.

The change in scattering as a function of temperature, both at the commensurate and incommensurate positions, can be used to identify the hidden order transition. At 40 K, well above the hidden order transition, the incommensurate scattering remains quite strong at 2.9 meV. It appears with roughly half the intensity as in the hidden order phase, but the commensurate scattering has been diminished significantly. This is consistent with the idea that the commensurate (1 0 0) fluctuations are the signature of the hidden order phase [208]. Fig. 5.3 shows the temperature dependence of the commensurate (1 0 0) fluctuations at 1.65 meV. This measurement was performed under different experimental conditions, which accounts for the change in background

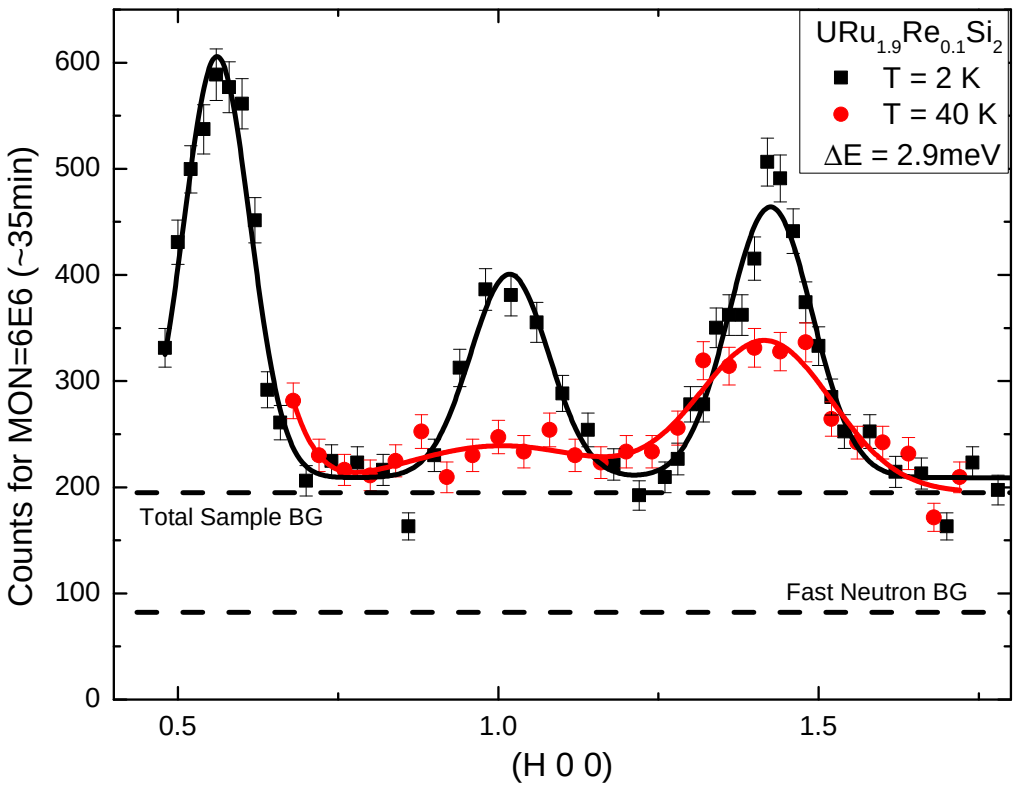

Figure 5.2: Inelastic scattering along the (H 0 0) direction for an energy transfer of 2.9 meV at T = 2 K (black squares) and T = 40 K (red circles). At 40 K, well above the hidden order transition, there is partial suppression of the incommensurate fluctuations. In contrast, there is almost complete suppression of the commensurate fluctuations. The lines are Gaussian fits at each of the three peak positions. Figure taken from [204].

compared to Fig. 5.2, but with the same array of single crystals. A discontinuity in the temperature dependence of the peak is observed around ∼13 K, which may indicate the onset of the hidden order phase. This change is not as clear as in the parent material [208], but this is likely due to electronic disorder associated with Re doping. The reduction of T_0 at this level is in agreement with previous results [140, 206, 209].

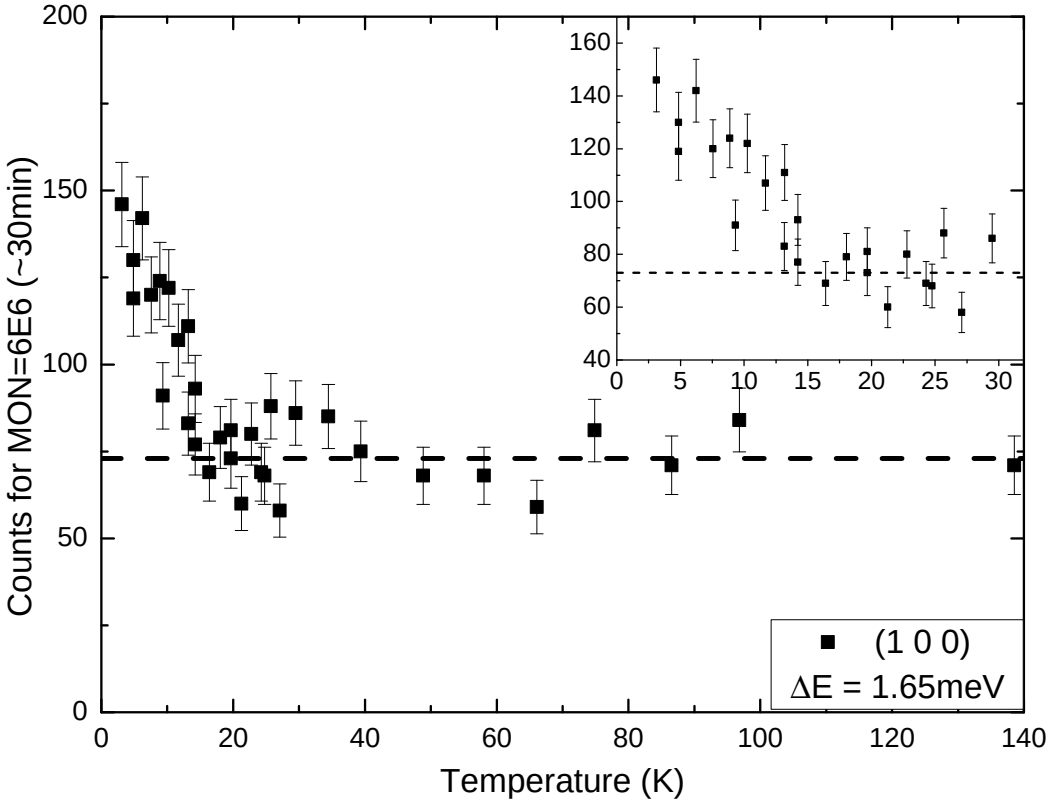

Figure 5.3: The temperature dependence of the commensurate (1 0 0) fluctuations in $URu_{1.9}Re_{0.1}Si_2$ at 1.65 meV. The onset of order parameter-like behaviour is observed around at the hidden order phase transition, T = 15 K. The inset shows a close-up of the data below 30 K. Figure taken from [204].

Energy scans at $\vec{Q}$ = (1.4 0 0) comparing the Re-doped sample with the pure material are shown in Fig. 5.4. The data have been normalized to a constant volume for the two crystals via phonon measurements at (2.3 0 0) and (1.8 0 0), respectively. The spectrum of $URu_{1.9}Re_{0.1}Si_2$ also exhibits an incommensurate spin gap similar to that in pure URu_2Si_2 [115, 210], but Re-doping seems to lower the value of the gap.

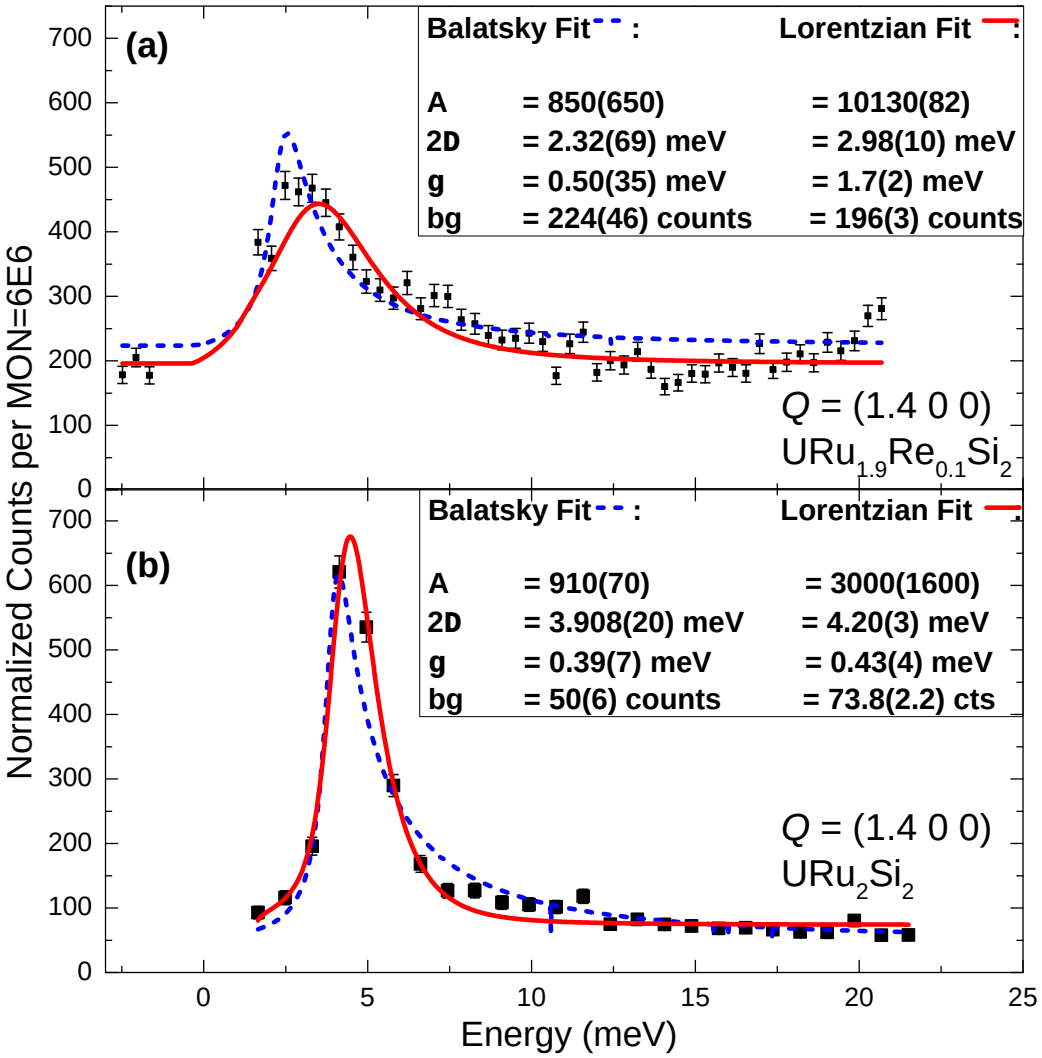

Figure 5.4: The fits to the incommensurate fluctuations for (a) $URu_{1.9}Re_{0.1}Si_2$ at T = 2 K and for (b) URu_2Si_2 at T = 3 K and 5 K (combined data). The blue line is the fit to Eq. 5.1 and the red line is a fit to a Lorentzian of energy 2Δ, amplitude A, and damping 2γ = FWHM, convoluted with the resolution function, as described below. For the Re-doped case, the nesting gap energy, Δ, is reduced to 60% of its value in the pure system. Figure taken from [204].

The normalized intensity in Fig. 5.4 shows that doping has reduced the intensity at the incommensurate wave vector by a factor of two, obtained from

the integrated intensity of the peaks. Re doping also increases the spectral width as seen in Fig. 5.4, showing that the fluctuations are highly damped by doping. The slowing of the fluctuations is more dramatic at the commensurate wave vector, as shown in Fig. 5.5. There, the lifetime is so short that the characteristic energy barely gives a peak in the spectrum. It may also signal the destruction of perfect nesting by charge impurities.

Band structure calculations and ARPES measurements suggest that there is partial Fermi surface nesting at the incommensurate wave vector [210, 107]. A theory based on a spin resonance in the hidden order state, involving transitions between nested parts of the Fermi surface separated by $\vec{Q} = (1.4\ 0\ 0)$ has been proposed by Balatsky *et al.* [107]. This spin resonance leads to the appearance of a particle-hole condensate [107]. The fermion energies are assumed to rise quadratically above the hidden order gap, $\Delta_{\vec{Q}^\star}$, allowing pairs of excitations to contribute to the dynamic susceptibility measured by by neutron scattering [107]. The data of Fig. 5.4 are fairly well-described by this theoretical model, given by:

$$\chi^{zz}(\vec{Q}^\star, \omega) = A^2 |\Delta_{\vec{Q}^\star}|^2 \int \frac{1}{\sqrt{E^2 - \Delta_{\vec{Q}^\star}}} \frac{1}{\omega^2 - 4E^2} dE \tag{5.1}$$

to which a constant background (bg) has been added, shown by the blue lines in Fig. 5.4. In this model, the gap in the spin spectrum in Fig. 5.4 is equal to $2\Delta_{\vec{Q}^\star}$.

In Fig. 5.4, the model for the spectrum has been convoluted with the four-dimensional instrumental resolution using RESLIB, as described in Sec-

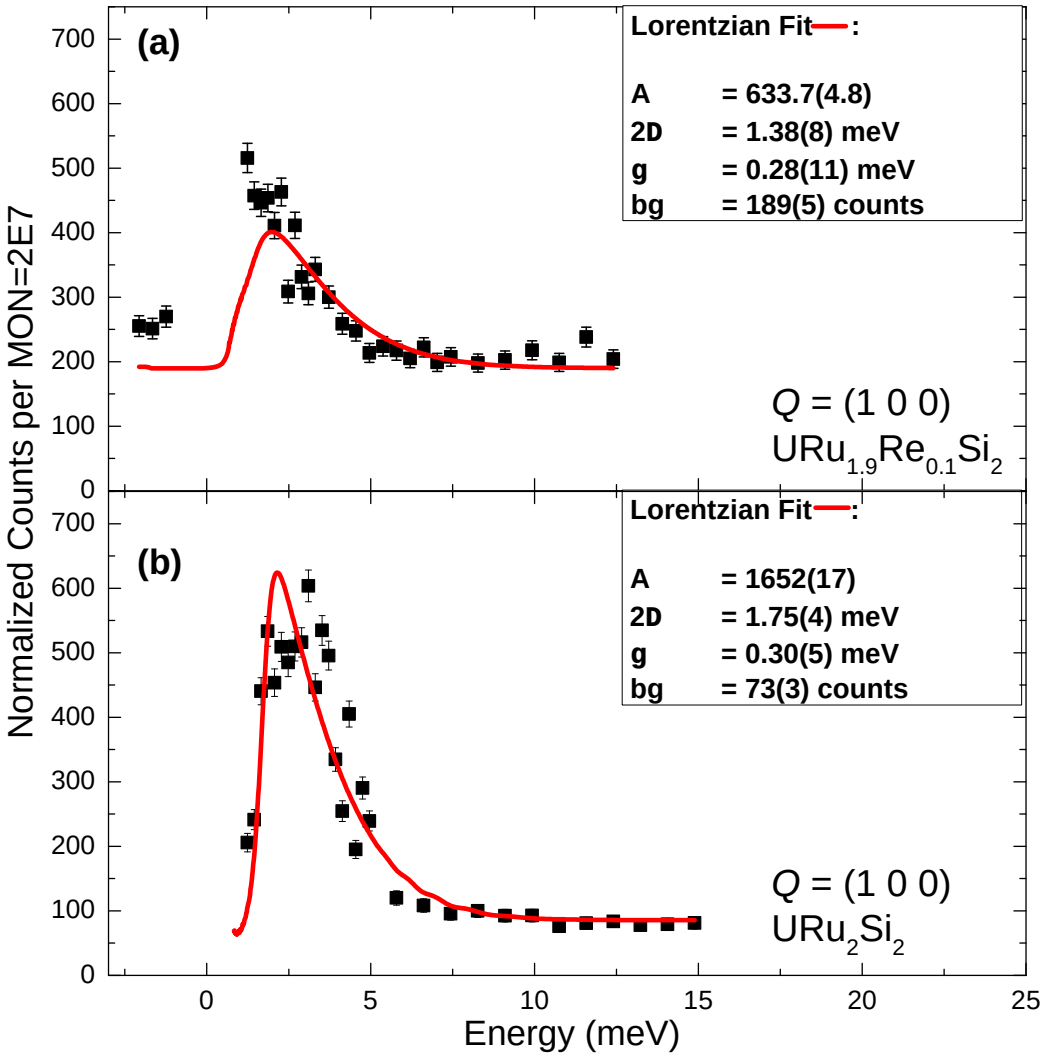

Figure 5.5: (a) The elastic scattering at (1 0 0) in the $URu_{1.9}Re_{0.1}Si_2$ sample, measured at T = 2K. (b) The (1 0 0) inelastic scattering in the pure URu_2Si_2 system, measured at 3 K and 5 K (combined data). Both were fit to a Gaussian for the elastic peak and a Lorentzian of energy $\omega_{\vec{Q}} = 2\Delta$, amplitude A, and damping 2γ = FWHM for the inelastic peak, convoluted with the resolution function. The commensurate fluctuations of the hidden order state are damped in the presence of Re-doping. Figure taken from [204].

tion 3.3.5 [171]. The required spin velocities were taken from Ref. [115]. The spectrum was broadened slightly to deal with the square root singularity of Eq. 5.1 by adding a small imaginary part γ to the frequency in such as way that it is analogous to the broadening γ of Fig. 5.4 described in relation to Eq. 5.2. The data has been corrected for higher-order perturbation of the monitor rate. This has been done since the amount of higher-order scattering in the monochromator is energy-dependent, but is known for most instruments and so this can be corrected in the analysis.

Recent measurements of the inelastic scattering along (H 0 0) have been analyzed in terms of a peak and a continuum [208]. In contrast to this work, no additional continuum was needed to describe the data. However, attempts to fit the commensurate excitations to the Balatsky nesting equation did not converge. Therefore, the spectra at both the commensurate and incommensurate points were fit to Lorentzians, give by:

$$I(\vec{Q}^{\star},\omega) = \frac{A}{\omega_{\vec{Q}^{\star}}}[\frac{1}{(\omega-\omega_{\vec{Q}^{\star}})^2+\gamma^2} - \frac{1}{(\omega+\omega_{\vec{Q}^{\star}})^2+\gamma^2}] \tag{5.2}$$

This was multiplied by a Bose factor, and convoluted with the resolution function, as described above and in Sec. 3.3.5. The commensurate fluctuations at (1 0 0) for the Re-doped and parent samples are shown in Fig. 5.5(a) and 5.5(b), respectively. Compared to the parent compound with a spin gap of 1.75 meV, the commensurate fluctuations are peaked at a lower energy, 1.38 meV. This corresponds to a reduction factor of 0.79, which tracks the reduction of T_0. Within a nesting picture, it appears that Re impurities greatly weaken the nesting that is present in the pure system.

As temperature is increased, the commensurate fluctuations are destroyed much more quickly than the incommensurate ones. Thus, the hidden order gap (the gap around (1 0 0)) becomes much less well-defined. Both the commensurate and incommensurate spectral form is that of a resonant frequency that decays into the Re-induced continuum of the itinerant particle-hole states. The Re-doping achieves this by $\vec{Q}$-broadening the nesting that gave the well-defined spectral onset above the gap. The relatively large spin wave velocities [115] then convert the $\vec{Q}$-broadening into an observed spectral broadening. This suggests that the gap may vanish when the quantum phase transition to ferromagnetism is reached.

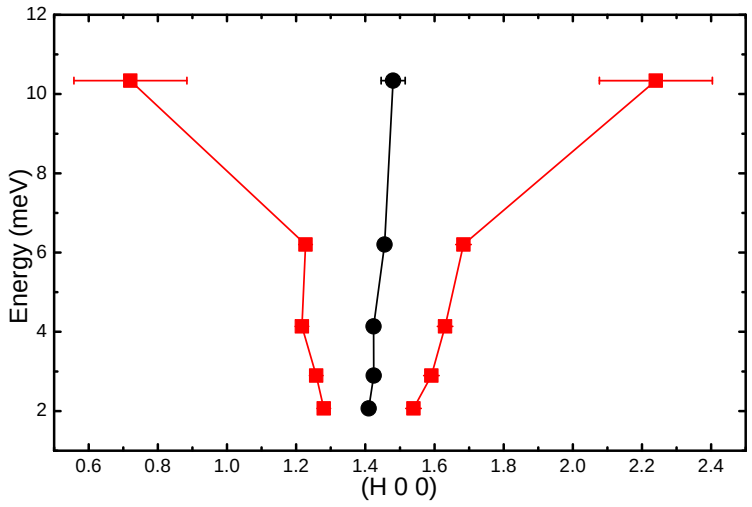

Figure 5.6: Locus of the half-widths in reduced wave vector, H, of spin fluctuations around (1.4 0 0). These inverse dynamic correlations lengths are narrow in wave vector for low energies, but they broaden significantly at higher energies. The black circles are the center of the peak, while the red squares are the FWHM of the peaks. The error bars for the low-energy data lie within the points. Figure taken from [204].

The $\vec{Q}$-width of the incommensurate excitations is shown in Fig. 5.6 as a function of energy. Constant energy scans were measured along (H 0 0) at energies ranging from 2.1 to 10.3 meV. These $\vec{Q}$-E patterns with Re present are very similar to those observed in the pure material [210]. The FWHM in H at 10 meV is anomalously large because of an overlap with spin cones emanating from (1 0 0) and phonons from (2 0 0), but the low-energy correlation width is accurate. The intensity and peak energy of the excitations have decreased from the parent material, but their $\vec{Q}$-width and hence their dynamic spin correlation lengths remain unchanged. Those incommensurate fluctuations that are not a primary signature of hidden order are barely affected by doping or temperature. So the predominant behaviour that survives the approach to the quantum critical point is the robust cone of gapped, incommensurate fluctuations, similar to the parent material.

5.3 Measurements of URu_2Si_2 Under Hydrostatic Pressure

Measurements were performed in three temperature- and pressure-driven phases of URu_2Si_2. These are the paramagnetic (P = 0, T = 25 K), hidden order (P = 0, T = 2 K) and antiferromagnetic (P = 10.1 kbar, T = 4 K) phases. The inelastic neutron scattering measurements are shown in Fig. 5.7.

To normalize the data between the paramagnetic and hidden order phases, the phonon at (2 0 0) was used. Since the sample environment is different when being measured under pressure, a more complicated procedure was necessary to normalize the data in the antiferromagnetic phase. The background was

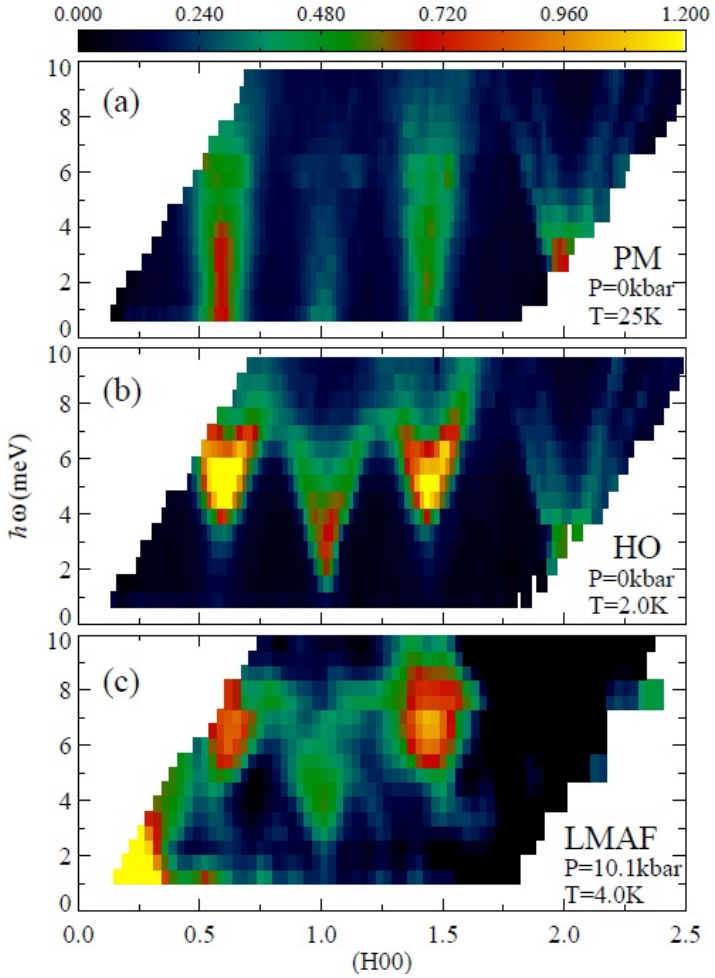

Figure 5.7: The scattering intensity as a function of energy and scattering vector along (H 0 0) in the three phases studied: (a) at ambient pressure and 25 K, in the paramagnetic phase. The phonon at (2 0 0) is visible, as are the excitations at the incommensurate (1.4 0 0) wave vector. (b) at ambient pressure and 2 K, in the hidden order regime. The phonon is present with equal intensity, while the excitations at (1.4 0 0) have become gapped, and more slowly dispersing. The commensurate excitation at (1 0 0) is also present. (c) at 10.1 kbar and 4 K, in the antiferromagnetic phase. The scattering here looks qualitatively similar to the spectrum in the hidden order phase, with some additional intensity at the commensurate point. Figure taken from [205].

first removed by subtracting a measurement of a piece of Al occupying the same volume as the sample and pressurized to 10.1 kbar. Then the data was normalized to the intensity in the hidden order phase by comparing the (1 0 0) elastic peak. This yields an approximate transmission of the pressure cell of 18% and a transmission of the He of approximately 1%. This is an inexact method, producing a normalization that is only valid within ∼50%, but it does provide relatively good agreement with the hidden order phase and with previous measurements in the antiferromagnetic phase [211]. The data has also been corrected for the higher-order perturbation of the monitor.

The paramagnetic phase shows nearly absent commensurate excitations, as well as incommensurate correlations that are gapless and strongly dispersing. Upon entering the hidden order phase, the commensurate excitations are much stronger, as are the incommensurate features. The incommensurate excitations have also become gapped. The antiferromagnetic phase looks qualitatively similar to the hidden order phase, with strong commensurate and incommensurate excitations with a spin gap present at the incommensurate wave vector. The spin gap appears to have increased in the antiferromagnetic phase compared to the hidden order phase. In the antiferromagnetic phase, there is elastic magnetic scattering present at (1 0 0), arising from the static magnetic ordering in this phase. Thus, the excitation at (1 0 0) is expected, in contrast to other measurements that have not observed this feature [208].

The phases can also be compared qualitatively by using constant E slices in the (H 0 L) plane, as shown in Fig. 5.8. These slices were constructed by integrating ±0.5 meV around 2, 5, 8 and 11 meV (shown clockwise from top

left) and folding the data into the H,K > 0 quadrant, allowed by the tetragonal symmetry of the crystal. In agreement with the observations in Fig. 5.7, the incommensurate excitations are present in all three phases, albeit are much stronger in the hidden order and antiferromagnetic phases. The commensurate excitations are only present in the hidden order and antiferromagnetic phases. Comparing these two phases, we see that the spin gap is larger in the antiferromagnetic phase. This is seen in the 5 meV slices, where all of the excitations are observed in the hidden order phase but the incommensurate features are not seen at 5 meV in the antiferromagnetic phase, due to this shift. Furthermore, the 8 meV slice shows the overlap of the two excitations in the hidden order phase, while they still appear separated in $\vec{Q}$ in the antiferromagnetic 8 meV slice.

To quantify these measurements, cuts of the data through the wave vectors (1 0 0) and (1.4 0 0) in each of the three phases are shown in Fig. 5.9. Following the analysis in Ref. [115], the data in each phase was fit to a spin wave model for interacting singlets, given by Eq. 5.3:

$$I(\vec{Q}^*, \omega) = \frac{A}{\omega_{\vec{Q}^*}} \cdot \left[\frac{1}{(\omega - \omega_{\vec{Q}^*})^2 + \gamma^2} - \frac{1}{(\omega + \omega_{\vec{Q}^*})^2 + \gamma^2} \right] \tag{5.3}$$

where A is the Intensity and γ is the FWHM width of the peak. The gap energy, Δ, is contained in the term $\omega_{\vec{Q}^\star}$, given by:

$$\omega_{\vec{Q}} = \sqrt{\Delta^2 + v_H^2(H - H_0)^2 + v_K^2(K - K_0)^2 + v_L^2(L - L_0)^2} \tag{5.4}$$

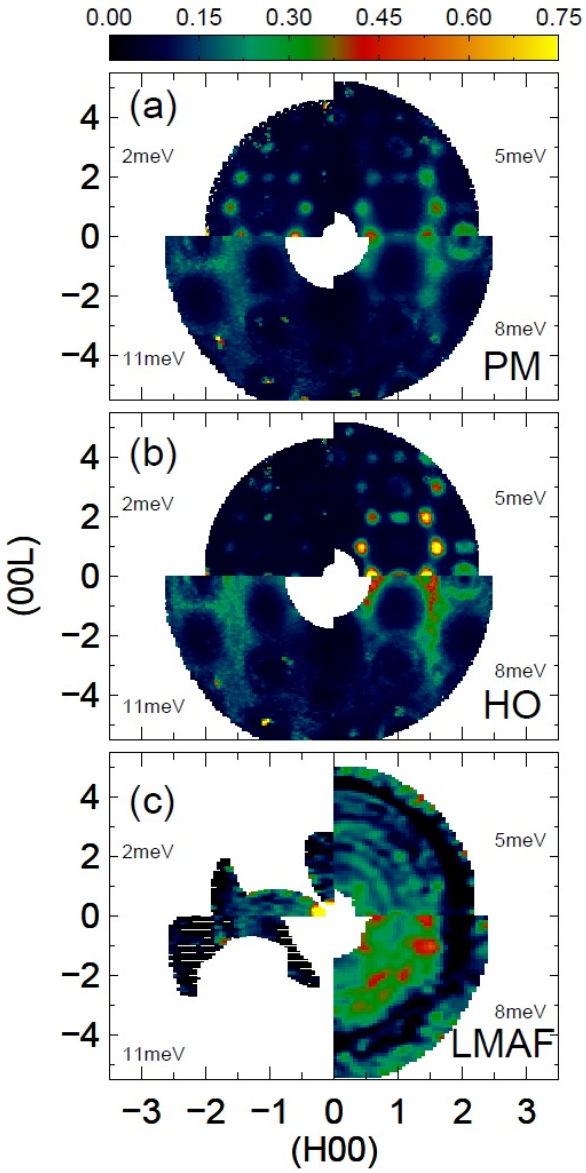

Figure 5.8: Constant energy slices in the (H 0 L) plane in each of the three phases. Energies shown are 2, 5, 8 and 11 meV (clockwise from top left). The range of integration of energy for the slices was ±0.5 meV. Figure taken from [205].

This was multiplied by a Bose factor, and convoluted with the 4D instrumental resolution function using RESLIB [171]. Using data taken from [115], the required spin velocities were taken to be: $v_H = 56.30$, $v_K = 36.61$ and $v_L = 19.97$ meV/r.l.u. around $\vec{Q} = (1.4\ 0\ 0)$ and $v_H = 48.64$, $v_K = 63.78$ and $v_L = 27.50$ meV/r.l.u. around $\vec{Q} = (1\ 0\ 0)$.

The results of this fitting are given in Table 5.1. In agreement with previous measurements of the commensurate spin excitations [115, 127, 208], a peak around 2.26(1) meV was found. Surprisingly, this peak is unaffected by the transition to the hidden order phase. The incommensurate gap is affected by the transition to antiferromagnetism, with a gap that increases by $\sim$30%. While this may be due to the strengthening of the hidden order and an increase in T_0, the increase in the gap is proportionally larger than the increase in T_0. It is also worth noting that the $\vec{Q}$-width of the excitations in the antiferromagnetic phase is similar to that of the hidden order phase. This qualitative similarity is supported by transport and thermodynamic measurements that find Fermi surface reconstruction when passing from the paramagnetic to the hidden order phase [92, 93]. In contrast, there is no significant Fermi surface reconstruction across the hidden order-antiferromagnetic phase boundary [143, 127].

5.4 Conclusions

The neutron scattering measurements in this Chapter have focused on the excitations present in the hidden order phase, and their response to two per-

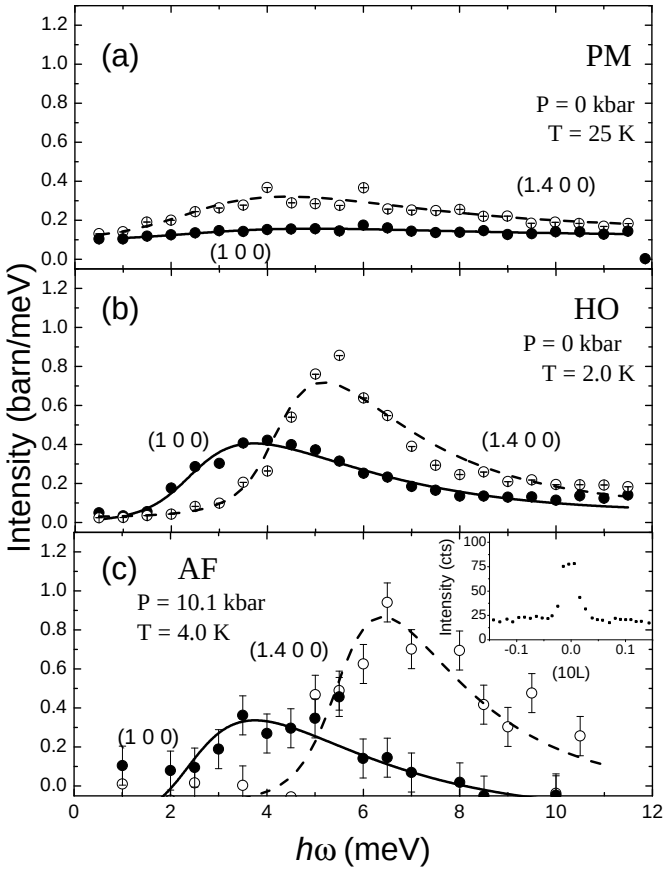

Figure 5.9: The energy-dependence of the scattering intensity at the commensurate (filled circles) and incommensurate (open circles) wave vectors in each phase. The lines are fits to the data as described in the text. (a) In the paramagnetic phase, no scattering is seen at the commensurate point, while a weak signal is seen at the incommensurate point. (b) In the hidden order phase, the scattering is much more intense at both wave vectors while opening a spin gap at (1.4 0 0). (c) In the antiferromagnetic phase, both peaks are still present. The incommensurate peak seems to have shifted to slightly higher energies. (inset) The scattering along (1 0 L) in the antiferromagnetic phase shows the substantially more intense peak at (1 0 0), arising from the large, ordered antiferromagnetic moment. Figure taken from [205].

turbations: chemical pressure through Re doping and the application of hydrostatic pressure.

Phase	$\vec{Q}$	Intensity	Δ (meV)	γ (meV)
PM	(1 0 0)	7.69(13)	2.32(3)	2.41(2)
PM	(1.4 0 0)	16.69(15)	2.23(1)	1.75(1)
HO	(1 0 0)	12.38(3)	2.26(1)	0.91(1)
HO	(1.4 0 0)	10.60(2)	4.15(1)	0.65(1)
AF	(1 0 0)	17.23(69)	2.27(2)	0.93(2)
AF	(1.4 0 0)	13.3(2.5)	5.50(1)	0.68(1)

Table 5.1: Results of fitting the data in Fig. 5.9 to the dispersion described in Eq. 5.3. Data taken from [205].

When doped with 5% Re, the commensurate spin fluctuations lose much of their collective peaking as nesting is disturbed. The lifetime of these spin fluctuations, or more likely the fermions from which they arise, is shorter in the Re-doped compound compared to the parent material. However, the spin gap that is present in the parent material is also present under this chemical doping. Though weakened, it indicates that the hidden order phase survives at least halfway to the quantum critical point to ferromagnetism. This is a contrasting case to Rh doping, where the hidden order phase is destroyed as the antiferromagnetic phase is enhanced.

When hydrostatic pressure greater than 6 kbar is applied, there is a phase transition to an antiferromagnetic phase. As described above, the spin correlations within the antiferromagnetic phase are qualitatively similar to those of the hidden order phase. This extends to the gapped nature of the incommensurate feature as well as the $\vec{Q}$-width of the excitations. The qualitative similarities suggest that the hidden order phase is closely related to the conventional antiferromagnetic phase that arises with the application of hydrostatic pressure. The main difference that is observed between the two phases in an

increase in the magnitude of the gap at $\vec{Q} = (1.4\ 0\ 0)$. This may be a result of the strengthening of the hidden order phase that occurs with the application of hydrostatic pressure [212]. This trend continues as the antiferromagnetic phase takes over.

Together, these two sets of measurements display the robust properties of the spin correlations present in the hidden order phase. With perturbations caused by the application of chemical and hydrostatic pressure, the excitations survive as the system approaches (in the case of Re-doping) or even enters (with hydrostatic pressure) a more conventional magnetic state. This suggests an intimate relationship between conventional magnetism and the hidden order phase in URu_2Si_2.

Chapter 6

Conclusions

6.1 $Ba(Fe_{1-x}Co_x)_2As_2$ and $Sr(Fe_{0.87}Co_{0.13})_2As_2$

Muon spin relaxation/rotation/resonance (μSR) was used to measure several single crystals of the series $Ba(Fe_{2-x}Co_x)_2As_2$ with Cobalt concentrations $x = 0.038$, 0.047, 0.061, 0.074, 0.107 and 0.114. A single crystal of $Sr(Fe_{0.87}Co_{0.13})_2As_2$ was also measured. The two samples with the lowest doping, $x = 0.038$ and $x = 0.047$, showed strong $\hat{c}$-axis magnetism occurring below T_{SDW}. The magnetic properties, such as the size of the local field and the magnetic volume fraction, do not change below the superconducting transition. The measurements suggest that the local magnetic field is increasingly disordered as the concentration of Co increases. These samples were shown to exhibit both superconductivity and magnetism, but that the entire samples sees magnetism means that superconductivity exists in or near regions of strong magnetic order.

The remaining compounds (with $x = 0.061$, 0.074, 0.107, 0.114 and $Sr(Fe_{0.87}Co_{0.13})_2As_2$) were measured with ZF-$\mu$SR and no magnetic ordering

was found down to T = 1.65 K. An analytic Ginzburg-Landau model was used to fit the data and obtain absolute values for the penetration depth, λ. A model for the temperature dependence of the superfluid density, $n_s \propto 1/\lambda^2$, based on two s-wave gaps describes the data well. The superfluid density varies roughly quadratically with the superconducting transition temperature, T_{SC}. Below T_{SC}, a paramagnetic frequency shift was observed indicative of field-induced magnetism along the $\hat{c}$ crystallographic direction.

These measurements represent one of the first measurements of the penetration depth in the iron pnictide superconductors. The values of the gaps obtained from fitting this data have been confirmed using other techniques, as well as by theoretical calculations. The μSR techniques described here have been used in other pnictide compounds and have proven effective in measuring magnetic properties of these compounds in the superconducting state.

6.2 $URu_{1.9}Re_{0.1}Si_2$ and URu_2Si_2

Measurements of URu_2Si_2 under chemical and hydrostatic pressure focused on measuring the spin correlations that are present in the hidden order phase.

The chemical pressure that is induced by 5% Re doping perturbs, but does not destroy, the commensurate spin excitations. The commensurate spin fluctuations lose much of their collective peaking, indicating that the lifetime of the fermions that give rise to them is shorter in the Re-doped compound compared to the parent material. The spin gap that is present in the parent material is also present under this chemical doping. The hidden order phase

survives at least halfway to the quantum critical point to ferromagnetism, but is weakened by the Re substitution.

Under hydrostatic pressure of 10.1 kbar, the spin correlations are found to be qualitatively similar to those of the hidden order phase. The $\vec{Q}$-width of the excitations and their gapped nature remains unchanged upon entering the antiferromagnetic phase. Quantitatively, there is an increase in the magnitude of the gap at $\vec{Q} = (1.4\ 0\ 0)$. This may be a result of the increase in the transition temperature preceding the onset of the antiferromagnetic phase.

These studies find that the spin correlations present in the hidden order phase are fairly robust against perturbations. This suggests an intimate relationship between conventional magnetism and the hidden order phase. As work continues into the nature of the broken symmetry in this phase, this work may lead to avenues of exploration related to more conventional magnetic states.

Future work for this compound may involve measurements at other pressures, allowing for a study of the excitations more completely across the hidden order-antiferromagnetic phase transition. Similarly to what has been done with previous measurements [208], it may be possible to do this at a pressure where both the hidden order and antiferromagnetic phase are accessible by varying temperature.

Bibliography

[1] H.K. Onnes. *Leiden Comm.* **120b:122b:124c** (1911).

[2] W. Meissner and R. Ochsenfeld. *Naturwissenschaften.* **21** (1933) 787.

[3] J. Bardeen, L.N. Cooper, and J.R. Schrieffer. *Phys. Rev.* **106** (1957) 162.

[4] A.A. Abrikosov. *Sov. Phys. JETP.* **5** (1957) 1174.

[5] N.W. Ashcroft and USA. (1976). N.D. Mermin. Solid State Physics. Harcourt Inc. Orlando, FL.

[6] USA. (1996). M. Tinkham. Introduction to Superconductivity. 2^{nd} Ed. Dover Publications Inc. Mineola, NY.

[7] USA. (1999). P.G. de Gennes. Superconductivity of Metals and Alloys. Westview Press. Boulder, CO.

[8] USA. (2005). C. Kittel. Introduction to Solid State Physics. 8^{th} Ed. John Wiley & Sons Inc. Hoboken, NJ.

[9] P. Townsend and J. Sutton. *Phys. Rev.* **128** (1962) 591.

[10] F. London and H. London. *Proc. R. Soc. London, Ser. A.* **149** (1935) 71.

[11] V.L. Ginzburg and L.D. Landau. *Zh. Eksp. Teor. Fiz.* **20** (1950) 1064.

[12] J.G. Bednorz and K.A. Müller. *Z. Physik B.* **64** (1986) 189.

[13] J. Orenstein and A.J. Millis. *Science.* **288** (2000) 468.

[14] T. Imai, T. Shimizu, T. Tsuda, H. Yasuoka, T. Takabatake, Y. Nakazawa, and M. Ishikawa. *J. Phys. Soc. Jpn.* **57** (1988) 1771.

[15] W.N. Hardy, D.A. Bonn, D.C. Morgan, R. Liang, and K. Zhang. *Phys. Rev. Lett.* **70** (1993) 3999.

[16] J.E. Sonier, R.F. Kiefl, J.H. Brewer, D.A. Bonn, J.F. Carolan, K.H. Chow, P. Dosanjh, W.N. Hardy, Ruixang Liang, W.A. MacFarlane, P. Mendels, G.D. Morris, T.M. Riseman, and J.W. Schneider. *Phys. Rev. Lett.* **72** (1994) 744.

[17] J.R. Kirtley, C.C. Tsuei, J.Z. Sun, C.C. Chi, L.S. Yu-Jahnes, A. Gupta, M. Rupp, and M.B. Ketchen. *Nature.* **373** (1995) 225.

[18] D.A. Wollman, D.J. van Harlingen, W.C. Lee, D.M. Ginsberg, and A.J. Leggett. *Phys. Rev. Lett.* **71** (1993) 2134.

[19] C.C. Tsuei, J.R. Kirtley, C.C. Chi, L.S. Yu-Jahnes, A. Gupta, T. Shaw, J.Z. Sun, and M.B. Ketchen. *Phys. Rev. Lett.* **73** (1994) 593.

[20] C.C. Tsuei, J.R. Kirtley, M. Rupp, J.Z. Sun, A. Gupta, M.B. Ketchen, C.A. Wang, Z.F. Ren, J.H. Wang, and M. Bhushan. *Science.* **271** (1996) 329.

[21] M.R. Norman and C. Pepin. *Rep. Prog. Phys.* **66** (2003) 1547.

[22] Y.J. Uemura, G.M. Luke, B.J. Sternlieb, J.H. Brewer, J.F. Carolan, W.N. Hardy, R. Kadono, J.R. Kempton, R.F. Kiefl, S.R. Kreitzman,

P. Mulhern, T.M. Riseman, D.Ll. Williams, B.X. Yang, S. Uchida, H. Takagi, J. Goplalakrishnan, A.W. Sleight, M.A. Subramanian, C.L. Chien, M.Z. Ceiplak, Gang Xiao, V.Y. Lee, B.W. Statt, C.E. Stronach, W.J. Kossler, and X.H. Yu. *Phys. Rev. Lett.* **62** (1989) 2317.

[23] K. Yamada, C.H. Lee, K. Kurahashi, J. Wada, S. Wakimoto, S. Ueki, H. Kimura, Y. Endoh, S. Hosoya, G. Shirane, R.J. Birgeneau, M. Greven, M.A. Kastner, and Y.J. Kim. *Phys. Rev. B.* **57** (1998) 6165.

[24] V.J. Emery, S.A. Kivelson, and O. Zachar. *Phys. Rev. B.* **56** (1997) 6120.

[25] D.J. Scalapino. *Rev. Mod. Phys.* **84** (2012) 1383.

[26] H. Takahashi, K. Igawa, K. Arii, Y. Kamihara, M. Hirano, and H. Hosono. *Nature.* **453** (2008) 376.

[27] M.D. Lumsden and A.D. Christianson. *J. Phys. Condens. Matter.* **22** (2010) 203203.

[28] P.C. Canfield and S.L. Bud'ko. *Ann. Rev. Condens. Matter Phys.* **1** (2010) 27.

[29] J.-Q. Yan, A. Kreyssig, S. Nandi, N. Ni, S.L. Bud'ko, A. Kratcher, R.J. McQueeney, R.W. McCallum, T.A. Lograsso, A.I. Goldman, and P.C. Canfield. *Phys. Rev. B.* **78** (2008) 024516.

[30] G.F. Chen, Z. Li, J. Dong, G. Li, W.Z. Hu, X.D. Zhang, X.H. song, P. Zheng, N.L. Wang, and J.L. Luo. *Phys. Rev. B.* **78** (2008) 224512.

[31] N. Ni, S. Nandi, A. Kreyssig, A.I. Goldman, E.D. Mun, S.L. Bud'ko, and P.C. Canfield. *Phys. Rev. B.* **78** (2008) 014523.

[32] F. Ronning, T. Klimczuk, E.D. Bauer, H. Volz, and J.D. Thompson. *J. Phys.: Condens. Matter.* **20** (2008) 322201.

[33] M. Rotter, M. Tegel, M. Johrengt, I. Schellenberg, W. Hermes, and R. Pöttgen. *Phys. Rev. B.* **78** (2008) 020503.

[34] A.I Goldman, D.N. Argyriou, B. Ouladdiaf, T. Chatterji, A. Kreyssig, S. Nandi, N. Ni, S.L. Bud'ko, P.C. Canfield, and R.J. McQueeney. *Phys. Rev. B.* **78** (2008) 100506(R).

[35] P.C. Canfield, S.L. Bud'ko, N. Ni, A. Kreyssig, A.I. Goldman, R.J. McQueeney, M.S. Torikachvili, D.N. Argyriou, G. Luke, and W. Yu. *Physica C.* **469** (2009) 404.

[36] J.M. Tarascon, L.H. Greene, P. Barboux, W.R. McKinnon, G.W. Hull, T.P. Orlando, K.A. Delin, S. Foner, and E.J. McNiff Jr. *Phys. Rev. B.* **36** (1987) 8393.

[37] G. Xiao, M.Z. Cieplak, D. Musser, A. Gavrin, F.H. Streitz, C.L. Chien, J.J. Rhyne, and J.A. Gotaas. *Nature.* **332** (1988) 238.

[38] N. Ni, M.E. Tillman, J.-Q. Yan, A. Kratcher, S.T. Hannahs, S.L. Bud'ko, and P.C. Canfield. *Phys. Rev. B.* **78** (2008) 214515.

[39] A.S. Sefat, R. Jin, M.A. McGuire, B.C. Sales, D.J. Singh, and D. Mandrus. *Phys. Rev. Lett.* **101** (2009) 117004.

[40] F. Ning, K. Ahilan, T. Imai, A.S. Sefat, R. Jin, M.A. McGuire, B.C. Sales, and D. Mandrus. *J. Phys. Soc. Jpn.* **78** (2009) 013711.

[41] J.-H. Chu, C. Kucharczyk J.G. Analytis, and I.R. Fisher. *Phys. Rev. B.* **79** (2009) 014506.

[42] R.M. Fernandes, A.V. Chubukov, J. Knolle, I. Eremin, and J. Schmalian. *Phys. Rev. B.* **85** (2012) 024534.

[43] L.W. Harringer, H.Q. Luo, M.S. Liu, C. Frost, J.P. Hu, M.R. Norman, and Pengcheng Dai. *Phys. Rev. B.* **84** (2011) 054544.

[44] E.D. Mun, S.L. Bud'ko, N. Ni, A.N. Thaler, and P.C. Canfield. *Phys. Rev. B.* **80** (2009) 054517.

[45] F. Rullier-Albenque, D. Colson, A. Forget, and H. Alloul. *Phys. Rev. Lett.* **103** (2009) 057001.

[46] L. Fang, H. Luo, P. Cheng, Z. Wang, Y. Jia, G. Mu, B. Shen, I.I. Mazin, L. Shan, C. Ren, and H.-H. Wen. *Phys. Rev. B.* **80** (2009) 140508.

[47] L.J. Li, Y.K. Luo, Q.B. Wang, H. Chen, Z. Ren, Q. Tao, Y.K. Li, X. Lin, M. He, Z.W. Zhu, G.H. Cao, and Z.A. Xu. *New J. Phys.* **11** (2009) 025008.

[48] C. Liu, T. Kondo, R.M. Fernandes, A.D. Palczewski, E.D. Mun, N. Ni, A.N. Thaler, A. Bostwick, E. Rotenberg, J. Schmalian, S.L. Bud'ko, P.C. Canfield, and A. Kaminski. *Nat. Phys.* **6** (2010) 419.

[49] N. Stojilovic, A. Koncz, L.W. Kohlman, R. Hu, C. Petrovic, and S.V. Dordevic. *Phys. Rev. B.* **81** (2010) 174518.

[50] D. Nakamura, Y. Imai, A. Maeda, T. Katase, H. Hiramatsu, and H. Hosono. (2009) *arXiv/cond-mat:*0912.4351v3.

[51] J. Dai, Q. Si, J.-X. Zhu, and E. Abrahams. *Proc. Nat. Acad. Sci. USA.* **106** (2009) 4118.

[52] Q. Si, E. Abrahams, J. Dai, and J.-X. Zhu. *New J. Phys.* **11** (2009) 045001.

[53] D.C. Johnston. *Adv. in Phys.* **59** (2010) 803.

[54] T. Imai, K. Ahilan, F. Ning, M.A. McGuire, A.S. Sefat, R. Jin, B.C. Sales, and Suppl. C. (2008) 47. D. Mandrus. *J. Phys. Soc. Jpn.* **77**.

[55] D.S. Inosov, J.T. Park, P. Bourges, D.L. Sun, Y. Sidis, A. Schneiderwind, K. Hradil, D. Haug, C.T. Lin, B. Keimer, and V. Hinkov. *Nat. Phys.* **6** (2010) 178.

[56] D. Parshall, K.A¿ Lokshin, J. Niedziela, A.D. Christianson, M.D. Lumsden, H.A. Mook, S.E. Nagler, M.A. McGuire, M.B. Stone, D.L. Abernathy, A.S. Sefat, B.C. Sales, D.G. Mandrus, and T. Egami. *Phys. Rev. B.* **80** (2009) 012502.

[57] M.D. Lumsden, A.D. Christianson, D. Parshall, M.B. Stone, S.E. Nagler, G.J. MacDougall, H.A. Mook, K. Lokshin, T. Egami, D.L. Abernathy, E.A. Goremychkin, R. Osborn, M.A. McGuire, A.S. Sefat, R. Jin, B.C. Sales, and D. Mandrus. *Phys. Rev. Lett.* **102** (2009) 107005.

[58] A.D. Christianson, M.D. Lumsden, S.E. Nagler, G.J. MacDougall, M.A. McGuire, A.S. Sefat, R. Jin, B.C. Sales, and D. Mandrus. *Phys. Rev. Lett.* **103** (2009) 087002.

[59] D.K. Pratt, A. Kreyssig, S. Nandi, N. Ni, A. Thaler, M.D. Lumsden, W. Tian, J.L. Zarestky, S.L. Bud'ko, P.C. Canfield, A.I. Goldman, and R.J. McQueeney. *Phys. Rev. B.* **81** (2010) 140510(R).

[60] D.K. Pratt, M.G. Kim, A. Kreyssig, Y.B. Lee, G.S. Tucker, A. Thaler, W. Tian, J.L Zarestky, S.L. Bud'koi, P.C. Canfield, B.N. Harmon, A.I. Goldman, and R.J. McQueeney. *Phys. Rev. Lett.* **106** (2011) 257001.

[61] Y. Laplace, J. Bobroff, F. Rullier-Albenque, D. Colson, and A. Forget. *Phys. Rev. B.* **80** (2009) 140510.

[62] P. Bonville, F. Rullier-Albenque, D. Colson, and A. Forget. *Europhys. Lett.* **89** (2010) 67008.

[63] P.J. Hirschfeld, M.M. Korshunov, and I.I. Mazin. *Rep. Prog. Phys.* **74** (2011) 124508.

[64] A. Chubukov. *Ann. Rev. Condens. Matter Phys.* **3** (2011) 57.

[65] I.I. Mazin and J. Schmalian. *Physica C.* **469** (2009) 614.

[66] I.I. Mazin, D.J. Singh, M.D. Johannes, and M.-H. Du. *Phys. Rev. Lett.* **101** (2008) 057003.

[67] Y.S. Oh, Y. Liu, L.Q. Yan, K.H. Kim, R.L. Greene, and I. Takeuchi. *Phys. Rev. Lett.* **102** (2009) 147002.

[68] C.W. Hicks, T.M. Lippman, M.E. Huber, Z.A. Ren, J. Yang, Z.X. Zhao, and K.A. Moler. *J. Phys. Soc. Jpn.* **78** (2009) 013708.

[69] T.A. Maier and D.J. Scalapino. *Phys. Rev. B.* **78** (2008) 020514(R).

[70] T.A. Maier, S. Grasser, D.J. Scalapino, and P.J. Hirschfeld. *Phys. Rev. B.* **79** (2009) 134520.

[71] D. Parker and I.I Mazin. *Phys. Rev. Lett.* **102** (2009) 227007.

[72] C.-T. Chen, C.C Tsuei, M.B. Ketchen, Z.-A. Ren, and Z.X. Zhao. *Nat. Phys.* **6** (2010) 260.

[73] L. Capriotti, R.D. Sedgewick, and D.J. Scalapino. *Phys. Rev. B.* **68** (2002) 14508.

[74] L. Zhu, W.A. Atkinson, and P.J. Hirschfeld. *Phys. Rev. B.* **69** (2004) 060503.

[75] Z. Fisk, D.W. Hess, C.J. Penthick, D. Pines, J.L. Smith, J.D. Thompson, and J.O. Willis. *Science.* **239** (1988) 33.

[76] K. Kadowaki and S.B. Woods. *Solid State Comm.* **58** (1986) 507.

[77] Z. Fisk, H.R. Ott, T.M. Rice, and J.L. Smith. *Nature.* **320** (1986) 124.

[78] G.R. Stewart. *Rev. Mod. Phys.* **56** (1984) 755.

[79] A. Wasserman, M. Springford, and A.C. Hewson. *J. Phys.: Condens. Matter.* **1** (1989) 2669.

[80] M.A. Ruderman and C. Kittel. *Phys. Rev.* **96** (1954) 99.

[81] T. Kasuya. *Prog. Theor. Phys.* **16** (1956) 45.

[82] K. Yosida. *Phys. Rev.* **106** (1957) 893.

[83] J. Kondo. *Prog. Theor. Phys. Jpn.* **32** (1964) 37.

[84] R.H. Heffner and M. Norman. arXiv/cond-mat:9506043 (1995).

[85] C.J. Penthick and 1987. p. 201. D. Pines. Novel Superconductivity. Plenum Press, New York.

[86] S. Doniach. *Physica B.* **91** (1977) 213.

[87] S. Kambe, H. Sakai, Y. Tokunaga, T. Fujimoto, H. Kato, R.E. Walstedt, S. Ikeda, T.D. Matsuda, Y. Haga, and Y. Onuki. *J. Phys. Soc. Jpn.* **75** (2006) 127.

[88] S. Kondo, D.C. Johnston, C.A. Swenson, F. Borsa, A.V. Mahajan, L.L. Miller, T. Gu, A.I. Goldman, M.B. Maple, D.A. Gajewski, E.J. Freeman, N.R. Dilley, R.P. Dickey, J. Merrin, K. Kojima, G.M. Luke, Y.J. Uemura, O. Chmaissem, and J.D. Jorgensen. *Phys. Rev. Lett.* **78** (1997) 3729.

[89] 1970. H.H. Hill. Plutonium and Other Actinides. AIME, New York.

[90] G. Just and P. Paufler. *J. All. Comp.* **232** (1996) 1.

[91] W. Schlabitz, J. Baumann, R. Pollit, U. Rauchschwalbe, H.M. Mayer, U. Ahlheim, and C.D. Bredl. *Z. Phys. B* **62** (1986) 171.

[92] T.T.M. Palstra, A.A. Menovsky, J. van den Berg, A.J. Dirkmaat, P.H. Kes, G.J. Nieuwenhuys, and J.A. Mydosh. *Phys. Rev. Lett.* **55** (1985) 2727.

[93] M.B. Maple, J.W. Chen, Y. Dalichaouch, T. Kohara, C. Rossel, M.S. Torikachvili, M.W. McElfresh, and J.D. Thompson. *Phys. Rev. Lett.* **56** (1986) 185.

[94] T.T.M. Palstra, A.A. Menovsky, and J.A. Mydosh. *Phys. Rev. B.* **33** (1986) 6527(R).

[95] J.A. Mydosh and P.M. Oppeneer. *Rev. Mod. Phys.* **83** (2011) 1301.

[96] C. Broholm, J.K. Kjems, W.J.L. Buyers, P. Matthews, T.T.M. Palstra, A.A. Menovsky, and J.A. Mydosh. *Phys. Rev. Lett.* **68** (1987) 1467.

[97] E.D. Isaacs, D.B. McWhan, R.N. Kleiman, D.J. Bishop, G.E. Ice, P. Zschack, B.D. Gaulin, T.E. Mason, J.D. Garrett, and W.J.L. Buyers. *Phys. Rev. Lett.* **65** (1990) 3185.

[98] H. Harima, K. Miyake, and J. Flouquet. *J. Phys. Soc. Jpn.* **79** (2010) 033705.

[99] H. Kusunose and H. Harima. *J. Phys. Soc. Jpn.* **80** (2011) 084702.

[100] A.I. Tóth and G. Kotliar. *Phys. Rev. Lett.* **107** (2011) 266405.

[101] J.-J. Su, Y. Dubi, P. Woelfle, and A.V. Balatsky. *J. Phys.: Condens. Matt.* **23** (2011) 094214.

[102] J. Rau and H.-Y. Kee. *Phys. Rev. B.* **85** (2012) 245112.

[103] C. Pépin, M.R. Norman, S. Burdin, and A. Ferraz. *Phys. Rev. Lett.* **106** (2011) 106601.

[104] C. Thomas, S. Burdin, C. Pépin, and A. Ferraz. *Phys. Rev. B.* **87** (2013) 014422.

[105] S. Fujimoto. *Phys. Rev. Lett.* **106** (2011) 196407.

[106] H. Ikeda, M.-T. Suzuki, R. Arita, T. Takimoto, T. Shibauchi, and Y. Matsuda. *Nat. Phys.* **8** (2012) 528.

[107] A.V. Balatsky, A. Chantis, H.P. Dahal, D. Parker, and J.X. Zhu. *Phys. Rev. B.* **79** (2009) 214413.

[108] T. Das. *Sci. Rep.* **2** (2012) 596.

[109] Y. Dubi and A.V. Balatsky. *Phys. Rev. Lett.* **106** (2011) 086401.

[110] P.M. Oppeneer, S. Elgazzar, J. Rusz, Q. Feng, T. Durakiewicz, and J.A. Mydosh. *Phys. Rev. B.* **84** (2011) 241102(R).

[111] P. Chandra, P. Coleman, and R. Flint. *Nature.* **493** (2013) 621.

[112] J. Schoenes, C. Schönenberger, J.J.M. Franse, and A.A. Menovsky. *Phys. Rev. B.* **35** (1987) 5375.

[113] A. de Visser, F.E. Kayzel, A.A. Menovsky, J.J.M. Franse, J. van den Berg, and G.J. Niewenhuys. *Phys. Rev. B.* **34** (1986) 8168.

[114] T.E. Mason, B.D. Gaulin, J.D. Garrett, Z. Tun, W.J.L. Buyers, and E.D. Isaacs. *Phys. Rev. Lett.* **65** (1990) 3189.

[115] C. Broholm, H. Lin, P.T. Matthews, T.E. Mason, W.J.L. Buyers, M.F. Collins, A.A. Menovsky, J.A. Mydosh, and J.K. Kjems. *Phys. Rev. B.* **43** (1991) 12809.

[116] D.E. MacLaughlin, D.W. Cooke, R.H. Heffner, R.L. Hutson, M.W. McElfresh, M.E. Schillaci, H.D. Rempp, J.L. Smith, J.O. Willis,

E. Zirngiebl, C. Boekema, R.L. Lichti, and J. Oostens. *Phys. Rev. B.* **37** (1988) 3153.

[117] G.M. Luke, A. Keren, L.P. Le, Y.J. Uemure, W.D. Wu, D. Bonn, L. Taillefer, J.D. Garrett, and Y. Onuki. *Hyperfine Interact.* **85** (1994) 397.

[118] A. Amato, M.J. Graf, A. de Visser, H. Amitsuka, D. Andreica, and A. Schenck. *J. Phys.: Condens. Matter.* **16** (2004) S4403.

[119] K. Matsuda, Y. Kohori, T. Kohara, E.K. Kuwahara, and H. Amitsuka. *Phys. Rev. Lett.* **87** (2001) 087203.

[120] C.R. Wiebe, G.M. Luke, Z. Yamani, A.A. Menovsky, and W.J.L. Buyers. *Phys. Rev. B.* **69** (2004) 132418.

[121] C.R. Wiebe, J.A. Janik, G.J. MacDougall, G.M. Luke, J.D. Garrett, H.D. Zhou, Y.-J. Jo, L. Balicas, Y. Qiu, J.R.D. Copley, Z. Yamani, and W.J.L. Buyers. *Nature Phys.* **3** (2007) 96.

[122] J.A. Janik, H.D. Zhou, Y.-J. Jo, L. Balicas, G.J. MacDougall, G.M. Luke, J.D. Garett, K.J. McClellan, E.D. Bauer, J.L. Sarrao, Y. Qiu, J.R.D. Copley, Z. Yamani, W.J.L. Buyers, and C.R. Wiebe. *Phys. Rev. B.* **37** (1988) 3153.

[123] W.J.L. Buyers. *Physica B.* **223-224** (196) 9.

[124] H. Ohkuni, Y. Tokiwa, K. Sakurai, R. Settai, T. Haga, E. Yamamoto, Y. Onuki, H. Yamagami, S. Takahashi, and T. Yanagisawa. *Philos. Mag. B.* **79** (1999) 1045.

[125] H. Shishido, K. Hashimoto, T. Shibauchi, T. Sasaki, H. Oizumi, N. Kobayashi, T. Takamasu, K. Takehana, Y. Imanaka, T.D. Matsuda, Y. Haga, Y. Onuki, and Y. Matsuda. *Phys. Rev. Lett.* **102** (2009) 156403.

[126] M.M. Altarawneh, N. Harrison, S.E. Sebatian, L. Balicas, P.H. Tobash, J.D. Thompson, F. Ronning, and E.D. Bauer. *Phys. Rev. Lett.* **106** (2011) 146403.

[127] E Hassinger, G. Knebel, T.D. Matsuda, D. Aoki, V. Taufour, and J. Flouquet. *Phys. Rev. Lett.* **105** (2010) 216409.

[128] Y.S. Oh, K.-H. Kim, P.A. Sharma, N. Harrison, H. Amitsuka, and J.A. Mydosh. *Phys. Rev. Lett.* **98** (2007) 016401.

[129] Y. Kasahara, H. Shishido, T. Shibauchi, Y. Haga, T.D. Matsuda, Y. Onuki, and Y. Matsuda. *New J. Phys.* **11** (2007) 055061.

[130] R. Bel, H. Jin, K. Behnia, J. Flouquet, and P. Lejay. *Phys. Rev. B.* **70** (2004) 220501(R).

[131] D.A. Bonn, J.D. Garrett, and T. Timusk. *Phys. Rev. Lett.* **61** (1988) 1305.

[132] J. Levallois, F. Lévy-Bertrand, M.K. Tran, J.A. Mydosh, Y.-K. Huang, and D. van der Marel. *Phys. Rev. B.* **84** (2011) 184420(R).

[133] A.R. Schmidt, M.H. Hamidian, P. Wahl, F. Meier, A.V. Balatsky, J.D. Garrett, T.J. Williams, G.M. Luke, and J.C. Davis. *Nature.* **465** (2010) 570.

[134] P. Aynajian, E.H. da Silva Neto, C.V. Parker, Y.-K. Huang, A. Pasupathy, J.A. Mydosh, and A. Yazdani. *Proc. Nat. Acad. Sci. U.S.A.* **107** (2010) 10383.

[135] R. Yoshida, Y. Nakamura, M. Fukui, Y. Haga, E. Yamamoto, Y. Onuki, M. Okawa, S. Shin, M. Hirai, Y. Muraoka, and T. Yokoya. *Phys. Rev. B.* **82** (2010) 205108.

[136] G.L. Dakovski, Y. Li, S.M. Gilbertson, G. Rodriguez, A.V. Balatsky, J.-X. Zhu, K. Gofryk, E.D. Bauer, P.H. Tobash, A. Taylor, J.L. Sarrao, P.M. Oppeneer, P.S. Riseborough, J.A. Mydosh, and T. Durakiewicz. *Phys. Rev. B.* **84** (2011) 161103(R).

[137] N.P. Butch and M.B. Maple. *J.Phys.: Condens. Matt.* **22** (2010) 164204.

[138] M.S. Torikachvili, L. Rebelsky, K. Motoya, S.M. Shapiro, Y. Dalichaouch, and M.B. Maple. *Phys. Rev. B.* **45** (1992) 2262.

[139] Y. Kohori, Y. Noguchi, T. Kohara, Y. Dalichaouch, M.A. de la Torre, and M.B. Maple. *Physica B.* **186-188** (1993) 792.

[140] Y. Dalichaouch, M.B. Maple, M.S. Torikachvili, and A.L. Giorgi. *Phys. Rev. B.* **39** (1989) 2423.

[141] St. Thieme, P. Steiner, L. Degiorgi, P. Wachter, Y. Dalichaouch, and M.B. Maple. *Europhys. Lett.* **32** (1995) 367.

[142] N.P. Butch, J.R. Jeffries, S. Chi, J.B. Leao, J.W. Lynn, and M.B. Maple. *Phys. Rev. B.* **82** (2010) 060408(R).

[143] M.W. McElfresh, J.D. Thompson, J.O. Willis, M.B. Maple, T. Kohara, and M.S. Torikachvili. *Phys. Rev. B.* **35** (1987) 43.

[144] J.R. Jeffries, N.P. Butch, T. Yukich, and M.B. Maple. *Phys. Rev. Lett.* **99** (2007) 217207.

[145] J.R. Jeffries, N.P. Butch, T. Yukich, and M.B. Maple. *J. Phys.: Condens. Matter.* **20** (2008) 095225.

[146] G. Motoyama, N. Yokoyama, A. Sumiyama, and Y. Oda. *J. Phys. Soc. Jpn.* **77** (2008) 123710.

[147] H. Amitsuka, M. Sato, N. Metoki, M. Yokoyama, K. Kuwahara, T. Sakakibara, H. Morimoto, S. Kawarazaki, Y. Miyako, and J.A. Mydosh. *Phys. Rev. Lett.* **83** (1999) 5114.

[148] K. Matsuda, Y. Kohori, T. Kohara, H. Amitsuka, K. Kuwahara, and T. Mastumoto. *J. Phys.: Condens. Matter.* **15** (2003) 2363.

[149] M. Nakashima, H. Ohkuni, Y. Inada, R. Setti, Y. Haga, E. Yamamoto, and Y. Onuki. *J. Phys.: Condens. Matter.* **15** (2003) S2011.

[150] A. Villaume, F. Bourdarot, E. Hassinger, S. Raymond, V. Taufour, D. Aoki, and J. Flouquet. *Phys. Rev. B.* **83** (2008) 193102.

[151] N.V. Abrosimov, S.N.Rossolenko, V. Alex, A. Gerhardt, and W. Schöder. *J. Crys. Growth.* **166** (1996) 657.

[152] A. Yaouanc and P. Dalmas de Réotier. Muon Spin Rotation, Relaxation and Resonance: Applications to Condensed Matter. Oxford University Press. New York. (2011).

[153] A. Schenck. Muon Spin Rotation Spectroscopy: Principle and Applications in Solid State Physics. Adam Hilger Ltd. Bristol and Boston. (1985).

[154] G.J. MacDougall. *Ph.D. Thesis*. McMaster University. (2008).

[155] T.J. Williams. *M.Sc. Thesis*. McMaster University. (2009).

[156] S.L. Lee, S.H. Kilcoyne, editors. Scottish Universities Summer School in Physics. Institute of Physics Publishing. Bristol R. Cywinski, and Philadelphia. (1998).

[157] Y.J. Uemura. *D.Sc. Thesis*. The University of Tokyo. (1982).

[158] J.L. Beveridge, J. Doornbos, D.M. Garner, D.J. Arsenau, I.D. Reid, and M. Senba. *Nucl. Instrum. Methods Phys. Res. A.* **240** (1985) 316.

[159] T.M. Riseman. *Ph.D. Thesis*. The University of British Columbia. (1993).

[160] J.E. Sonier, J.H. Brewer, and R.F. Keifl. *Rev. Mod. Phys.* **72** (2000) 769.

[161] E.H. Brandt. *J. Low Temp. Phys.* **73** (1988) 355.

[162] E.M. Forgan, M.T. Wylie, S. Lloyd, M.P. Nutley, S.L. Lee, R. Cubitt, C. Aegerter, H. Keller, and T.W. Li. *Hyperfine Interact.* **105** (1997) 61.

[163] G. Shirane, S.M. Shapiro, and J.M. Tranquada. Neutron Scattering with a Triple-Axis Spectrometer. Cambridge University Press. Cambridge. (2002).

[164] W.L. Bragg. *Proc. Cambridge Phil. Soc.* **17** (1913) 43.

[165] G.L. Squires. Introduction to the Theory of Thermal Neutron Scattering. Cambridge University Press. Cambridge. (1978).

[166] US Department of Energy. http://neutrons.ornl.gov/instruments/. Accessed: 19 August 2013. "ORNL Neutron Sciences Instruments". The Oak Ridge National Lab.

[167] Government of Canada. http://archive.nrc-cnrc.gc.ca/eng/facilities/cnbc/spectrometers.html. Accessed: 28 May 2013. "Neutron Spectrometers Facilities NRC-CNRC". National Research Council.

[168] J.A. Rodriguez, D.M. Adler, P.C. Brand, C. Broholm, J.C. Cook, C. Brocker, R. Hammond, Z. Huang, P. Hundertmark, J.W. Lynn, N.C. Mallszewskyj, J. Moyer, J. Orndorff, D. Pierce, T.D. Pike, G. Scharfstein, S.A. Smee, and R. Vilaseca. *Meas. Sci. Technol.*. **19** (2008) 034023.

[169] M.J. Cooper and R. Nathans. *Acta Cryst.*. **23** (1967) 357.

[170] N.J. Chesser and J.D. Axe. *Acta Cryst.*. **A29** (1972) 160.

[171] TN. (2007). A. Zheludev. *ResLib 3.4*.. Oak Ridge National Laboratory, Oak Ridge.

[172] T.J. Williams, A.A. Aczel, S.L. Bud'ko, P.C. Canfield, J.P. Carlo, T. Goko, N. Ni, Y.J. Uemura, and G.M. Luke. (2013) To be published.

[173] T.J. Williams, A.A. Aczel, E. Baggio-Saitovich, S.L. Bud'ko, P.C. Canfield, J.P. Carlo, T. Goko, J. Munevar, N. Ni, Y.J. Uemura, W. Yu, and G.M. Luke. *Phys. Rev. B.* **80** (2009) 094501.

[174] T.J. Williams, A.A. Aczel, S.L. Bud'ko, P.C. Canfield, J.P. Carlo, T. Goko, N. Ni, S.R. Saha, J. Paglione, Y.J. Uemura, and G.M. Luke. *Phys. Rev. B.* **82** (2010) 094512.

[175] A.A. Aczel, E. Baggio-Saitovich, S.L. Bud'ko, P.C. Canfield, J.P. Carlo, G.F. Chen, Pengcheng Dai, T. Goko, W.Z. Hu, G.M. Luke, J.L. Luo, N. Ni, D.R. Sanchez-Candela, F.F. Tafti, N.L. Wang, T.J. Williams, W. Yu, and Y.J. Uemura. *Phys. Rev. B.* **78** (2008) 214503.

[176] P. Marsik, K.W. Kim, A. Dubroka, M. R ossle, V.K. Malik, L. Shultz, C.N. Wang, Ch. Niedermayer, A.J. Drew, M. Willis, T. Wolf, and C. Bernhard. *Phys. Rev. Lett.* **105** (2010) 057001.

[177] R. De Renzi, P. Bonfà, M. Mazzani, S. Sanna, G. Prando, P. Carretta, R. Khasanov, A. Amato, H. Luetkens, M. Bendele, F. Bernardini, S. Massidda, A. Palenzona, M. Tropeano, and M. Vignolo. *Supercond. Sci. Technol.* **25** (2012) 084009.

[178] K. Prokeš, S. Mat'aš, L. Harnagea, S. Singh, S. Wurmehl, D.N. Argyriou, and B. Büchner. *Phys. Rev. B.* **83** (2011) 104414.

[179] F. Massee, Y.K. Huang, J. Kaas, E. van Heumen, S. de Jong, R. Huisman, H. Luigjes, J.B. Goedkoop, and M.S. Golden. *Europhys. Lett.* **92** (2010) 57012.

[180] J.E. Sonier. *Rep. Prog. Phys.* **70** (2007) 1717.

[181] M.R. Eskildsen, L.Ya. Vinnikov, T.D. Blasius, I.S. Veshchunov, T.M. Artemova, J.M. Densmore, C.D. Dewhurst, N. Ni, A. Kreyssig, S.L.

Bud'ko, P.C. Canfield, and A.I. Goldman. *Phys. Rev. B.* **79** (2009) 100501(R).

[182] T.M. Riseman, J.H. Brewer, K.H. Chow, W.N. Hardy, R.F. Keifl, S.R. Kreitzman, R. Liang, W.A. MacFarlane, P. Mendels, G.D. Morris, J. Rammer, J.W. Schneider, C. Neidermayer, and S.L. Lee. *Phys. Rev B.* **52** (1995) 10569.

[183] J. Nagamutsu, N. Nakagawa, T. Muranaka, Y. Zenitani, and J. Akimitsu. *Nature.* **410** (2001) 63.

[184] A.Y. Liu, I.I. Mazin, and J. Kortus. *Phys. Rev Lett.* **87** (2008) 087005.

[185] T. Kiss T. Yokoya, A. Chainani, S. Shin, M. Nohara, and H. Takagi. *Science.* **294** (2001) 2518.

[186] F.D. Callaghan, M. Laulajainen, C.V. Kaiser, and J.E. Sonier. *Phys. Rev Lett.* **95** (2005) 197001.

[187] F. Bouquet, Y. Wang, R.A. Fisher, D.G. Hinks, J.D. Jorgesen, A. Junod, and N.E. Phillips. *Europhys. Lett.* **56** (2001) 856.

[188] K. Ohishi, T. Muranaka, J. Mkimitsu, A. Koda, W. Higemoto, and R. Kadono. *J. Phys. Soc. Jpn.* **72** (2003) 29.

[189] S. Takeshita and R. Kadono. *New J. Phys.* **11** (2009) 035006.

[190] K. Gofryk, A.S. Sefat, E.D. Bauer, M.A. McGuire, B.C. Sales, D. Mandrus, J.D. Thompson, and F. Ronning. *New J. Phys.* **12** (2010) 023006.

[191] F. Hardy, T. Wolf, R.A. Fisher, R. Eder, P. Schweiss, P. Adelmann, H. von Löhneysen, and C. Meingast. *Phys. Rev. B.* **81** (2010) 060501(R).

[192] R.T. Gordon, N. Ni, C. Martin, M.A. Tanatar, M.D. Vannette, H. Kim, G.D. Samolyuk, J. Schmalian, S. Nandi, A. Kreyssig, A.I. Goldman, J.Q. Yan, S.L. Bud'ko, P.C. Canfield, and R. Prozorov. *Phys. Rev. Lett.* **102** (2009) 127004.

[193] R.T. Gordon, C. Martin, H. Kim, N. Ni, M.A. Tanatar, J. Schmalian, I.I. Mazin, S.L. Bud'ko, P.C. Canfield, and R. Prozorov. *Phys. Rev. B.* **79** (2009) 100506(R).

[194] S. Weyeneth, M. Bendele, R. Puzniak, F. Murányi, A. Bussmann-Holder, N. Zhigadlo, S. Ktrych, Z. Bukowski, J. Karpinski, A. Shengelaya, R. Khasanov, and H. Keller. *Europhys. Lett.* **91** (2010) 47005.

[195] M. Ichioka, K. Machida, N. Nikai, and P .Miranovic. *Phys. Rev. B.* **70** (2004) 144508.

[196] S.R. Saha, N.P. Butch, K. Kirschenbaum, and J. Paglione. *Phys. Rev. B.* **79** (2009) 224519.

[197] A. Leithe-Jasper, W. Schnelle, C. Geibel, and H. Rosner. *Phys. Rev. Lett.* **101** (2008) 207004.

[198] S.L. Bud'ko, N. Ni, and P.C. Canfield. *Phys. Rev. B.* **79** (2009) 220516(R).

[199] Y.J. Uemura, A. Keren, L.P. Le, G.M. Luke, W.D. Wu, Y. Kubo, T. Manako, Y. Shimakawa, M. Subramanian, and J.T. Markert. *Nature.* **364** (1993) 605.

[200] J.W. Loram, K.A. Mirza, J.M. Wada, J.R. Cooper, and W.Y. Liang. *Physica C.* **235-240** (1994) 134.

[201] Y.J. Uemura. *J. Phys.: Condens. Matter.* **16** (2004) S4515.

[202] R. Khasanov, A. Maisuradze, H. Maeter, A. Kwadrin, H. Luetkens, A. Amato, W. Schnelle, H. Rosner, A. Leithe-Jasper, and H.-H. Klauss. *Phys. Rev. Lett.* **103** (2009) 067010.

[203] J.E. Sonier, K.F. Poon, G.M. Luke, P. Kyriakou, R.I. Miller, R. Liang, C.R. Wiebe, P. Fournier, and R.L. Greene. *Phys. Rev. Lett.* **91** (2004) 147002.

[204] T.J. Williams, N.P. Butch, G.M. Luke, M.B. Maple, Z. Yamani, and W.J.L. Buyers. *Phys. Rev. B.* **86** (2012) 235104.

[205] T.J. Williams, H. Barath, Z. Yamani, J.A. Rodriguez-Riviera, J.B. Leao, J.D. Garrett, G.M. Luke, W.J.L. Buyers, and C. Broholm. (2013) In preparation.

[206] N.P. Butch and M.B. Maple. *Phys. Rev. Lett.* **103** (2009) 076404.

[207] E.D. Bauer, V.S. Zapf, P.-C. Ho, N.P. Butch, E.J. Freeman, C. Sirvent, and M.B. Maple. *Phys. Rev. Lett.* **94** (2005) 046401.

[208] F. Bourdarot, E. Hassinger, S. Raymond D. Aoki, V. Taufour, L.-P. Regnault, and J. Flouquet. *J. Phys. Soc. Jpn.* **78** (2010) 064719.

[209] Y. Dalichaouch, M.B. Maple, J.W. Chen, T¿ Kohara, C. Rossel, M.S. Torikachvili, and A.L. Giorgi. *Phys. Rev. B.* **41** (1990) 1829.

[210] J.A. Janik, H.D. Zhou, Y.-J. Jo, L. Balicas, G.J. MacDougall, G.M. Luke, J.D. Garrett, K.J. McClellan, E.D. Bauer, J.L. Sarrao, Y. Qiu, J.R.D. Copley, Z. Yamani, W.J.L. Buyers, and C.R. Wiebe. *J. Phys.: Condens. Matter.* **21** (2009) 192202.

[211] D. Aoki, F. Bourdarot, E. Hassinger, G. Knebel, A. Miyake, S. Raymond, V. Taufour, and J. Flouquet. *J. Phys. Soc. Jpn.* **78** (2009) 053701.

[212] G. Motoyama, T. Nishioka, and N.K. Sato. *Phys. Rev. Lett.* **90** (2003) 166402.